Dynamic Reservoir Characterization of Naturally Fractured Reservoirs from an Inter-Well Tracer Test: A Case Study

Ufuk Kilicaslan[*1], Aymen A. Alramadhan[2], David S. Schechter[3]

Harold Vance Department of Petroleum Engineering, Texas A&M University
College Station, Texas, USA

[*1]ufuk.kilicaslan@pe.tamu.edu; [2]aymen.alramadhan@pe.tamu.edu; [3]david.schechter@pe.tamu.edu

Abstract

After redevelopment of a field located in the Spraberry Trend Area, an inter-well tracer test was conducted in 2011 at the field scale in order to understand the fracture system which forms preferential flow paths, and for better management of waterflooding. The test consisted of 13 injection wells and 110 producing wells that were sampled, with each injector having its own unique water tracer. The test generated 598 tracer responses from 52 out of the 110 sampled wells. A wide range of tracer velocities from 14 ft/day to ultra-high velocities exceeding 10,000 ft/day with same-day breakthrough was observed. Re-injection of produced water has caused the tracers to be re-injected and added an additional challenge to diagnose tracer responses affected by water recycling.

In this study, a comprehensive workflow is presented for dynamic reservoir characterization of naturally fractured reservoirs from an inter-well tracer test by incorporation of analytical interpretation and streamline simulation. Prior to numerical simulation phase, tracer responses were categorized and mapped in accordance to analytical interpretations. The dominating flow trends were detected in E-W and NE-SW directions, where only the NE-SW direction was observed from inter-well tracer test conducted in E.T. O'Daniel lease in 2000. Then, a dual-porosity streamline simulator was used to match both historical production and tracer responses. Historical production performance and tracer responses of an inverted nine-spot pattern were matched and taken as a case study to understand matrix-fracture transfer mechanism, matrix capillary pressure and fluid distribution in the field where no information exists other than dynamic data.

Introduction

Fluid flow in a porous medium is affected by any kind of heterogeneity within rock fabrics. The presence of fractures further triggers the complexity of fluid flow in a porous medium. As a result, characterization of naturally fractured reservoirs becomes more challenging. To overcome difficulty in comprehending fluid flow phenomena in naturally fractured reservoirs, a variety of static and dynamic data are incorporated to understand overall reservoir heterogeneity and to decide the best option for recovery enhancement.

The basic requirement for managing waterflood is to understand how injection wells displace oil to producing wells. However, reservoir-originated effects such as faulting, structure, permeability, influx, and boundaries beside the wellbore make fluid movements complicated to diagnose. Active management of the displacement process can be accomplished by quantifying these complicated fluid movements (Grinestaff, 1999).

Unlike averaged reservoir parameters from pressure transient tests, an inter-well tracer test has many distinctive advantages for reservoir characterization because it could detect reservoir heterogeneity and provide useful information such as volumetric sweep, directional flow trends, and delineation of flow barriers to optimize tertiary recovery in terms of design, control, and implementation (Wagner, 1977).

Although it does not consider transverse dispersion, streamline simulation is presently the best option for

modeling an inter-well water tracer test due to its nature of tracing. It directly assesses dynamic injector-producer connectivity with respect to sweep efficiency, allocation factor, and injection efficiency, so the inter-well tracer test provides reliable, definitive, and unambiguous information on injector-producer connectivity (Guan et al., 2005).

Background of Spraberry Field

The Spraberry Trend Area in West Texas was a candidate for the largest oil field in the world as it covers a 2,500-mi² area in the Permian Basin. Even though estimated oil in the Spraberry reservoir was originally more than 10 billion bbl, the primary recovery factor was less than 10% (Schechter, 2002). The Spraberry sands are fine-grained and interbedded with shales, laminated siltstones, silty sandstones, thin limestones, shaly limestones, and dolomites. The low porosity and low permeability of them is due to close initial packing, pressurizing, and tight cementation (Warn and Sidwell, 1953). However, an extensive vertical fracture system existing in the pay zones makes the field commercial under this low matrix permeability (Elkins, 1953).

Although more than 50 years of waterflooding took place, low oil recovery, which is less than 15% in the Spraberry, was attributed to lack of pattern confinement and injection well density, incorrect well pattern alignment, fracture mineralization (Schechter et al., 1996a), low permeability to oil after waterflooding of the gas-saturated reservoir (Baker, 1996), and stress-sensitive fracture conductivity (Elkins and Skov, 1962; Guo and Schechter, 1997).

Project Description

In late 2010, the operating company took a decision to develop the field and changed existing well pattern to inverted 9-spot by drilling new injectors and producers. In order to understand complex water movement in the reservoir, to assess injector-producer connectivity, and to understand sweep and fractures heterogeneity, a field scale inter-well tracer test was conducted less than one year later. 13 different conservative water tracers were injected through 13 injectors and 110 producers were water sampled for ionic conservative water tracers. They were injected as slug with a ratio of 10%. The tracer test lasted for 114 days from start of tracer injection in April 25, 2011 until last water sample were analyzed in August 17, 2011. A tracer concentration of 50 parts per trillion

(ppt) was determined as a low detection limit. Tracer breakthrough was observed from the same day of tracer injection, and a total of 598 tracer elution curve were detected from 52 out of the 110 sampled wells. As an example, tracer responses of a well throughout sampling period are shown in FIG. 1.
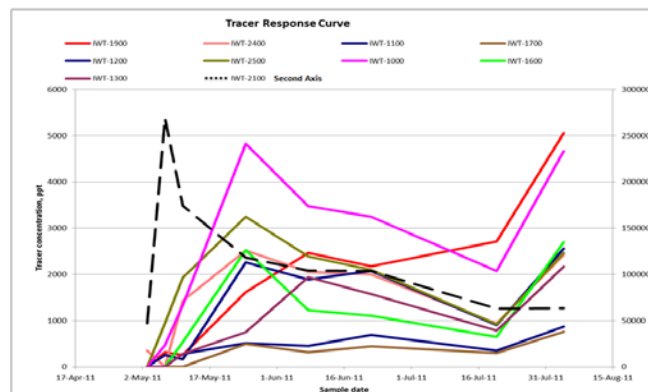

FIG. 1 OBSERVED TRACER RESPONSES FOR A WELL

Produced water which has certain tracer concentration reinjected from injectors without any treatment. Therefore, additional noise on tracer data was introduced due to reinjection of produced water.

Analytical Interpretation Techniques

Before starting simulation work, a quantitative analysis for the tracer data can provide crucial information for building the reservoir model and adjusting reservoir parameters. From observed tracer data, we can easily calculate swept pore volume by Methods of Moments (MOM), tracer recovery, breakthrough time and tracer velocity. Based on magnitude and distribution of those, both static and dynamic reservoir models could be modified.

Method of Moments

MOM is the most common to calculate swept pore volume from tracer responses. In the oil industry, Deans (1978) first applied this method. A general derivation of MOM for 3D for any kind of heterogeneous reservoir was provided by Asakawa (2005).

For each well pair, swept pore volume was calculated and normalized by the global maximum value. The corresponding histogram was formed as seen in FIG. 2.

However, the results are not conclusive for characterization of fracture sets due to its injector-based volumetric formulation. Difference in well location, production rate, tracer recovery,

breakthrough time, etc. between wells did not yield significant difference in swept pore volume. Therefore, MOM results were not taken into account for identification of fracture systems.
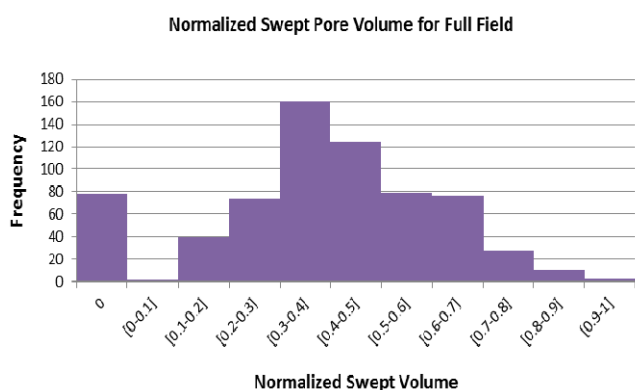

FIG. 2 DISTRIBUTION OF NORMALIZED SWEPT PORE VOLUME FOR FULL FIELD

Tracer Recovery Analysis

Contrary to swept volume calculation, tracer recovery in an offset well offers a clear picture of the relationship between injector and producer. Tracer recovery by percentage for a producer actually equals the percentage of injected water produced by that producer in steady-state conditions. In other words, tracer recovery can show how many barrels of injected water are produced by an offset well and how many barrels of injected water stay in the reservoir. Since both injection and production rates were very stable during the inter-well tracer test with injection/production rates not varying more than 10% from the average rate. A decision was made to assume steady-state condition to calculate tracer recoveries.

Again for each well pair, recovered tracer in percentage was calculated. Because wells far outside pattern area exhibited unusual high tracer recovery compared to the low recoveries within a pattern, a decision was made not to normalize recoveries by injector-producer separation length. As illustrated in FIG. 3, the maximum tracer recovery for any injector is less than 10%. Having a low tracer recovery is unlikely for this field, where a highly conductive and highly intense fracture system is thought to be responsible for high water-cut values observed in the field. This kind of low recovery can be attributed to confinement of tracer in the reservoir. For the confinement of tracer, the injected tracer stays in the reservoir without production by sampled wells. This could be achieved by either the presence of a very low-conductivity fracture system, in which tracers have not reached wells, or by having a good matrix-fracture interaction

mechanism, where a large amount of water imbibes into the matrix system. However, none of the reservoir properties mentioned above was common for the Spraberry Trend Area. Therefore, the injected tracer either moved outside the project area or it was produced by non-sampled wells. Another reason could be the dilution of the injected tracer, which will be highlighted in later sections.
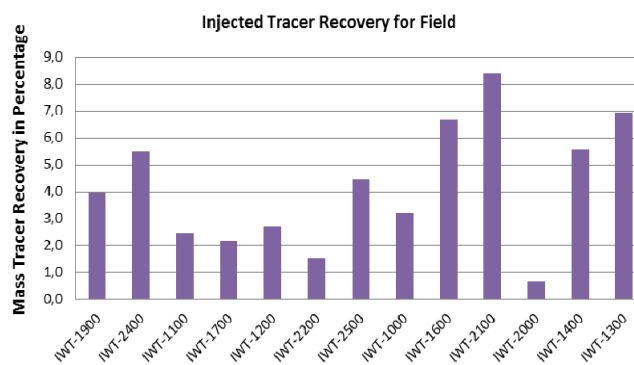

FIG. 3 DISTRIBUTION OF TRACER RECOVERY FOR ALL INJECTORS IN %

The 598 tracer responses obtained in the field were categorized and analyzed by tracer recovery for each response by end of the test. This is in order to overcome the challenge in this study introduced by the absence of any petrophysical and geological characterization work and by the abundance of high resolution dynamic data. The analysis is summarized as a frequency plot in FIG. 4. According to the plot, tracer recoveries higher than 0.1% show a different trend compared to lower values. Since higher tracer recoveries reflect the major direction of water movement, which is driven by the dominant fracture system, a decision was made to focus on tracer responses within this interval. Hence, tracer responses and their relative recoveries were categorized to three different groups as follows: tracer responses with tracer recovery less than 0.1%, tracer responses with tracer recovery between 0.1% and 0.5%, and tracer responses with tracer recovery higher than 0.5%. The first group constitutes higher than 83% of the overall response; however, the amount of received water calculated from this range is extremely low for understanding the source of water for wells. The second category, which is in the range of 0.1–0.5%, is the turning point and covers 12.5% of tracer responses. The remaining group is tracer responses with recovery higher than 0.5%. Even though the last two categories are relatively rare at the field scale, they are the most reliable responses among overall tracer tests in order to characterize the fracture system and to understand the water source of the wells because they constitute a

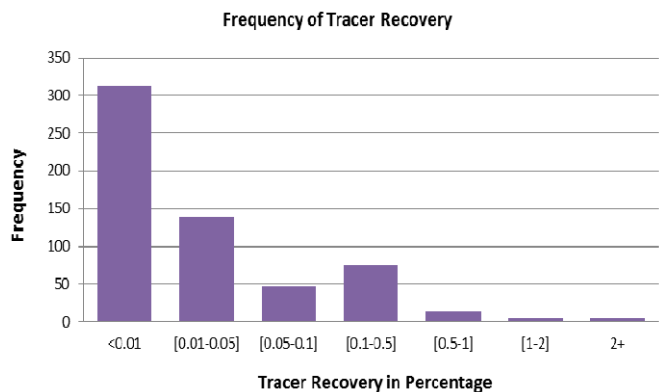large portion of total recovered tracer in terms of amount.

FIG. 4 DISTRIBUTION OF FIELD TRACER RECOVERY IN %

All statistical analysis presented earlier is used as a data mining tool to highlight, group, and map tracer responses that provide relatively more information about reservoir characterization compared to other responses. Tracer responses that are part of the last two recovery categories are mapped separately in FIG. 5 and FIG. 6. Each injector has a unique color, which is the same as the arrow starting from that injector. The map for the second category, shown in FIG. 5, reveals that recovered tracer in the range of 0.1–0.5% flowed through very complex fractures. It is impossible to make a uniform fracture realization over the study area that allows this kind of fluid movement. Characterizing such a complex system requires further knowledge about geology, especially for responses far away from the injector.
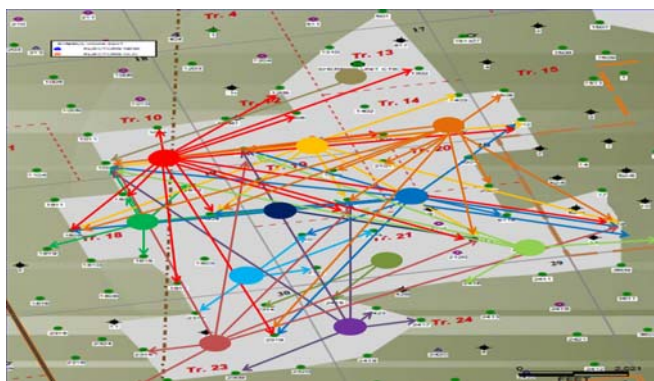

FIG. 5 FIELD TRACER MAP FOR TRACER RECOVERY IN THE RANGE OF 0.1-0.5 %

However, this complexity disappears when tracer recovery higher than 0.5% is mapped at the field scale. As illustrated with solid lines in FIG. 6, no matter their location, all injectors have the same flow trend. This observation proves the existence of a highly conductive fracture system in the E-W direction. Although it is not as common as the E-W direction, some of the injection wells showed another fracture

system in the NE-SW direction. These fracture trends are very close to what is observed from the analysis of horizontal core in the O'Daniel Unit.

For investigation of a NE-SW-oriented fracture system in the reservoir, mapping tracer recovery is done for the last two categories, which are recoveries of 0.1–0.5% (shown by dashed arrows) and recoveries higher than 0.5% (shown by solid arrows). However, this time-mapping of recoveries does not cover all observed wells; it is limited to the inverted nine-spot pattern for each injector (shaded area in field map) in order to analyze them confidently. As demonstrated in FIG. 6, this limited mapping makes clear the existence of another set of fracture systems in the NE-SW direction in addition to that in the E-W direction.
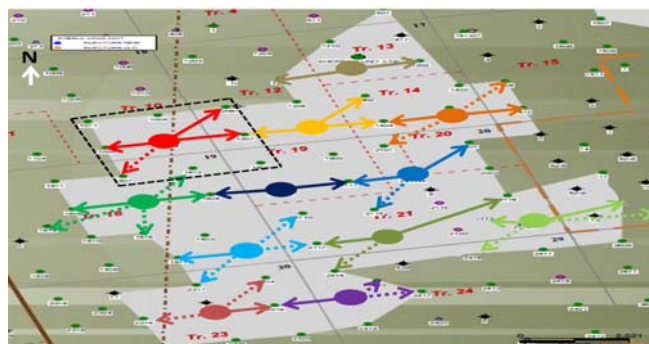

FIG. 6 PATTERN BASED FULL FIELD MAP FOR HIGH TRACER RECOVERY

Traced Water Production

Once tracer recovery in mass is calculated proportionally to the total amount of injected tracer keeping into consideration the stable production and injection rates in the field during the test which resembles study state condition, the obtained fraction can be used to estimate the amount of received water from a particular injector by multiplying the amount of injected water with that fraction. Even though high-recovery wells received a certain amount of water, that amount is very low compared with total water production. Maximum tracer recovery is less than 5% for any well in the field, which means that less than 5% of injected water was produced by corresponding wells. Therefore, remaining water should come from the reservoir or from external water influx.

For deep investigation of traced water, a well pair which has the highest tracer recovery was selected for analysis. In order to assign water contribution of the injector to the producer accurately, only tracer response at the breakthrough time was taken into account because other responses are highly affected by change in flow distribution or streamlines due to

change in well rates. The advantage of this well pair is that breakthrough occurred just 1 day after injection. Another positive aspect of it is that there is no injector located around PROD1 (shown in FIG. 7), which can have an impact on both tracer response and water production.
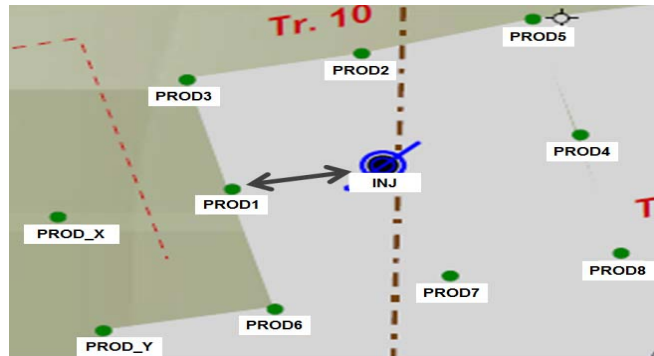

FIG. 7 MAP FOR SAMPLE WELL PAIR

When the fraction of recovered tracer to total injected tracer is multiplied by the water injection rate at the corresponding time, the total amount of injected water produced by this production well only constitutes 0.3 % of water production rate because breakthrough was only 1 day at which highest tracer concentration was observed for this well throughout sampling period, which is also one of the highest tracer concentration observed in the field. Basically, the injection well had no impact on the water production of producer, and this well produces water from either the reservoir or from an external water source according to the tracer result.
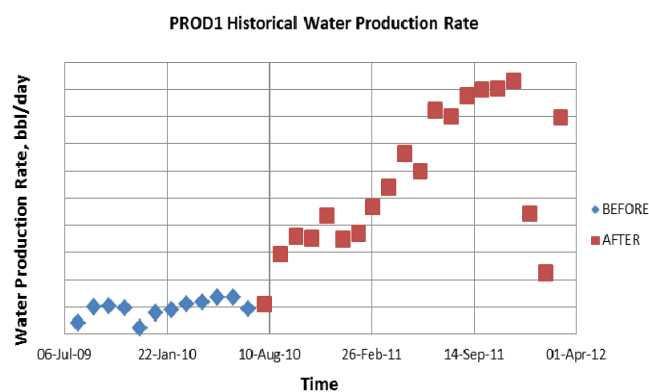

FIG. 8 WELL WATER PRODUCTION RATE IN STB/DAY

In order to validate this observation, the water production rate of the producer was analyzed before and after injection was introduced. As illustrated in FIG. 8, water production rate was tripled after just 1 month. This large amount of change in water production observed after introducing injector cannot be explained by only water influx to producer. More water was received from the injector than was calculated based on tracer. In other words, calculation

of water production based on tracer underestimates water production due to injector. This highlights that the injected tracer was exposed to excessive dilution. As a result, further precaution is required during evaluation of water allocation according to the magnitude of tracer response.

Breakthrough Time Analysis

Breakthrough time of tracers provides valuable information of the conductivity in the fracture systems. Also, analyzing it under categories based on tracer recovery may show some unique behaviors or trends, which helps in further classification. It should be noted that the effect of well-pair distance is included within analysis of tracer velocities next section. The general histogram of breakthrough time of tracer for the full field is demonstrated by FIG. 9. More than 60% of wells got breakthrough within the first 2 weeks, while the injected tracer didn't reach to almost 14% of wells. Also, after the first 2 weeks of the inter-well tracer test, a cyclic behavior is observed and was used in this study as a guide to identify tracers generated by reinjection of produced water.
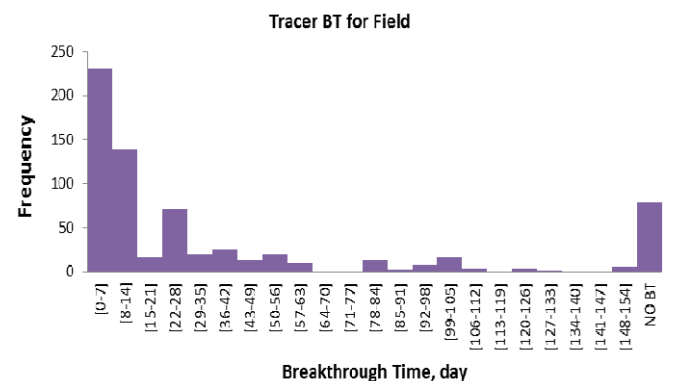

FIG. 9 FULL FIELD TRACER'S BREAKTHROUGH TIME DISTRIBUTION IN DAYS

In order to better understand this cyclic trend, histograms of breakthrough time were generated for each recovery group separately. The low-recovery tracers exhibit almost the same trends seen in FIG. 9 as well as of abnormal non-declining tracer responses. This increases the possibility of the water recycling effect on abnormal-late time responses rather than poorly conductive fractures. On the contrary, such cyclic and abnormal responses are not observed within high tracer recoveries. As can be seen from FIG. 10 breakthrough occurred even within the first week for more than 93% of that specific group. This proves that reinjection of water has minimum impact on high-tracer-recovery wells for their early time response, especially in the first 2 weeks. Thus, for accurately assessing the dominating fracture system in the field,

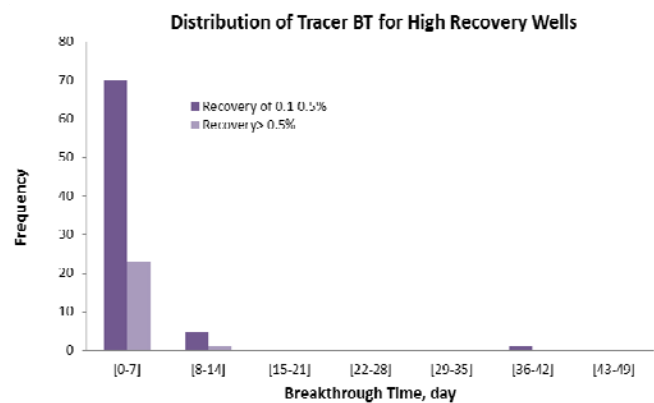only early time response of high-tracer-recovery wells should be used.

FIG. 10 BREAKTHROUGH TIME DISTRIBUTION FOR TRACER RECOVERY >0.1% IN DAYS

Tracer Velocity Analysis

Similar to the breakthrough time study, analyzing tracer velocity can offer significant information about conductivity of fracture systems, especially the distribution of their pore volume. The general distribution of tracer velocities in the field is demonstrated in FIG. 11. Here zero tracer velocity, means that the tracer didn't reach the production well. The highest tracer velocity is 11,334 ft/day, while the slowest one is 14 ft/day after eliminating zero tracer velocities. As seen from FIG. 11, smooth declining trends exist with different slopes, and almost no peak is observed for increasing velocity. However, velocity distribution for high-tracer-recovery responses, which are our main focus for fracture characterization, shows multiple peaks indicating the presence of multiple populations of fracture sets each with a distinctive fracture property. These peaks are shown by FIG. 12 and FIG. 13. Based on these trends, it was recommended to utilize these observations as a starting point for future geological and fracture characterization studies.
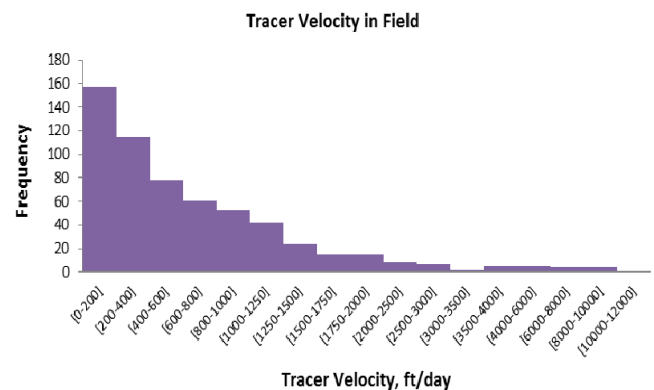

FIG. 11 TRACER VELOCITY DISTRIBUTION FOR FULL FIELD IN FT/DAY
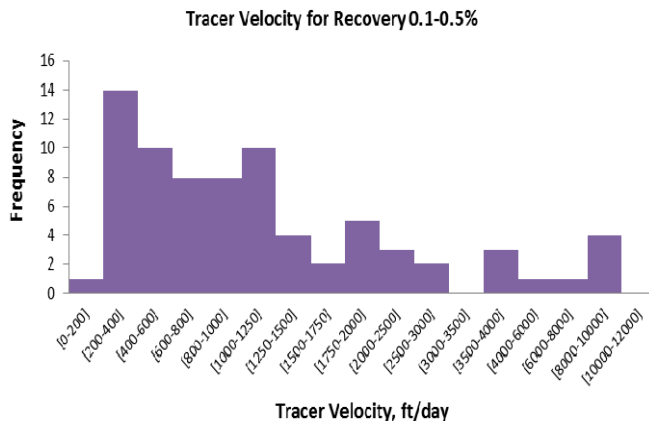

FIG. 12 TRACER VELOCITY DISTRIBUTION FOR TRACER RECOVERY OF 0.1%-0.5% IN FT/DAY
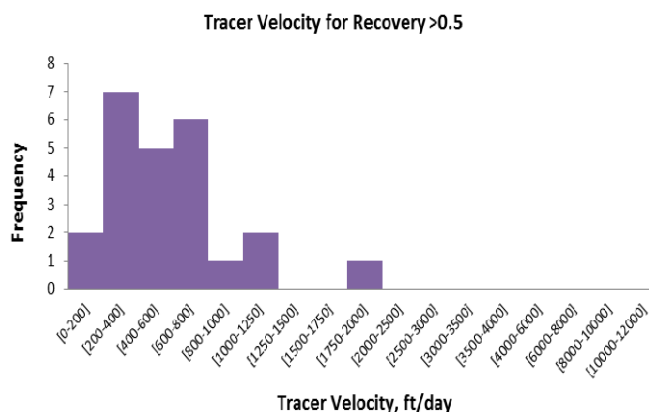
FIG. 13 TRACER VELOCITY DISTRIBUTION FOR TRACER RECOVERY > 0.5% IN FT/DAY

Dual-Porosity Streamline Simulation

Spraberry Trend Area consists of a tight matrix and highly conductive fracture system. The main fluid flow occurs through these fractures, while the matrix is believed to provide fluid storage. A dual-porosity model is the best candidate to reflect this kind of production performance. A commercial dual-porosity streamline simulator, FrontSim™ was used to simulate reservoir performance. An important drawback of the used simulator is the lack of tracer transport analysis for dual-porosity models. However, time-of-flight (TOF) and allocation factor which are the main functionalities of streamline simulation over finite-difference solution can be attributed to tracer breakthrough time and tracer recovery respectively.

Base Model Construction and Sensitivity Analysis

A base three-phase, 3D, dual-porosity model was created for a selected pattern in order to conduct sensitivity analysis and manual history matching. A structural model of the study area, rock and fluid properties, matrix and fracture properties, and rock-fluid and matrix-fracture interaction properties are

required in order to construct a dual-porosity model.

Initially, the general structure of the base model was constructed according to FIG. 14, in which 1U and 5U which are sand oil-productive zones are separated by a shale formation with a thickness of 140 ft. The matrix is known as a tight matrix; however, there is no definitive information about fracture properties except average fracture spacing. Pressure, volume, and temperature (PVT) for the field was taken from differential liberation and a flash test of one of the wells located in the Spraberry Trend Area. For matrix capillary pressure, measurements done by the static equilibrium method were taken from the paper written by Guo et al. (1998) and details are presented in FIG. 15 below. Based on end points of residuals from capillary pressure data, which are 0.22 for water and 0.57 for oil, relative permeability for the matrix was constructed by using correlations as shown in FIG. 16, while relative permeability of both oil and water is a straight line for fractures with zero capillary pressure, which is the most common way of modeling fractures.
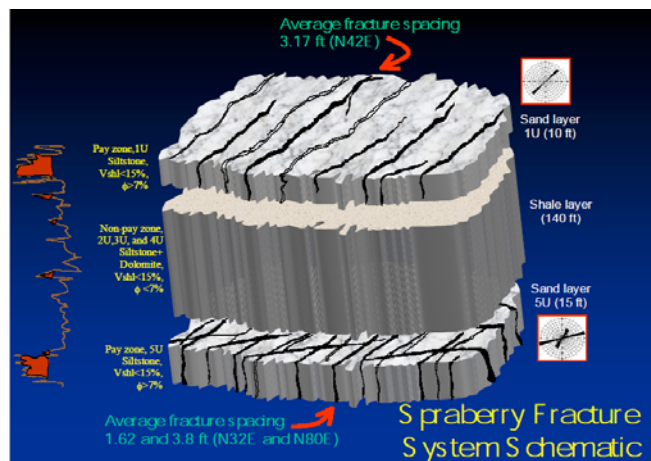

FIG. 14 SCHEMATIC DIAGRAM OF FRACTURE SYSTEM IN UPPER SPRABERRY
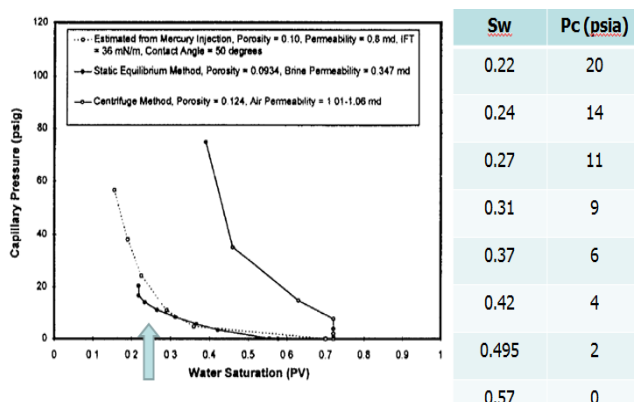

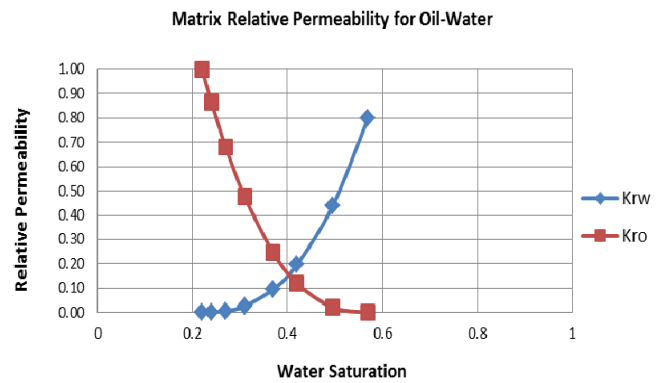FIG. 15 MEASURED MATRIX CAPILLARY PRESSURE FOR SPRABERRY, GUO ET AL. (1998)

FIG. 16 OIL-WATER RELATIVE PERMEABILITY CURVES

Because available simulator does not calculate tracer concentration in a dual-porosity model, the main objective was to associate breakthrough time and tracer recovery with water production response for changes in reservoir properties. As a result, simulations were compared with respect to field water cut after each sensitivity case. A three-phase, dual-porosity model was built with available data stated previously. For simulation, selected inverted nine-spot (shown in FIG. 6 with black dashed lines) was representative enough because four of the wells located there were newly drilled and four of them showed very high tracer response in both E-W and NE-SW directions. This pattern was simulated from the start of injection under the oil constraint operation limit. Sensitivities were conducted on 38×38×6 grid system with a grid dimension of 100 ft. Due to grid block size, time step is limited to 0.1 days for accuracy.

Sensitivity analysis was done for sigma (matrix-fracture interaction coefficient), water saturation, pressure, matrix porosity, fracture porosity, fracture permeability, matrix capillary pressure, matrix relative permeability, and matrix residual oil saturation. After being sure of the producing historical oil rate, field water-cut responses were compared with each other to figure out which parameter was more effective on water production. From sensitivity analysis, important reservoir parameters that mainly control water production were determined as sigma, water saturation, fracture porosity, and fracture permeability.

History Matching

First step of manual history matching is determining historical production data to be matched based on project objective. Then, reservoir properties to be modified during this process are assigned and ordered starting from the least accurately known property with significant effect on reservoir performance to a

property with certain level of confidence, having least effect on production. However, due to complete absence of geological and petrophysical studies in the area understudy, models were built entirely based on dynamic data. A general knowledge of fracture and formation properties from nearby leases was used as general guide. Due to abundance and high resolution nature of tracer tests, they can contribute to build more representative reservoir models in such a way that any kind of flow heterogeneity detected from inter-well tracer test can be represented by adjusting related model parameters.

Once important reservoir parameters were identified, manual history matching began to replicate both observed field and individual well production performance. For accuracy and visualization, the grid system was changed to 76×76×6, including fractures with the same areal resolution. Also, the thickness of 5U was reduced to 10 ft based on perforations from the injection profile log. Another important change was controlling criteria switched from oil rate constraint to total liquid rate constraint. This constraint is more suitable for streamline simulation because streamlines are calculated from total fluid velocity rather than individual oil or water velocity.

In manual history matching, early efforts are put into matching cumulative liquid production. Because it is a volumetric issue, actual production for the individual liquid was matched by adjusting its saturation. However, the initial focus was assigning a sigma coefficient for our case. According to the fracture system in FIG. 14, sigma was calculated as 1.84 1/ft² from Kazemi's shape factor formula, assuming that two fracture systems exist for both layers. In this case, water saturation was assumed to be the main reason for high-water-cut observations, so fracture water saturation was determined as 0.95. Even for this kind of high water saturation, sigma based on fracture spacing produces much more oil than observed data, shown by Fig. 17. To ensure sigma effect on oil production, water saturation was increased to 0.995, and then each case was simulated for that. Fig. 18 demonstrates that even a sigma of 0.01 has more oil production than observed for such extreme water saturation. This highlights that the actual matrix-fracture interaction in the field is much lower than calculated. There should be some other mechanisms that inhibit counter-current flow between the matrix and fracture in spite of the closely spaced fracture system. The primary reason seems to be fracture mineralization. As illustrated by FIG. 19, excessive

mineralization on the fracture surface causes very poor matrix-fracture interaction. Therefore, most injected water didn't sweep oil from the matrix because it couldn't imbibe into the matrix.

FIG. 17 CUMULATIVE OIL PRODUCTION OF FIELD AT Sw = 0.95 FOR INCREASING SIGMA
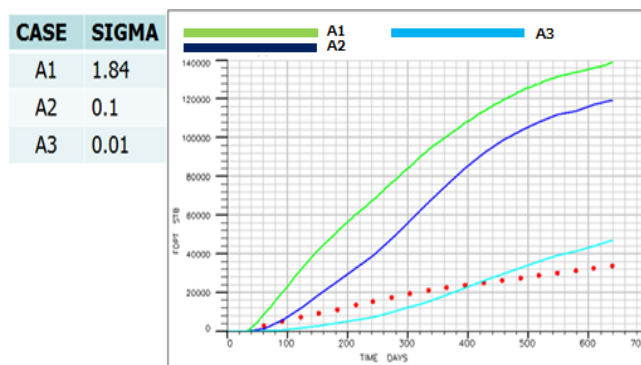
FIG. 18 CUMULATIVE OIL PRODUCTION OF FIELD AT Sw = 0.995 FOR INCREASING SIGMA

FIG. 19 OBSERVED MINERALIZATION ON FRACTURE SURFACE FROM SPRABERRY CORE

To assess remaining reservoir parameters during history matching, optimum sigma was ensured after conducting a composite sensitivity analysis of sigma – matrix capillary pressure. As listed in table 1, four different capillary pressure sets including extreme zero case were used to determine most likely sigma in the field. For any of the capillary pressure sets except last one which is fracture type capillary pressure, sigma of 0.01 can produce much more oil than historical production as seen in FIG. 20. However, extremely small sigma conceals the effect of difference in capillary pressure and none of them could produce

as much as observed cumulative oil production at the end of simulated period except PC1 set as demonstrated by FIG. 22. On the other hand, sigma of 0.001 seems to be representative enough for field-scale matrix-fracture interaction since difference in capillary pressure sets can be still seen and production performance of it with low capillary pressure is somehow close to historical one as illustrated in FIG. 21. Another interesting point in this sensitivity analysis is that PC1 set which was measured experimentally in a core-scale was able to produce more oil than observed cumulative oil production even for extremely small sigma case. This observation questions accuracy of our capillary pressure (PC1) because of overestimation in matrix contribution to oil production. Therefore, it can be interpreted that actual capillary pressure in the field seems to be much more less than measured.

TABLE 1 MATRIX CAPILLARY PRESSURE SETS

Sw	PC1	PC2	PC3	PC4
0.22	20	5	2.5	0
0.24	14	3.5	1.75	0
0.27	11	2.75	1.375	0
0.31	9	2.25	1.125	0
0.37	6	1.5	0.75	0
0.42	4	1	0.5	0
0.495	2	0.5	0.25	0
0.57	0	0	0	0

FIG. 20 CUMULATIVE OIL PRODUCTION OF FIELD AT SW = 0.995 FOR SIGMA OF 0.01

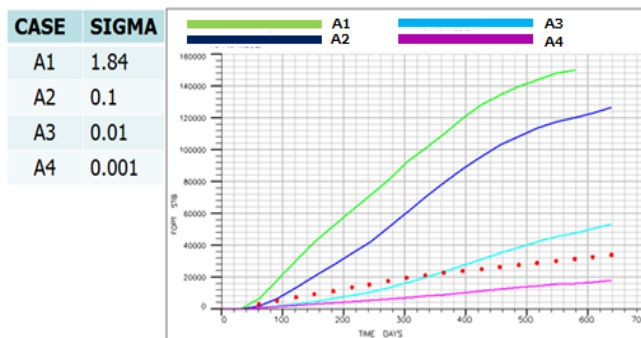FIG. 21 CUMULATIVE OIL PRODUCTION OF FIELD AT SW = 0.995 FOR SIGMA OF 0.001

FIG. 22 CUMULATIVE OIL PRODUCTION OF FIELD AT SW = 0.995 FOR SIGMA OF 0.0001

CASE	Sw_m	Sw_f
A1	0.515	0.74
A2	0.48	0.78
A3	0.45	0.84
A4	0.40	0.90

FIG. 23 EFFECT OF INITIAL WATER SATURATION ON CUMULATIVE OIL PRODUCTION

Once sigma was kept constant at 0.001, only initial water saturation and fracture porosity remained as key parameters in order to get a match for the cumulative field because initial water saturation determines amount of oil in place and the latter controls not only amount of oil in place, but also amount of water production due to injected water. Estimating the amount of water in the matrix and in the fracture is critical for initial water saturation distribution. To understand the impact of water distribution in the matrix and fracture, sensitivity analysis was done for increasing water saturation in the fracture while at the same time decreasing it in the matrix. It can be seen from FIG. 23 that higher oil production during the early time is due to lower water saturation in the fracture, while lower matrix water saturation causes large oil production during the late time, as expected. However, actual field performance is closer to the simulated case, in which the saturation difference between the matrix and fracture is low for this particular simulation model. This observation is vital to evaluate actual field performance based on this model. The discrepancy between the matrix and fracture in terms of initial water saturation should be low according to this model, which means that water saturation in the matrix is higher than expected. This could be achieved under two circumstances—either

initial fluid distribution in the reservoir or an external water source flowing to the field. The first one is related to migration of oil or water during the primary reservoir process. In other words, the matrix was already saturated by a large amount of water before any field production started. The other reason could be that the matrix was watered by water influx coming from an external source. Both initial water saturation measurements during primary production and the external water source hypothesis in the Spraberry support having high initial water saturation in the matrix.

Since PC1 set was used in previous sensitivity analysis as a matrix capillary pressure, which is evaluated as overestimated capillary pressure, conclusion regarding high initial matrix water saturation should be validated for different capillary pressure sets. Therefore, another composite sensitivity analysis of initial water saturation in the matrix– matrix capillary pressure was conducted. As demonstrated in FIG. 24, FIG. 25 and FIG. 26 respectively, increase in matrix water saturation leads to reduce effect of difference in capillary pressure as expected. For deep investigation, fracture water saturation which could be assumed main reason for water cut in the field was assigned as 0.76, which is actual water-cut, to homogenous reservoir model and same sensitivity was conducted for PC1 and PC3 set. As it can be seen in FIG. 27 and FIG. 28, even though PC1 set results in more oil production than PC3 as expected, historical oil production stays in such an interval in which matrix water saturation varies from 0.5 to 0.57 for both case. This sensitivity analysis not only confirmed high initial matrix water saturation in the field but also questioned our capillary pressure interpretation stated above. It is more accurate to say that initial matrix water saturation in the field is such a high value where capillary pressure is very low, rather than saying that PC1 set is not correct and overestimated.
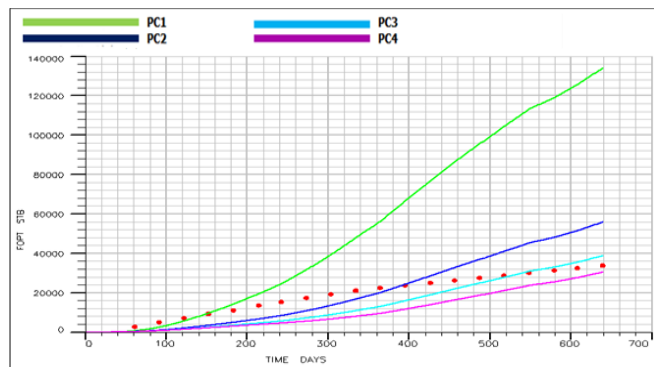
FIG. 24 CUMULATIVE OIL PRODUCTION OF FIELD AT SW_M = 0.3 FOR SIGMA OF 0.001
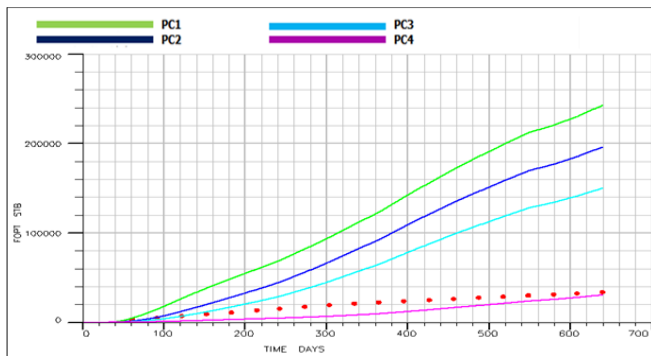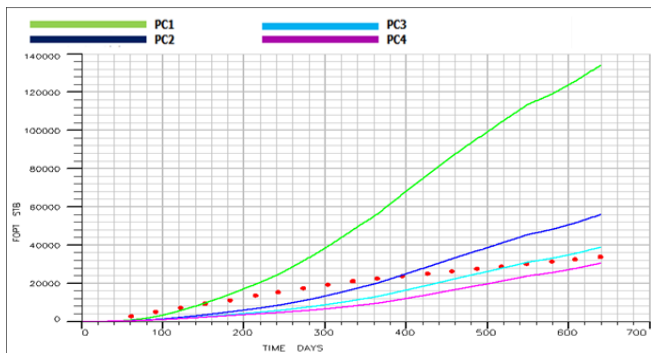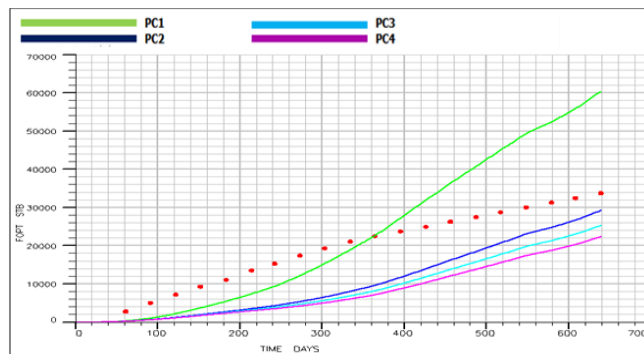

FIG. 25 CUMULATIVE OIL PRODUCTION OF FIELD AT SW_M = 0.4 FOR SIGMA OF 0.001

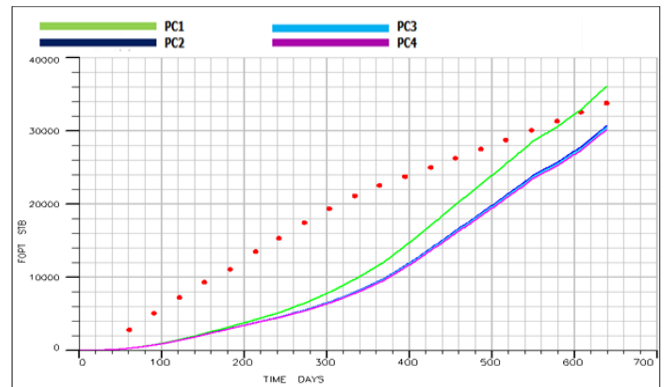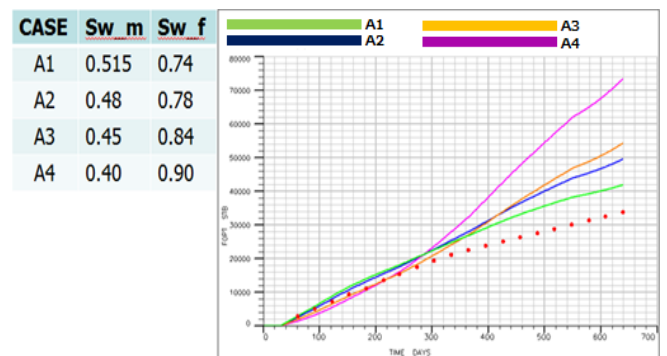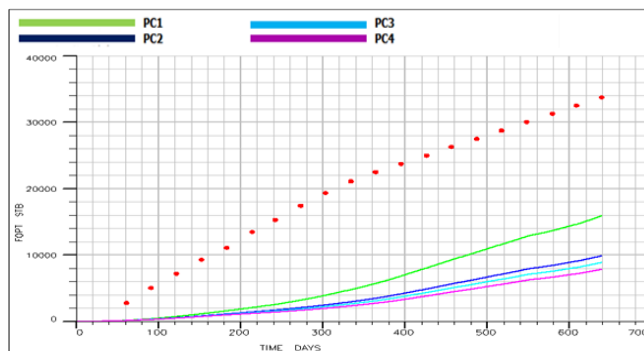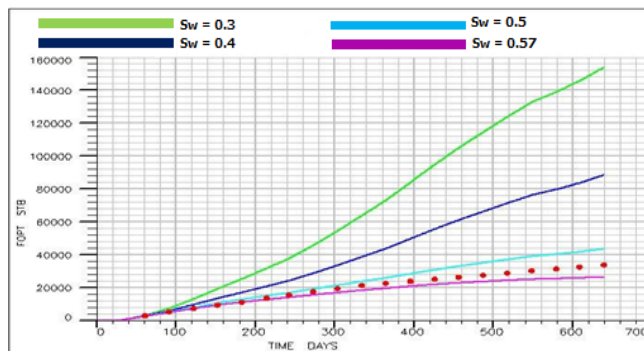FIG. 26 CUMULATIVE OIL PRODUCTION OF FIELD AT SW_M = 0.5 FOR SIGMA OF 0.001

FIG. 27 CUMULATIVE OIL PRODUCTION OF FIELD AT SW_F = 0.76 FOR PC1 SET
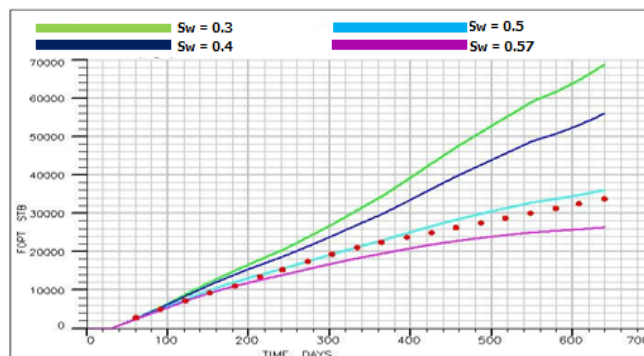

FIG. 28 CUMULATIVE OIL PRODUCTION OF FIELD AT SW_F = 0.76 FOR PC3 SET

After several runs with that model, an initial matrix water saturation of 0.53 and initial fracture saturation of 0.76 provided the final match obtained for cumulative oil production and cumulative water

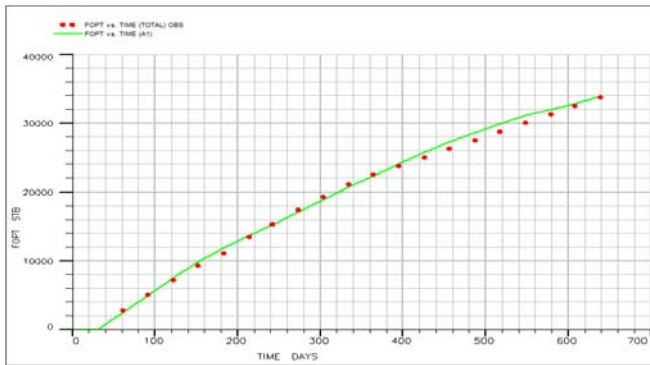production, as shown in FIG. 29 and FIG. 30, respectively.

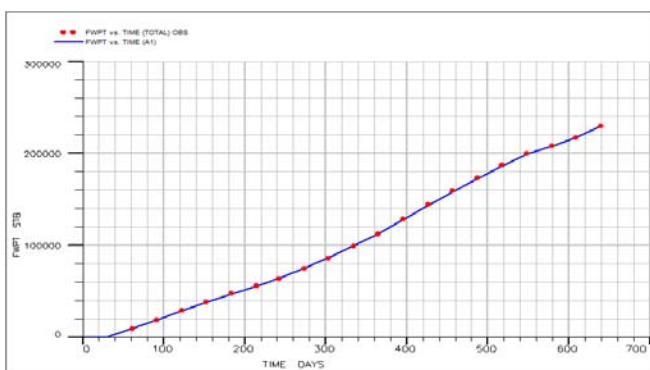FIG. 29 OBSERVED AND SIMULATED CUMULATIVE OIL PRODUCTION OF FIELD

FIG. 30 OBSERVED AND SIMULATED CUMULATIVE WATER PRODUCTION OF FIELD

Well-by-Well History Matching

Although cumulative field production closely agrees with observed data, individual well performance is far from actual for many of them. The main reason for this is incorrect distribution of injected water. In other words, actual water allocation from the injector for each well is different from the simulation case. Geometric allocation factors are too poor to identify the dynamic relationship between injector and producer. To quantify actual allocated water for each well, there should be some dynamic data that provide information about the relationship of the injector-producer well pair. The novelty of the inter-well tracer test emerges at this point, where it directly assesses this relationship. Before moving to well-by-well history matching, tracer results should be evaluated for a better description of fluid flow and should be used for adjusting reservoir parameters. Both cumulative liquid production (represented by dark blue) and tracer response (represented by red) were delineated, as shown in FIG. 31. The total weight of each well in the pattern is demonstrated as a percentage for both cumulative liquid and tracer production. Also, a small portion in the dark blue

circle corresponds to cumulative oil production, while the rest of it shows cumulative water production.
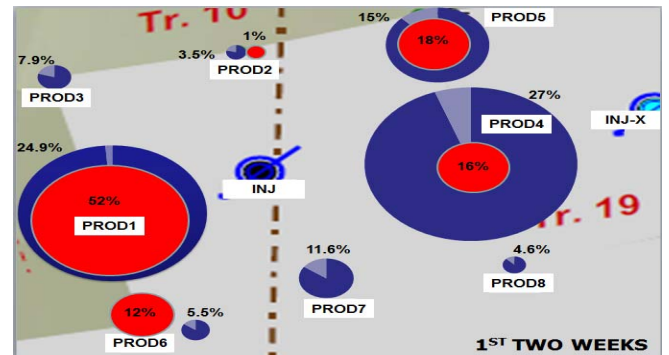
FIG. 31 CUMULATIVE LIQUID AND TRACER PRODUCTION FOR PATTERN

This composite analysis gives insightful information about reservoir characterization. First of all, both production and tracer data indicate flow domination in the E-W direction. They also show other domination in fluid flow in the NE-SW direction in spite of the smaller quantity compared with E-W. These flow trends remark on the existence of highly conductive fracture systems in these directions, as mentioned before. However, a very poor fracture system was observed in N-S direction, while almost no fracture system exists in the NW-SE direction according to tracer recovery. For further analysis, wells were categorized based on tracer presence. PROD1, PROD4, PROD5, and PROD6 showed high tracer response, and PROD2, PROD3, PROD7, and PROD8 showed either very low or no tracer response.

PROD1 definitely has the highest water allocation from the injector based on these data. Even though PROD4 produces the largest amount of liquid in the pattern, at least half the production comes from the nearby injector of INJ-X. This was confirmed by comparison of tracer recovery and breakthrough time for INJ and INJ-X injectors. PROD4 has a tracer recovery of 0.912% with 5 days breakthrough from INJ, while it has 1.705% tracer recovery with a breakthrough time of 2 days for INJ-X. Based on that, the proportion of PROD4 in the pattern could be lowered by half. This reduction makes water movement clear because PROD5 receives more water from the injector compared with PROD4 according to the new ratio. Tracer observation has exactly the same conclusion, in which higher recovery was observed for PROD5. The behavior of PROD6 is more complex than the others because it showed high tracer recovery; however, total liquid production is less than 6%. This kind of poor production can be clarified by the fact that the amount of water received from the injector

was actually smaller than expected based on tracer results. Hence, the allocation factor for PROD6 should be low. Furthermore, it can be concluded that injected water tends to flow in the W and N-E directions from both cumulative production and tracer recovery wells. The underlying reason could be dipping of the reservoir and pressure difference rather than due to only an oriented fracture system.

For PROD2, both cumulative production and tracer recovery is very low. Unlike the old well, PROD2, PROD3 has moderately high liquid production as a new well without any contribution from the injector. Having no tracer response could be the outcome of a sealing fault between PROD3 and INJ, as well as the lack of a NW-SE fracture system. Similarly, PROD7, which is also a new well, produces a significant amount of liquid, while received water due to the injector is negligible. PROD8 again shows a low production capacity with insignificant tracer response. It is clear that old wells, PROD2 and PROD8, produce much less than new wells, PROD3 and PROD7, as expected because the drainage area of the new wells hasn't swept yet and was already depleted for the old ones.

According to the conclusions from a composite interpretation of production and tracer data, some of the grid blocks were modified in order to create flow anisotropy. Any kind of cell-based modification was applied to both 1U and 5U. Initial trials for history matching were changing fracture porosity and fracture permeability of modified grid cells. However, it was not good enough to obtain a reasonable match because certain differences were present either during the early time or late time. To compensate for these differences, initial saturation of nearby cells was adapted mostly based on being an old or new well, as well as fracture porosity.

After conducting several runs to get a match for wells, cumulative field production was not as good as previously seen, especially for oil production. However, initial water saturation in the fracture and matrix were reduced to 0.74 and 0.515, respectively. The final match was very close to actual data for both the field and individual wells. Especially for water production, each well has an almost perfect match. Besides liquid production match for wells, tracer breakthrough time was matched, as illustrated by FIG. 32. Except for PROD6, they are exactly same for observed breakthrough time.
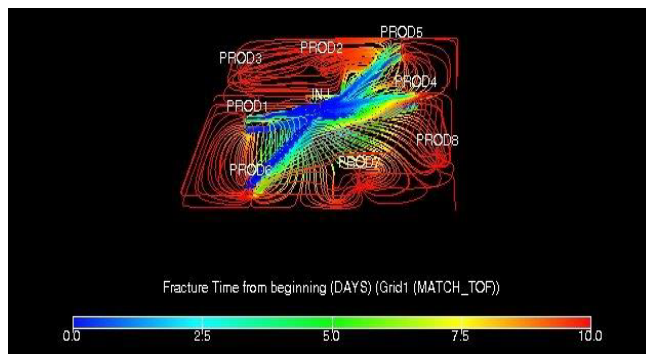
FIG. 32 TIME OF FLIGHT (TOF) AT TRACER INJECTION

Conclusions

In this study, dynamic reservoir characterization of the field located in Spraberry Trend Area, a naturally fractured reservoir, was done based on field production performance and tracer responses. To accomplish accurate reservoir characterization, a variety of different approaches were incorporated into this analysis. Before starting simulation work, tracer responses were categorized in terms of tracer recovery, breakthrough time, velocity, and traced water production by analytical interpretation techniques and were then mapped in order to identify preferential flow trends. Flow anisotropy was created by modifying some of the grid properties based on conclusions from a composite interpretation of production and tracer data. Historical production performance of inverted nine-spot and breakthrough time of injected tracer were matched successfully by simulation of 3D, three-phase, dual-porosity model. Main conclusions from this research can be summarized as follows:

- Field-wide tracer recovery is less than 10% for any injected tracer, which is too low for highly conductive fractures commonly seen in the Spraberry Trend Area. Injected tracer was not confined in the field and most likely flowed outside the well, as it might be produced by non-sampled wells because of poor matrix-fracture interaction. Another reason could be excessive dilution of tracer, which was shown for the PROD1-INJ well pair.

- Mapping categorized tracer recovery based on its distribution is helpful to assess direction of the dominating fracture system. Even though the map of tracer recovery in the range of 0.1–0.5% shows a very complex fracture system, it disappeared by mapping tracer recovery higher than 0.5%, and then the presence of an E-W fracture trend became obvious.

Furthermore, the map of those two categories in a pattern base was helpful to confidently detect a NE-SW fracture system.

- Calculated water production due to injector based on tracer response is much lower than actual because injected tracer was excessively diluted, which was proved for the PROD1-INJ well pair. For accurate estimation of water contribution from injector, water production of the well should be monitored before and after the injection period, if it is present. In spite of the recognition of underestimated water production based on tracer response, water influx to the field can be still one of the reasons for abnormally high water cuts observed in the field for many wells.

- Breakthrough time analysis showed that water recycling has an influence on low-recovery wells' response after the first 2 weeks, while its effect does not exist for high-tracer-recovery wells, at least during the first 2 weeks. To be confident, it is suggested to only use tracer responses during the first 2 weeks for interpretation of fracture sets.

- Distribution of overall tracer velocities, particularly high-recovery tracer velocities, has the potential to further refine reservoir dynamics as well as fracture and geological characterization in future studies.

- An extremely high-water-saturation example proves that the actual matrix-fracture interaction in the field is much lower than calculated sigma based on fracture spacing. Fracture mineralization seems to be the main reason for limited counter-current flow between the matrix and fracture, in spite of a closely spaced fracture system.

- According to the base model properties, water saturation in the matrix is higher than expected. This could be due to either initial fluid distribution settled during pre- or post-deposition of the reservoir, in which the matrix had been watered before any field production started or to an external water source flowing to the field after field production. To a certain extent, both of them are believed to be valid.

- More accurate way to explain capillary pressure is that actual capillary pressure in the field corresponding to high matrix water saturation is very low, instead of saying that measured capillary pressure is overestimated. Therefore, further reduction occurs in imbibition mechanism in addition to low sigma.

- Flow domination in field production and high tracer responses strongly agree on the presence of highly conductive fracture systems in the E-W and NE-SW directions. However, a very poor fracture system was observed in the N-S direction, while almost no fracture system exists in the NW-SE direction according to tracer recovery.

- The tendency of flow observed with both higher liquid production and more tracer recovery toward the W and N-E directions could be a result of reservoir dipping and pressure difference rather than oriented fracture system.

- High tracer response does not necessarily mean more allocated water, as in the case of PROD6.

- In off-trend wells, production capacity of newly drilled wells is larger than old wells because of an unswept drainage area.

- By incorporation of tracer results into history matching, fracture porosity was refined in the E-W and NE-SW directions to model preferential flow paths after determining sigma, matrix and fracture water saturation in field scale from historical production.

- Regeneration of historical production performance was achieved by the constructed model based on dynamic data for oil and water at both the field and well scale.

REFERENCES

Asakawa, K. (2009). "A Generalized Analysis of Partitioning Interwell Tracer Tests." Ph.D. Thesis, The University of Texas at Austin.

Baker, R.O. (1996.) "Reasons for the Relatively Low Recovery of the Spraberry Waterfloods." PRRC Spraberry Database, New Mexico.

Deans, H.A. (1978). "Using Chemical Tracers to Measure Fractional Flow and Saturation In-Situ." SPE 7076-MS.

Elkins, L.F. (1953). "Reservoir Performance and Well Spacing, Spraberry Trend Area Field of West Texas." Journal of Petroleum Technology, 5(7): 177-196

Elkins, L.F. and Skov, A.M., 1962. "Large Scale Waterflood

Performance Sprayberry Field, West Texas." SPE 405-MS.

Grinestaff, G.H. (1999). "Waterflood Pattern Allocations: Quantifying the Injector to Producer Relationship with Streamline Simulation." SPE 54616-MS.

Guan, L., Du, Y., Johnson, S.G. and Choudhary, M.K. (2005). "Advances of Interwell Tracer Analysis in the Petroleum Industry." Journal of Canadian Petroleum Technology, 44(5).

Guo, B. and Schechter, D.S. (1997). "Use of a Simple Mathematical Model for Estimating Formation Damage in Wells Intersecting Long Fractures." SPE 38178-MS.

Schechter, D. (2002). "Waterflooding and CO2 Injection in the Naturally Fractured Spraberry Trend Area." Journal of Canadian Petroleum Technology, 41(10): 9-14.

Schechter, D.S., McDonald, P., Sheffield, T. and Baker, R. (1996a). "Reservoir Characterization and CO2 Pilot Design in the Naturally Fractured Spraberry Trend Area." SPE 35469-MS.

Wagner, O.R. (1977). "The Use of Tracers in Diagnosing Interwell Reservoir Heterogeneities - Field Results." Journal of Petroleum Technology, 29(11): 1410-1416.

Warn, G.F. and Sidwell, R. (1953). "Petrology of the Spraberry sands of West Texas." Journal of Sedimentary Research, 23(2): 67-74

Ufuk Kilicaslan is a Reservoir Engineer working for Turkish Petroleum Corporation (TPAO), national oil company of the Republic of Turkey in Ankara. He actively involves in developing reservoir models for overseas exploration blocks and on-going international projects of the company.

He received his bachelor's degree of science in Petroleum and Natural Gas Engineering from Middle East Technical University, Ankara, Turkey in 2010. After getting scholarship from TPAO, he received his M.Sc. degree of Petroleum Engineering from Texas A&M University, College Station, U.S., in 2013.

Aymen A. Alramadhan is Reservoir Engineer working for Saudi Aramco since 2008. He is an active member of multi-disciplinary team managing offshore fields at Saudi Aramco. As Petroleum Engineer, Aymen worked as petro physicist, reservoir simulation, and well testing engineer on various giant oil fields owned by the company.

In 2008, he received his B.Sc. degree in Petroleum Engineering from King Fahd University of Petroleum & Minerals, Dhahran, Saudi Arabia and in 2013; Aymen received his M.Sc. degree in Petroleum Engineering from Texas A&M University, College Station, U.S.

David S. Schechter is Associate Professor of Petroleum Engineering at Texas A&M University, College Station, Texas. His research interests are Spraberry Trend Area, geological and petrophysical analysis, wettability determination and imbibition experiments, numerical modelling and reservoir simulation, and CO2 flooding and gas injection.

He received his B.Sc. degree in Chemical Engineering from The University of Texas at Austin, Austin, U.S. in 1988 and his Ph.D. degree in Physical Chemistry from Bristol University, England in 1988. He headed the Naturally Fractured Reservoir Characterization/Engineering group at the New Mexico Institute of Mining and Technology for 7 years. He has been involved in an extensive reservoir characterization effort in the naturally fractured Spraberry Trend Area which has involved geological, petrophysical, logging interpretation, core-flooding and simulation studies. He also spent five years at the Petroleum Engineering Department at Stanford University as a Post-Doctoral Research Associate and Assistant Professor.

Combustion Properties of Spray Flames of Canola Methyl Ester and Diesel Blends at Lean Inlet Equivalence Ratios

C. Aldana[*1], R. N. Parthasarathy[2], S. R. Gollahalli[3]

School of Aerospace and Mechanical Engineering, University of Oklahoma

865 Asp Avenue, Norman, OK 73019, USA

[*1]cristian254@ou.edu; [2]rparthasarathy@ou.edu; [3]gollahal@ou.edu

Abstract

The objective of this study was to document the combustion characteristics of spray flames of Canola Methyl Ester (CME) and No 2 diesel (petroleum fuel) blends. Three blends with 25%, 50% and 75% volume concentration of CME were studied. The fuel was atomized and burned in a heated stream of air at supply equivalence ratios of 0.62 and 0.75. Measurements of global CO and NO emissions, in-flame temperature and in-flame concentrations of combustion products were made. The near-injector homogeneous gas-phase reaction zone increased in size with the addition of CME. The global NO emission decreased significantly with the increase in CME content in the fuel blend at the equivalence ratio of 0.62; however, the global NO emission index of all the tested flames was comparable at the equivalence ratio of 0.75. The in-flame NO concentration profiles and flame temperature profiles followed similar trends, suggesting that the thermal mechanism of NO formation was dominant in these flames.

Introduction

Biofuels, such as canola methyl ester (CME), are made from renewable sources and are nearly carbon-neutral, making them attractive alternatives to petroleum fuels. The properties of these biofuels are similar to those of petroleum fuels enabling them to be easily blended with petroleum fuels. Furthermore, the blends can be used in current automobile engines with minor modifications. In the near future, such biofuel/diesel blends provide a viable option as fuels for transportation and help reduce our dependence on petroleum fuels.

There have been a few studies on the use of biofuels and their blends in diesel engines. Schumacher et al. (2001) compared the performance of two engines that were fueled with various blends of biofuel and petroleum diesel fuel. An increase in NOx emissions, accompanied by a decrease in CO, particulate matter (PM), and unburned hydrocarbons was observed with the addition of biofuels. Canakci and Gerpen (2003) found that the use of soybean biofuel resulted in significant reductions in PM, CO, and unburned hydrocarbon emissions. Tsai et al. (2010) documented a reduction in the emissions of PM, total carbon and polycyclic aromatic hydrocarbons (PAHs) from a diesel generator fuelled with soy-biodiesel blends. Fontaras et al. (2010) tested five biodiesels from different feedstocks (rapeseed, soy, sunflower, palm, and used fried oils) blended with diesel (10% by volume) in a passenger car and found that NOx emissions increased by up to 20% for two blends, and decreased by up to 15% for two blends. Song et al. (2012) documented the NO and soot emissions under different load conditions from a diesel engine that was fuelled with biodiesel and found that the NO emissions were higher with the biodiesels on an average. Bari (2014) found that the CO and soot emissions were lower and NO emissions were increased slightly when a biodiesel blend (20% biodiesel by volume) was used in a metro-bus. Thus, the effects of biofuel blends on engine emissions are still not definitive.

In general, pollutant emission studies in engines have shown that the majority of biofuels produced more NOx, less CO, PM, and unburned hydrocarbons than

diesel fuel, although the effects of blending are still debatable. Several reasons, including differences in physical properties (such as compressibility), changes in spray atomization and ignition delay (due to differences in viscosity and surface tension), and differences in chemical structure (presence of oxygen in biofuels and differences in iodine number) have been offered as reasons for these observed changes.

Love et al. (2009) made in-flame NO concentration and temperature measurements in laminar partially-premixed flames of vaporized biofuels in air at various burner-exit equivalence ratios. It was found that the peak NO concentrations occurred in the fuel-rich near-burner region and that the peak NO concentrations increased with the iodine number of the fuel. At equivalence ratios greater than 3, the peak NO concentrations were not correlated with the peak temperatures and the Fenimore (prompt) mechanism rather than the Zeldovich (thermal) mechanism was suggested to be dominant. Singh et al. (2013) studied the combustion properties of CME/diesel blends in a set-up similar to that of Love et al. (2009) and found that the NO emission index increased as the CME content in the fuel was increased.

Erazo et al. (2009) documented the combustion characteristics of spray flames of neat CME and diesel with an air-blast atomizer to study the effects of diferences in both chemical structure and physical properties. The coflow air was heated to a temperature of two-thirds of the end boiling point of the fuel. The CME spray flame was cooler by 200K than the diesel flame in the far-injector region. The CME spray flame had a lower global NO emission index and lower peak NO in-flame concentrations than the diesel flame. Habib et al. (2009) found that both the CO and NO emissions in a gas turbine engine were lower than those obtained with Jet-A fuel; the emissions were influencd by differences in physical and chemical properties and the engine operating parameters. Hashimoto et al. (2008) made similar observations when palm methyl ester was used in gas turbines. While compression ignition engine studies highlight an increase in NO emissions with the use of biofuels, investigations of spray-flames at atmospheric pressure and in gas turbine combustors report a decrease in NO emissions. The discrepancy is attributed to the large differences in pressure, temperature, and residence time, and flame structure between continuous combustors (such as gas turbines) and intermittent combustors (compression ignition engine configurations).

In summary, the documentation of the effects of blending of biofuels with petroleum fuels on emissions is limited and inconclusive in literature. Futhermore, the effects appear to vary non-monotonically with blend ratio; therefore, the combustion properties of blends cannot be extrapolated from those of the parent fuels. Also, the inlet mixture equivalence ratio plays a strong role in determining the dominant mechanism of NOx emission. These factors served as motivation for this study.

The present experimental investigation was aimed at understanding the combustion properties of spray flames of CME/diesel blends in a set-up similar to that of Erazo et al. (2009). These flames were turbulent, involving fuel atomization and drop evaporation, unlike the laminar flames of prevaporized fuels studied by Singh et al. (2013). The specific objectives of this research project were to measure the global emissions, in-flame emissions and temperature profiles in spray flames of blended CME and No. 2 diesel fuel at two inlet equivalence ratios.

Experimental Set-Up and Methods

A description of the experimental set-up, instrumentation, fuels and test conditions is provided in this section.

Experimental Set-Up

The experiments were conducted in a vertical steel test chamber with a cross section of 76 x 76 cm and a height of 100 cm. The top of the combustion chamber was connected to the outside atmosphere through an exhaust duct. The ambient pressure in the laboratory was maintained slightly (20 Pa) above the atmospheric pressure, to provide a positive draft inside the test chamber and eliminate leakage of the combustion products into the main laboratory facility. A schematic diagram of the setup is presented in Figure 1. Air was filtered and dehydrated and then passed through a 10 kW, three-phase co-flow air heater; the air temperature was controlled using a digital temperature controller. Insulated piping guided the air into a settling chamber filled with marbles in order to supply a stable uniform flow of air into the flame chamber. The flame chamber (10.2 cm width by 52 cm in height) was made of stainless steel with Vycor glass windows to facilitate visual access to the flame. An atomizing air system, a heated co-flow air system and a fuel tank were connected to the bottom of the flame chamber.
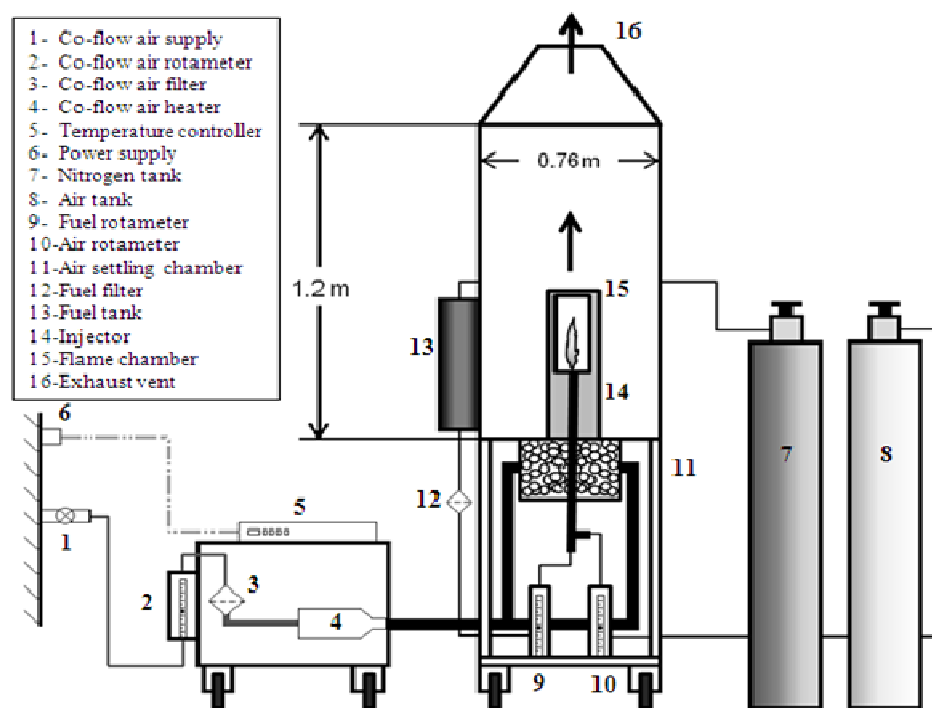
FIG. 1. SCHEMATIC DIAGRAM OF THE EXPERIMENTAL SET-UP

TABLE 1. FUEL PROPERTIES

Fuel	Molecular Formula	Density (kg/m³)	Viscosity at 20°C (cP)	LHV (MJ/kg)	Oxygen mass percentage (%)	Boiling point (°C)
Diesel	$C_{16}H_{34}$	850	2.19	42.6	0	150 - 350
CME B25	$C_{16.5}H_{34}O_{0.42}$	855	2.9	41.9	2.8	
CME B50	$C_{17.3}H_{34.3}O_{0.9}$	858	3.25	41.1	5.5	
CME B75	$C_{18}H_{34.4}O_{1.4}$	867	3.6	40.4	8.2	
CME	$C_{18.8}H_{34.6}O_{2}$	875	3.82	39.8	10.8	351 - 405

A partial swirl stainless steel air-blast atomizer with a 300 micron orifice diameter, served as the injector. The injector was vertically positioned at the tip of a 5 mm ID stainless steel tube providing the atomizing air through a concentric stainless steel pipe of 9 mm ID. The fuel tank was pressurized using a nitrogen cylinder at a pressure of 48 kPa; the atomizing air was supplied from an air cylinder. A swirling spray of fuel drops was formed at the exit of the atomizer; this spray was injected into a coflow of hot air. Additional details of the experimental set-up are provided by Aldana (2010).

Fuels

CME/diesel blends were used in different concentrations (B25, B50, B75), with the number denoting the percentage of volume of CME in the blend; for example B25 represents a blend with 25% CME and 75% diesel. The parent fuels were splash blended and vigorously stirred at room temperature. No noticeable separation of the blends was observed even after several months when stored at room temperature. The fuel properties are shown in Table 1. The oxygen content in the fuel increases with increase in CME concentration in the blend. Also, the heating value decreases as the CME concentration is increased because CME has a lower heating value (by about 10%) than diesel. The viscosity and upper boiling point temperature of CME are higher than those of diesel. The distillation curves presented by Alptekin and Canaci (2009) indicate that the boiling point range of the blends is between that of the pure fuels.

Test Conditions

The experiments were conducted at initial equivalence ratios (ϕ) of 0.62 and 0.75 to replicate lean burning conditions. The stoichiometric air-fuel ratio was calculated using the molecular formulas presented in Table 1 and assuming complete combustion (Aldana, 2010). With the atomizing and coflow air stream rates kept constant, the fuel flow rate was adjusted to set and maintain these equivalence ratios. The coflow air

temperature was maintained at a constant value of 250°C, equal to 66% of the midpoint of the boiling point range of pure CME. At these equivalence ratios, the presence of the hot coflow of air helped stabilize the flame. Morton et al. (2013) found that the spray flames were longer and corresponded to rich conditions ($\phi > 1$) without any coflow. A propane pilot flame (about 25 cm long) was used as the ignition source for all the flames, and was removed after the spray flame was stabilized.

Flame Visualization

Visible flame images were acquired using an 8 mega pixel digital AF SLR camera. The images were obtained under similar lighting conditions with a dark background. Using appropriate software, the number of pixels falling within the same cut-off intensity was counted and converted into visible flame length using a calibration reference.

Global Emission Measurements

Measurements of the volumetric concentration of CO, CO_2 and NO in the exhaust were carried out using a portable flue gas analyzer. The analyzer consisted of a built-in solid state infrared CO and CO_2 detector, and electrochemical sensors for measurement of O_2 and NO concentrations. A pyrex funnel with a height of 27 cm, bottom diameter of 16 cm and top diameter of 4 cm was mounted 7.5 cm above the flame chamber, where the flue gases were collected and guided to an uncooled quartz probe with a 1 mm. inner diameter orifice expanding to a 6 mm (inner diameter) tube. These gases were passed through a water condenser immersed in an ice bath, in order to protect the detectors and to report all the emission results on a dry basis, and then directed across a fiber filter to trap particulate matter before they were passed to the gas analyzer. The analyzer was calibrated with standard reference gas mixtures before measurements were taken. The following equation was used to convert the concentration measurements of CO and NO to their emission indices on a mass basis (g /kg of fuel) to compensate for dilution during sampling:

$$EI_i = [X_i/ (X_{CO} + X_{CO2})] [(N \, MW_i)/MW_f] \qquad (1)$$

Here X_i represents the mole fraction of species i, N is the number of carbon atoms in the mixture, and MW_i MW_f are the molecular weight of species i and fuel respectively. It is assumed that all the carbon in the fuel is converted into CO or CO_2; the assumption is reasonable because the soot liberation from the flames

was negligible (Turns, 2000).

Temperature Measurements

The in-flame temperature profiles were measured using an R-Type thermocouple with a bead diameter of 0.35 mm. Catalytic action was reduced by coating the tip of the thermocouple with a layer of silica using a flame incorporating silicone grease. This thermocouple was positioned along the length of the flame using a guided traverse mechanism. Data acquisition was accomplished using LabView software (National Instruments Co.). The temperature readings were sampled at a rate of 1 Hz and averaged over a period of 30 seconds and corrected for radiation and conduction losses (Aldana, 2010).

In-Flame Concentration Measurements

In-flame radial concentration profiles of CO, CO_2, O_2 and NO were measured using a flue gas analyzer, similar to that used for global emission measurement. A quartz 1 mm-tip diameter probe was guided at various axial locations using a traverse mechanism. The probe was connected to the water condenser to trap the water produced in the combustion process. Subsequently, the sample gas was passed through a coarse quartz fiber wool filter and a fine balsa fiber filter to trap soot particles, before passing the sample through the gas analyzer.

Results and Discussion

Flame Appearance

Photographs of the spray flames of the blends are presented in Figure 2. These pictures were taken with an exposure time of 1/25 second. The flames were turbulent and had a brushy appearance. At an equivalence ratio of 0.62, the flames were of comparable length (approximately 9 cm). With an increase in fuel flow rate, the flames became longer (about 12 cm) at an equivalence ratio of 0.75. The flames contained a large luminous yellow region preceded by a small bluish region near the injector (Aldana, 2010), which appear as white and light gray regions in the black-white versions presented here. The near-injector gray zone represents the area in which fuel pyrolysis, soot formation, and primary gas-phase oxidation reaction occurred. Both the oxygen that was organically bound with the fuel in biofuels and the oxygen in the air-supply stream helped in the gas-phase oxidation. The unburned soot continued to grow and burn downstream with the additional

oxygen in the entrained air; the continuum radiation from the burning soot particles gave the flames a luminous yellow hue. The CME in the fuel blend had two significant effects on the flame appearance. First, the luminosity of the flame was reduced as the content of CME in the blend was increased, indicating a reduction in the soot content in the flames (Singh et al., 2013). Second, the near-injector gray zones (that appeared blue in color photographs) became longer with increased volumetric content of CME due to the increase in oxygen content of the fuel blend (Table 1).
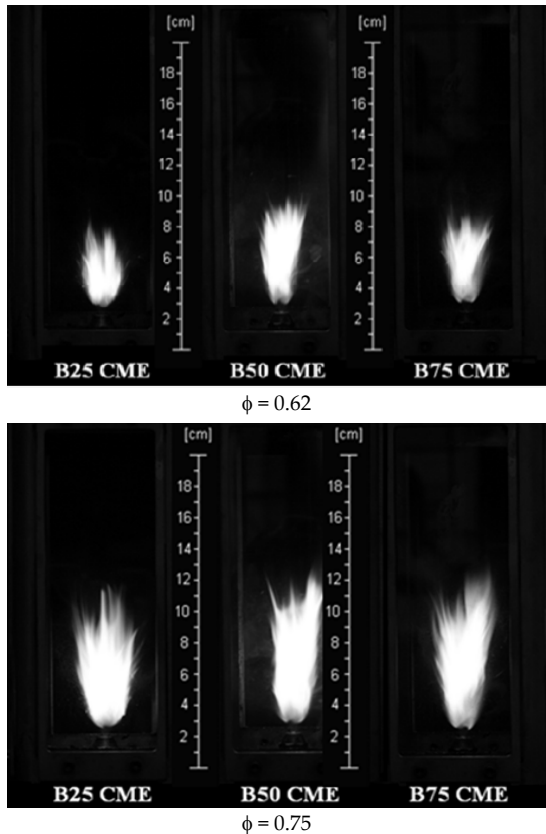
FIG.2. PHOTOGRAPHS OF SPRAY FLAMES

Global Emissions

The global NO and CO emission indices are presented for the two equivalence ratios in Figure 3. It is observed that both the concentration of CME and the equivalence ratio affect the emission indices significantly. The NO emission index is primarily dependent on the flame temperature distribution, which is significantly affected by the soot content. At ϕ = 0.62, the NO emission index decreased markedly as the volumetric content of CME in the blend was increased from 0 to 75%. This observation, although is in contrast to the results obtained from studies in diesel engines, agrees with the results obtained in previous continuous spray combustion studies discussed in the introduction. It is possible that the

emission index results from diesel engines (intermittent combustion where ignition delay plays a dominant role) and spray flames (continuous combustion without significant ignition delay) would agree if the ignition delay effects present in the former were compensated. Since the heating value decreased with the CME concentration in the blend (Table 1), the NO emission index decreased from 85.2 g/MJ for diesel to 16.2 g/MJ for B75 at this equivalence ratio.
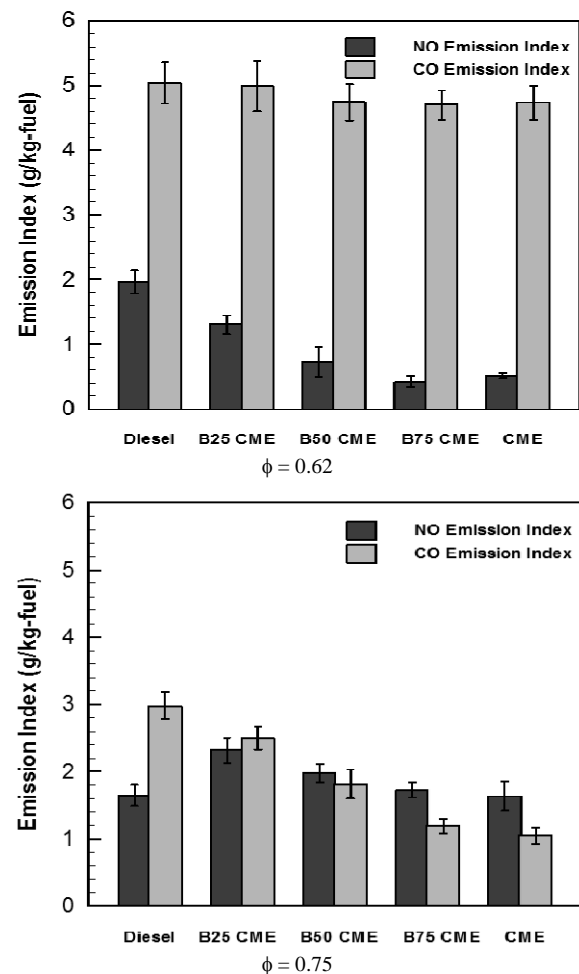
FIG.3. COMPARISON OF NO AND CO EMISSION INDICES OF DIFFERENT FLAMES

The NO emission index of the blends was higher compared to that of diesel as the equivalence ratio was increased to 0.75 because the overall conditions were closer to stoichiometric conditions; this observation agrees with compression-ignition engine exhaust results. In this case, the B25 blend flame had the highest NOx emission index (100.6 g/MJ) compared to the lowest value for the diesel flame (68.2 g/MJ). Thus, at this equivalence ratio, the NO emission index varied by less than 42% among the various flames. This condition is typical of fuel-air mixtures at higher loads of the engines which are also accompanied by higher soot emissions. Soot burning in the far-nozzle region

could have two counteracting effects: the competition for oxygen could reduce NO formation locally; however, an increase in local flame temperature could lead to increased thermal NO formation. It appears that the higher soot formation accompanying the high equivalence ratios cannot be compensated by the reduction in soot due to the increased oxygen content of the biofuel blend and the change in flame temperature caused by a reduction in the soot content. Furthermore, at the equivalence ratio of 0.75, the radiation effect overshadows the oxygen abstraction by the soot. Interestingly, at this condition, the NO emission index was highest for the B25 flame and the values were comparable for the CME, B50 and B75 diesel flames. The differences in the soot content and soot properties between these flames resulting in similar temperature profiles could be a reason for this behavior.

At ϕ = 0.62, the CO emission index decreased only slightly (by 6%) as the volumetric content of CME in the blend was increased from 0 to 75%. The increased

oxygen content in the fuel with CME concentration would be expected to result in more complete combustion leading to less CO formation. However, the additional oxygen also leads to significant local leaning of the mixtures, causing partial quenching of the CO oxidation reactions. At the higher equivalence ratio, the CO emission index was lowered with the biofuel content of the blend. The effectiveness of the fuel-bound oxygen in the formationof soot precursors in the near-injector region and subsequent lower degree of soot oxidation of CO is evident at this condition. Interestingly, a monotonic decrease in the CO emission index with the CME content in the fuel was observed.

In-Flame Concentration

The radial profiles of the in-flame concentrations of CO, CO_2 and O_2 at 25% flame height are presented in Figure 4. This region is of substantial importance in forming soot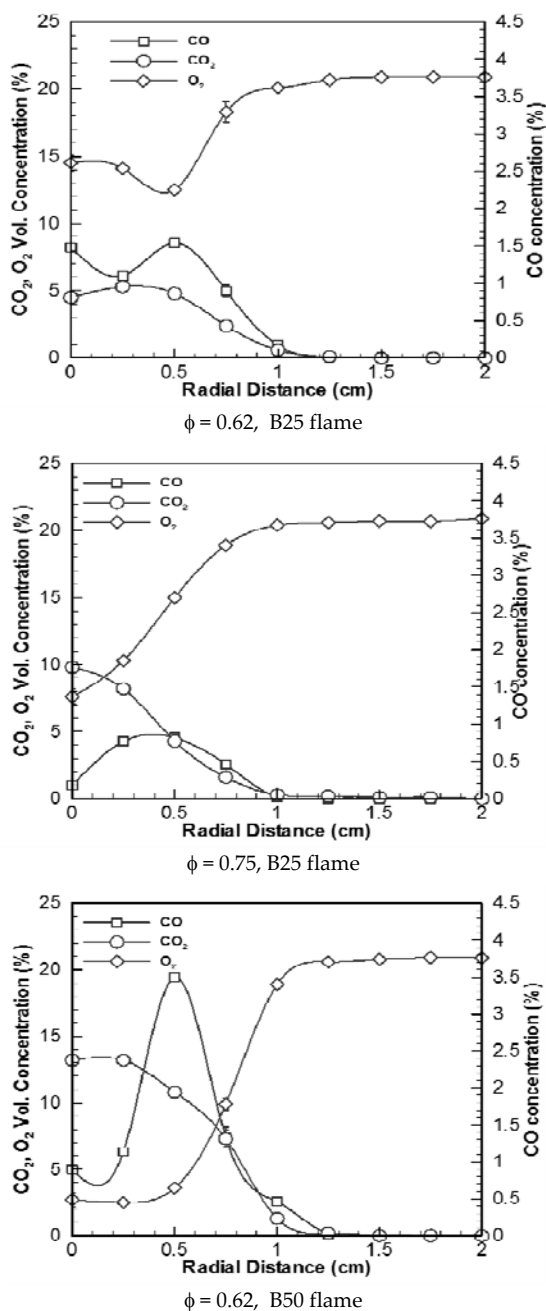 precursors and oxidation of pyrolysis fragments, and consequently is cricial to determine what occurs in the rest of the flame. These profiles indicate the presence of a reaction zone that was located about 4-6 mm away from the centerline (as seen in a minimum value of the oxygen concentration and a maximum value of CO concentration). At ϕ = 0.62, the oxygen concentration was high at the centerline in the B25 flame and the CO_2 concentration was low (peak value of 5%). The B25 fuel had the

highest diesel content with the most amount of soot pre-cursors. At 25% flame height, only a small amount of oxidation of the fuel had occurred, and the CO and CO_2 concentrations were low. In contrast, a significantly higher peak concentration of CO was observed in the B50 flame. The B50 fuel had more CME content with more fuel-bound oxygen and less diesel than B25. The fuel-bound oxygen enabled the conversion of fuel carbon to CO and CO_2. The B75 flame had the least amount of diesel and the most fuel-bound oxygen, resulting in an increase in the oxygen concentration near the centerline (than the B50 flame) and a reduction in CO and CO_2 concentration. Thus, these measurements highlight the effectiveness of fuel-bound oxygen in the oxidation reactions.

ϕ = 0.62, B25 flame

ϕ = 0.75, B25 flame

ϕ = 0.62, B50 flame

$\phi = 0.75$, B50 flame

$\phi = 0.62$, B75 flame

$\phi = 0.75$, B75 flame
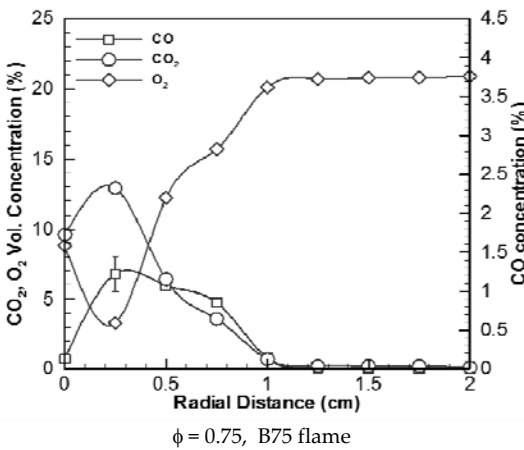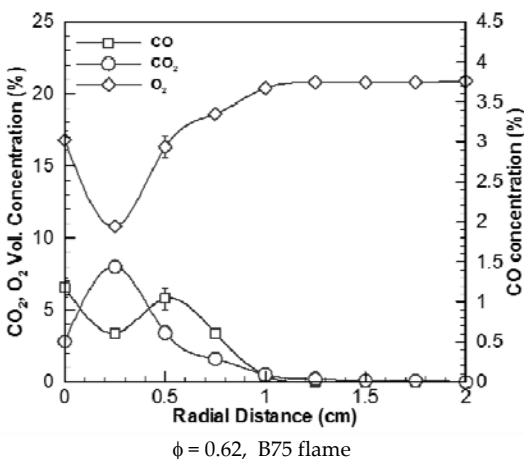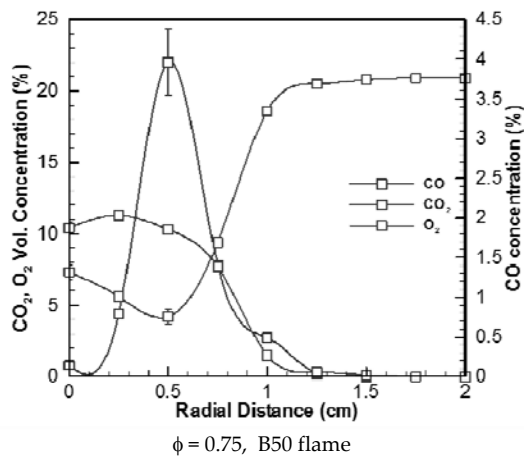
FIG.4. RADIAL NO CONCENTRATION PROFILES AT 25%
FLAME HEIGHT IN THE FLAMES

As the equivalence ratio was increased (by increasing the fuel flow rate), the oxygen concentration near the centerline became lower and the CO_2 concentration increased in the B25 flame. The B50 flame again had a high peak CO concentration, whereas the B75 flame had lower CO and CO_2 concentrations than the B50 flame. At 50% and 75% flame heights, the peak CO_2 concentration and the minimum O_2 concentration shifted to the axis due to entrainment and mixing. Those results are provided by Aldana (2010) and are not given here for the sake of brevity.

The NO concentration profiles along with the temperature profiles at 25% flame height are presented in Figure 5. At 25% flame height, the peak temperatures and peak NO concentrations were located off-axis (where the reaction zone was located). At $\phi = 0.62$, the B25 flame had a significantly higher NO concentration than the B50 and B75 flames (confirming the global NO emission index measurements presented in Fig. 3); the peak temperature was also slightly higher for the B25 flame. Overall, the NO concentration profiles were similar to the temperature profiles, suggesting that the thermal mechanism of NO formation was dominant in these flames.

$\phi = 0.62$, B25 flame

$\phi = 0.75$, B25 flame

$\phi = 0.62$, B50 flame

φ = 0.75, B50 flame

φ = 0.62, B75 flame

φ = 0.62, B75 flame
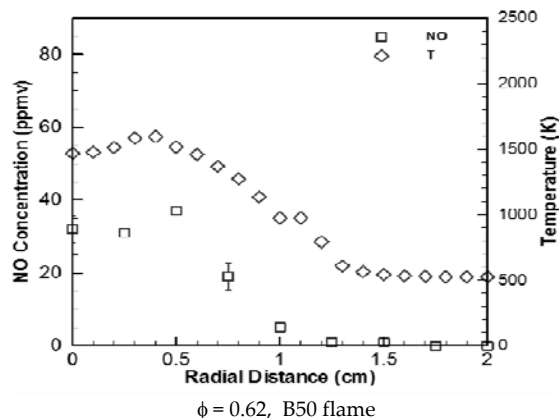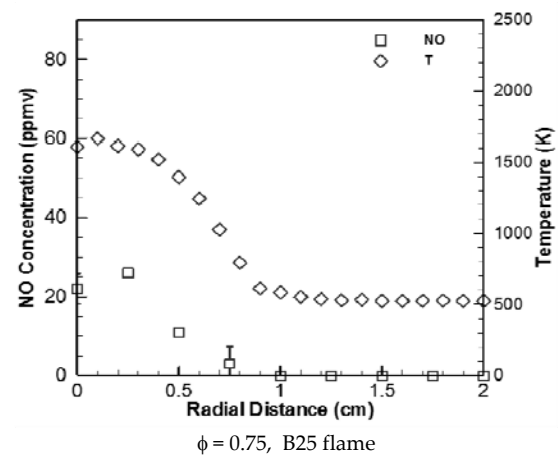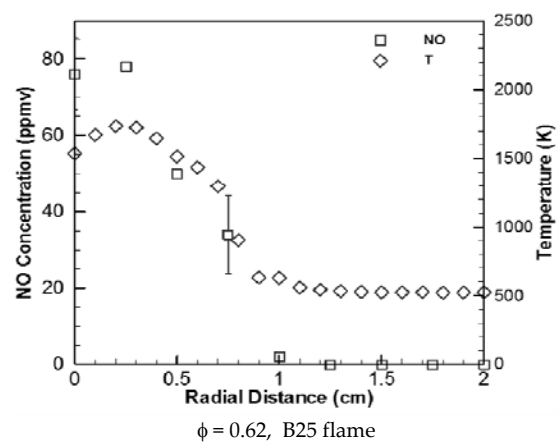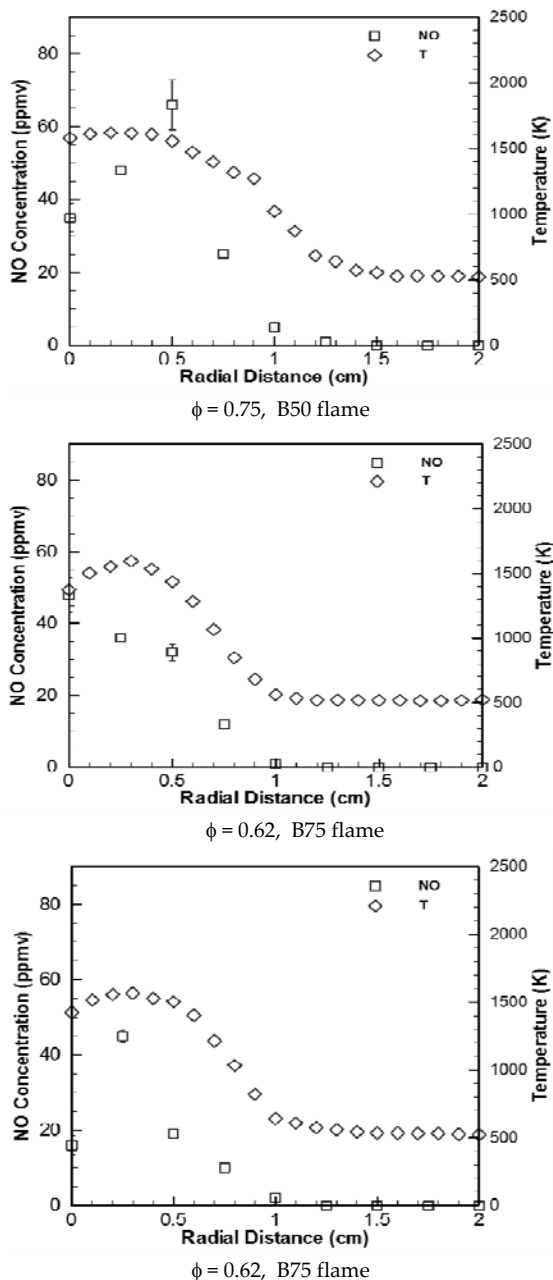
FIG.5. RADIAL NO CONCENTRATION AND TEMPERATURE
PROFILES AT 25% FLAME HEIGHT IN THE FLAMES

When the equivalence ratio was increased to 0.75, the peak temperatures did not change significantly. The soot content in the flames was higher due to an increase in the carbon input rate. In this case, the B50 flame had the highest NO concentration. Again, the NO concentration profiles were similar to the temperature profiles. At higher flame locations, the peak NO concentration shifted to the centerline and the peak concentrations were lower than those measured at 25% flame height (Aldana, 2010).

Conclusions

In summary, spray flames of CME/diesel blends were

studied at an initial supply equivalence ratio of 0.62 and 0.75. Measurements of global CO and NO emissions and in-flame temperatures and concentrations were made. Based on the measurements, the following conclusions were drawn:

1. The flame luminosity decreased with an increase in CME concentration indicating a reduction in the soot content; the homogenous gas-phase reaction region near the injector became larger as the CME concentration was increased.

2. At φ = 0.62, the global NO emission index decreased significantly as the CME concentration was increased from 0 to 75%. However, the pure diesel flame had the highest NO emission index at φ = 0.75.

3. The global CO emission index did not vary significantly with the increase in CME concentration at φ = 0.62 and decreased with CME content at φ = 0.75.

4. The effects of biofuel content of blends on NO and CO emission indices were strongly coupled to the inlet equivalence ratio.

REFERENCES

Aldana, C., 2010, "Combustion Properties of Spray Flames of Soy Methyl Ester and Canola Methyl Ester Blended with No. 2 Diesel Fuel," M. S. Thesis, School of Aerospace and Mechanical Engineering, University of Oklahoma, Norman, Oklahoma.

Alptekin, E. and Canakci, M. "Characterization of the key fuel properties of methyl ester-diesel fuel blends," Fuel 88 (2009):75-80.

Bari, S. "Performance, Combustion and Emission Tests of a Metro-bus Running on Biodiesel-ULSD Blended (B20) Fuel," Applied Energy 124 (2014): 35-43.

Canakci M. and Van Gerpen, J. "Comparison of Engine Performance and Emissions for Petroleum Diesel Fuel, Yellow Grease Biofuel and Soybean oil Biofuel" Transactions of the American Society of Agricultural and Biological Engineers 46 (2003): 937–944.

Erazo, J., Parthasarathy, R. N. and Gollahalli, S. R.

"Atomization and Combustion of Canola Methyl Ester Fuel Spray." Fuel 42 (2010): 3735-3742.

Fontaras, G. , Kousoulidou, M., Karavalakis, G., Tzamkiozis, T., Pistikopoulos, P., Ntziachristos, L, Bakeas, E., Stournas, S., and Samaras, Z. "Effects of Low Concentration Biodiesel Blend Application on Modern Passenger Cars. Part 1: Feedstock Impact on Regulated Pollutants, Fuel Consumption and Particle Emissions." Environmental Pollution 158 (2010): 1451-1460.

Habib, Z., Parthasarathy, R. N. and Gollahalli, S. R. "Performance and Emission of a Small Scale Gas Turbine Engine Fueled with Biofuels." Applied Energy 87 (2010): 1701-1709.

Hashimoto, N., Ozawa, Y., Mori, N., Yuri, I and Hismatsu, T. "Fundamental Combustion Characteristics of Palm Methyl Ester (PME) as Alternative Fuel for Gas Turbines." Fuel 87 (2008): 3373-3378.

Labeckas, G. and Slavinskas, S. "The Effect of Rapeseed Oil Methyl Ester on Direct Injection Engine Performance and Exhaust Emissions." Energy Conversion and Management 47 (2006): 1954-1967.

Love N., Parthasarathy R. and Gollahalli S. "Effect of Iodine Number on NO Formation in Laminar Flames of Oxygenated Biofuels." International Journal of Green Energy 6 (2009): 323-332.

Morton, C., Tran, V., Parthasarathy, R. N. and Gollahalli, S. R. "Combustion Characteristics of Spray Flames of Canola Methyl Ester/Diesel Blends in a Furnace." International Mechanical Engineering Congress and Exposition, IMECE2013-63004, San Diego, California.

Schumacher L., Marshall W., Krahl J., Wetherell W. and Grabowski M. "Biofuel Emissions Data from Series 60 DDC Engines." Transactions of the American Society of Agricultural and Biological Engineers 44 (2001): 1465–1468.

Singh, V. N., Parthasarathy, R. N. and Gollahalli, S. R. "Radiation and Emission Characteristics of Laminar Partially Premixed Flames of Petroleum Diesel-Canola Methyl Ester Blends." Journal of Petroleum Science Research 2 (2013): 97-103.

Song, H., Tompkins, B., Bittle, J. and Jacobs, T. "Comparisons of NO Emissions and Soot Concentrations from Biodiesel-Fuelled Diesel Engine" Fuel 96 (2012): 446-453.

Tsai, J., Chen, S., Huang, K., Lin, Y., Lee, W., Lin, C., Lin, W. "PM, Carbon and PAH Emissions From a Diesel Generator Fuelled with Soy-Biodiesel Blends" Journal of Hazardous Materials 179 (2010): 237-243.

Turns S.. An Introduction to Combustion: Concepts and Applications, 2nd Edition, McGraw-Hill, 2000.

An Integrated Approach for the Application of the Enhanced Oil Recovery Projects

Mahmoud Abu El Ela*[1], Helmy Sayyouh[2], El Sayed El Tayeb[3]

Petroleum Engineering Department, Faculty of Engineering, Cairo University, Giza, Egypt

*[1]Mahmoud.abuelela@worleyparsons.com; [2]sayyouh@gmail.com; [3]sayed_eltayeb6262@yahoo.com

Abstract

This work presents an integrated approach for screening and application of the most suitable enhanced oil recovery (EOR) method to the oil fields. The proposed approach can be used to support the decision making during the critical technology selection phase. By providing early stage advice through detailed design, the approach can provide a bridging service to bring the EOR projects from screening and laboratory stages into the field applications.

EOR screening for some of the Egyptian oil fields is presented. The screening procedure and criteria are based on field results and previous experiences, and involve the analysis of both surface and subsurface fields' conditions. The results indicate that the most appropriate EOR methods for the studied oil fields appear to be CO_2 and alkali-surfactant-polymer injection methods. The study shows that CO_2-EOR could help Egypt simultaneously to reduce the emissions of CO_2 and increase the recovery factor by 5 to 15 %.

The study then identifies the main technological barriers to the implementation of CO_2-EOR, and indicates key areas that require further research and development. In addition, the challenges and the main technical concerns in applying CO_2-EOR technologies are discussed in the light of the lessons learnt from large scale worldwide EOR projects.

Such study is an original contribution to achieve successful EOR applications and could significantly increase the reserves of the mature oil fields.

Introduction

Although technical challenges and costs have often precluded many oil companies from adopting EOR methods, it has quickly become more feasible and is expected to continue to grow rapidly with ongoing investment. Oil-production from EOR projects continues to supply an increasing percentage of the world's oil. About 3% of the worldwide production now comes from EOR (Abu El Ela, 2008; Taber et al., 1997). Fig. 1 shows the number of EOR projects according to 2004, 2010, 2012 and 2014 Oil and Gas Journal worldwide survey (Moritis, 2004; Moritis, 2010; Koottungal, 2012; Koottungal, 2014).
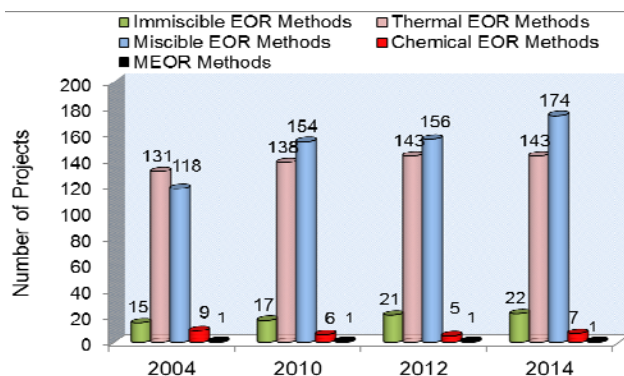
FIG. 1 EOR PROJECTS WORLDWIDE IN 2004, 2010, 2012 AND 2014

It is clear from Fig. 1 that the miscible flooding and thermal methods are the most widely used EOR recovery processes. The number of miscible flooding projects increases from 118 projects in 2004 to reach 174 projects in 2014. The thermal methods projects increases from 131 projects in 2004 to be 143 projects in 2014. The number of projects of these technologies is expected to continue to grow due to the availability of the proven technology. Fig. 1 indicates also that the immiscible EOR processes increase slowly from 15 projects in 2004 to be 22 projects in 2014; but the chemical EOR methods ranges between 7 to 9 projects during the same duration. To date, chemical flooding has had limited application due to the high ongoing cost of associated chemicals, concerns about environmental impacts and the failure of selected

laboratory successes to translate into significant production gains when applied to operating fields.

Miscible flooding includes several methods: CO_2 injection, nitrogen injection and hydrocarbon injection. Miscible processes aim at achieving miscibility by eliminating the interface between injected fluid and residual oil through a process of mass transfer between the two fluids. The miscibility is dependent on reservoir pressure and temperature and on the compositions of the injected fluid and crude oil. The first-contact miscibility is achieved when the injected fluid and the crude oil mix in all proportions and result in single phase mixtures. The multi-contact miscibility is achieved due to the gradual transfer of molecules between the injected fluid and the crude oil, thereby eliminating capillary forces completely. A ternary diagram is a simplified way to examine the phase behavior of an injection fluid with the crude oil. Different gases reach miscibility with the crude oil at different minimum miscibility pressure (MMP) levels. While CO_2 is effective in most crude oils, its volume requirement is much higher due to its high solubility in water. For medium and light oils in deep formation, CO_2 miscible displacement processes are the best to be applied. N_2 flooding has been an effective recovery process for deep, high-pressure, and light oil reservoirs. Generally for these types of reservoirs, N_2 flooding can reach miscible conditions. However, immiscible N_2 injection has also been used for pressure maintenance, cycling of condensate reservoirs, and as a drive gas for miscible slugs (Alvarado and Manrique, 2010; Manrique and Muci, 2007; Terry, 2001).

Thermal methods are often the best for recovering heavy oil. The world contains about 10 trillion bbl of heavy oil resources (Farouq Ali et al., 1997). However, Egypt has about 3 billion bbl of heavy oil in place with about 40% in the Eastern desert, 3% in the Western desert, 18% in Sinai, and 39% in the Gulf of Suez (Abu El Ela, 2008; EGPC, 2007). The thermal methods provide a driving force and heat for reducing oil viscosity (Alvarez and Han, 2013). These methods such as steam injection, hot water injection, or in situ combustion are well established for shallow reservoirs (due to thermal loss as well as its lower latent heat content at elevated pressures) containing heavy viscous oil, which would otherwise not be recovered.

Cyclic-steam stimulation involves injecting steam and then producing oil for the same well. One of the advantages of using steam injection is that this method

needs moderate investments (Abu El Ela, 2008). It can be used to enhance recovery from the nearby wellbore and can be used for paraffin removal from the wellbore. Today, cyclic steam injection is regarded as a well-established oil recovery method, which will become increasingly important in the years to come. Well stimulation by Huff-&-Puff is a widely used process due to its low front-end cost, ease of steam generation, low operating cost, and quick pay-out. In Cold Lake, Alberta, recovery is over 25% or higher. Venezuela has nearly two trillion barrels of heavy oil. In Venezuela, cycling steaming is a well established and recoveries from this process as high as 40% have been noted (Farouq Ali et al., 1997). Cyclic steam stimulation has also been very successful in several countries including USA, Canada, Egypt, Syria and Oman. The first filed applied cyclic steam stimulation in Egypt is Issran field. It is located in the eastern desert of Egypt (Abu El Ela, 2008).

Continuous steam flooding, much like waterflooding, is a pattern drive, with arrays of injection and production wells. In this case, the performance is strongly dependent on the pattern size, since heat loss to the surrounding rocks can consume a large proportion of the injected heat. Steam is continuously injected into the injector, resulting in the formation of steam zone, which advances at an ever-decreasing rate. Steam overrides due to gravity. Steam reduces the oil saturation within the steam zone to very low values, of the order of 10% (Farouq Ali et al., 1997). When steam breakthrough occurs, the steam injection rate is reduced to a value that is enough to supply the heat loss. At a later time steam is discontinued, and hot water may be injected.

Hot waterflooding is seldom employed and has limited field applications because heat losses in surface lines, wellbore and formation, are greater than the heat losses in the other thermal processes. The heat losses in the hot waterflood cause a large drop in temperature and reduce its effectiveness in decreasing the oil viscosity. Steam flooding is preferred over hot water flooding for many reasons; the higher heat content is the primary reason. Steam flooding results in incremental oil recovery due to a combination of viscosity reduction and steam distillation and reforming.

In-situ combustion process is conducted within the reservoir aiming at generating heat inside the reservoir pore space through a spontaneous combustion by the injection of air. This process is

therefore more efficient in terms of effective heat transfer, compared with the steam flooding or Huff & Puff steam stimulation process. This increased temperature reduces crude oil viscosity as well as generates other heat-associated benefits such as thermal expansion and crude cracking, distillation, and reformatting. The process has a high thermal efficiency, but this process requires more control.

Chemical EOR methods are mostly suitable for low to medium viscosity oils. These processes include surfactant-flooding, polymer-flooding, and alkaline-flooding. Polymer flooding is considered a mature technology and still the most important EOR chemical method based on the review of full-field case histories (Alvarado and Manrique, 2010). Polymer flooding is suited for reservoirs where normal waterfloods fail due to one of the two reasons: High heterogeneity and high oil¬ water mobility ratio. The addition of polymer to water increases the water viscosity and/or plugs the high-permeability zones of the reservoir rock and thus improves the water mobility. The improvement in the water mobility reduces the fingering and increases the areal sweep efficiency. Polymer floods mainly target oil in areas of the reservoir that have not been contacted efficiently. Thereby, they reduce the detrimental effect of vertical permeability variation (causing low vertical sweep) and facieses variation (causing low areal sweep) on recovery efficiency. Polymers are also used in many EOR projects to provide mobility control behind the injected chemical slug.

In the alkaline-waterflooding, the reaction between the caustic solution and certain organic acids present in some crude oils results in the formation of soaps which enhances the emulsification and the resulting emulsions reduce the interfacial tension. Also, the rock wettability may be altered by the reaction of the caustic solution with the reservoir rock. This wettability change results in the increase of oil recovery. The caustic flooding, utilizing a slug of dilute caustic solution chased by injection water, is useful only in reservoirs with crude oil of high acid number.

Surfactant flooding utilizes a dilute surfactant solution in place of water. Micellar flooding utilizes a slug of micellar solution (a solution of oil, water, surfactant, and co-surfactant) that is chased by a slug of dilute polymer solution alone or in combination with water. While this method is simple, its use has not been very successful due to slug breakdown. Slug breakdown is due to: loss of chemical from rock adsorption and dispersive mixing with the reservoir fluids.

The injections of alkali, surfactant, alkali-polymer (AP), surfactant-polymer (SP) and Alkali-Surfactant-Polymer (ASP) have been tested in a limited number of fields. The high salinity and temperature of the oil reservoir formations impose a serous limitation on the use of micellar and polymer floods. High values of formation water salinity and temperature cause problems in degradation, difficulty of designing stable surfactant/polymers systems; and/ or consumption of the chemicals used in the process. The salinity should be less than 200,000 ppm and temperature should be less than 200°F (Taber et al., 1997; Sayyouh and Al-Blehed, 1990). In addition to the salinity and temperature, reservoir heterogeneity is another critical parameter. Most chemical EOR methods are applicable preferably, to sandstone reservoirs, not for extensive fractures and or extreme reservoir heterogeneity.

The application of microbial techniques to improve oil recovery has been termed Microbial Enhanced Oil Recovery (MEOR). The idea behind this technology is that the microbes consume nutrients such as molasses and produce biomass and various metabolic products such as biopolymers, biosurfactants, solvents, and gases. Some of these metabolic products or the biomass help to mobilize residual oil from depleted petroleum reservoirs. The potential of the MEOR technology has been evaluated in the laboratory by studies that have demonstrated the growth of candidate cultures at simulated reservoir conditions. These experiments were expanded to include model core flooding tests which demonstrated that oil release by microbial action was successful. However, field-testing remains the final criterion for evaluating the potential of MEOR technology to become a successful tertiary recovery method.

Recently, a new technology of using the electro treatment has been developed to improve the oil recovery. The electro treatment technology is based on the effects of changing the cavitated spatial pattern within the soil of a reservoir and spacious structure of two-phase liquid filtration (oil & water) in the reservoir as a result of repeated cycles of electric pulses. These treatments can increase the oil recovery by 10 to 30%; however, it is still under research and development stage.

Approach for the Application of the EOR Projects

Fig. 2 presents the general approach for the

application of the EOR project to a specific reservoir. The proposed approach is a lengthy process and involves several phases and stages. Each stage is discussed in this section.

Data Management

Making smart reservoir development plan depends on the ability to collect, analyze and integrate the available data from the disciplines of geology, geophysics, economics, reservoir and production engineering. The challenges are to know when to integrate and at what level the integration should take place.

Preliminary Screening

Not all fields are amenable to EOR processes. Effective screening practices must be employed to identify suitable candidates. EOR processes are rather difficult and high risk operations. The important question is:

how much oil can be recovered and what techniques could be applied under what cost? Therefore, comparison and assessment of the field properties and characteristics against the EOR screening criteria should be performed to determine the most suitable EOR technologies that can be applied to improve the oil recovery from the field. Numerous parameters should be carefully studied in order to assess the applicability of various EOR methods. Remaining oil saturation is perhaps the most critical criterion in selecting the EOR method. The choice also depends on such considerations as depth, oil viscosity, reservoir pressure and temperature, water salinity, rock type, thickness, porosity, permeability etc. Table 1 can be used as a guide for the preliminary screening (Taber et al., 1997). Screening criteria are useful for many candidate reservoirs before expensive reservoir descriptions and economic evaluations are done.

TABLE 1 SUMMARY OF THE EOR SCREENING CRITERIA (TABER ET AL., 1997)

	Oil Properties			Reservoir Characteristics					
EOR Method	Gravity (°API)	Viscosity (cp)	Composition	Oil Saturation (% PV)	Formation Type	Net Thickness (ft)	Average Permeability (md)	Depth (ft)	Temperature (°F)
Nitrogen and flue gas	>35↑ 48↑	< 0.4↓ 0.2↓	High percent of C1 to C7	>40↑ 75↑	Sandstone carbonate	Thin unless dipping	NC	> 6,000	NC
Hydrocarbon	>23↑ 41↑	<3↓ 0.5↓	High percent of C2 to C7	>30↑ 80↑	Sandstone carbonate	Thin unless dipping	NC	> 4,000	NC
CO2	>22↑ 36↑a	<10↓ 1.5↓	High percent of C5 to C12	>20↑ 55↑	Sandstone carbonate	Wide range	NC	> 2,500a	NC
Immiscible gases	>12	< 600	NC	>35↑ 70↑	NC	NC if dipping and/or good vertical permeability	NC	> 1,800	NC
Miceller/ Polymer, ASP, and Alkaline Flooding	>20↑ 35↑	<35↓ 13↓	Light, intermediate, some organic acids for alkaline floods	>35↑ 53↑	Sandstone preferred	NC	>10↑ 450↑	> 9,000↓ 3,250	> 200↓ 80
Polymer Flooding	>15	< 150, > 10	NC	>50↑ 80↑	Sandstone preferred	NC	>10↑ 800↑	< 9,000	> 200↓ 40
Combustion	>10↑ 16	< 5,000 - 1,200	Some asphaltic components	>50↑ 72↑	High-porosity sand/ sandstone	>10	>50	<11,500↓ 3,500	> 100↑ 135
Steam	> 8 to 13.5- >	< 200,000 - 4,700	NC	>40↑ 66↑	High-porosity sand/ sandstone	>20	>200↑ 2,540↑	< 4,500↓ 1,500	NC

N.C.: Not Critical   MMP: Minimum Miscibility Pressure
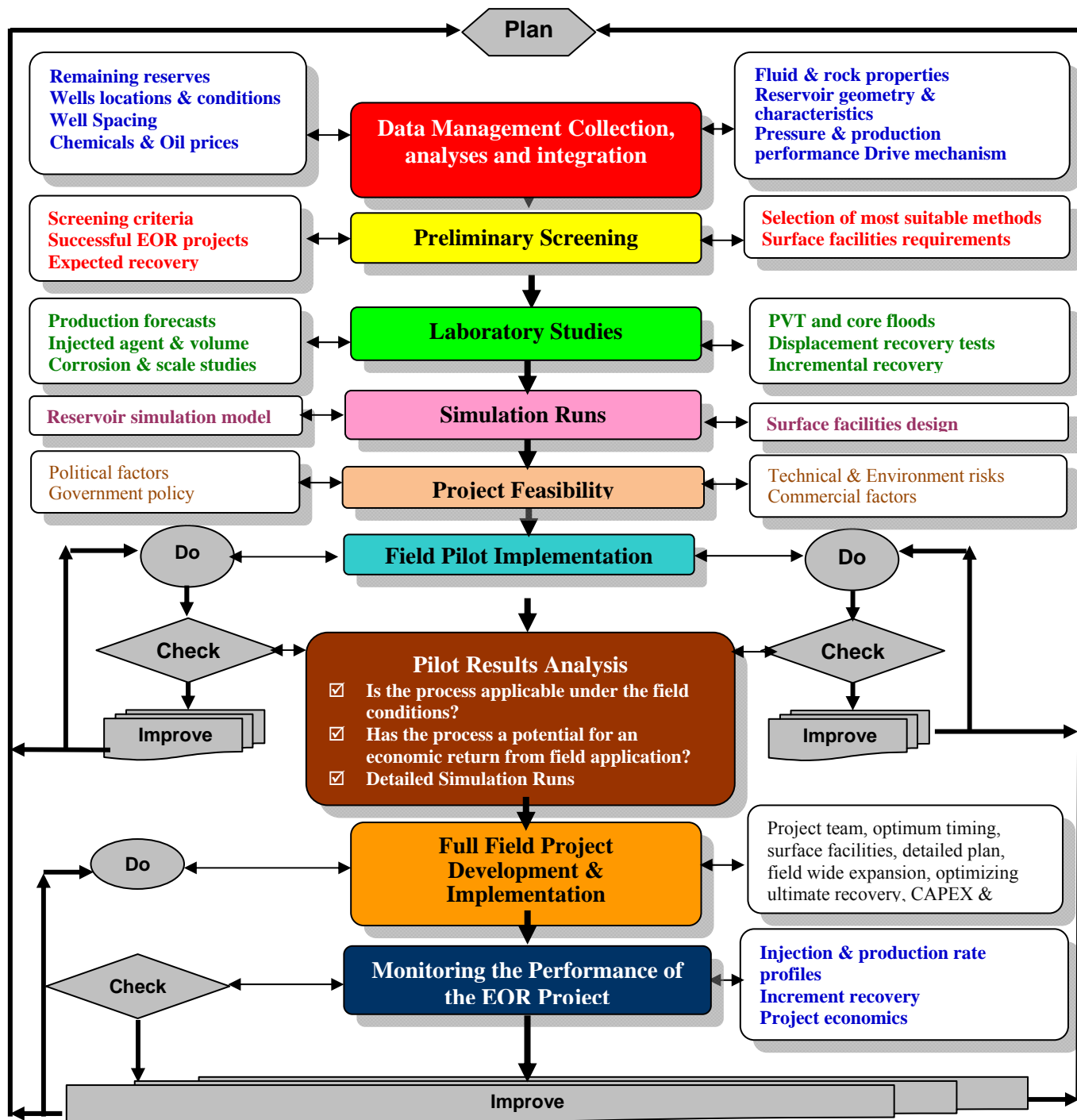
FIG. 2 DESIGN AND IMPLEMENTATION STEPS OF A COMPREHENSIVE EOR PROGRAM

Table 2 presents the results of a preliminary screening that nominate and recommend the most suitable EOR technologies to some of the Egyptian oil fields in the Western Desert (Abu El Ela, Mahmoud et al., 2013). The screening is carried out using specialized software (EOR Graphical User Interface – EORgui). Through the use of the EORgui software, the oil fields and reservoirs are screened and the potential of applying the EOR techniques is identified. Fig. 3 presents a sample of EORgui results for one of the reservoir. The coloring scheme in Fig. 3 is simply based on the degree

in which the criteria are met or not. Namely, if a cell is colored red, then this criterion is not met. Whereas, if a cell is colored light green, then the criterion is just met. However, if the cell is colored dark green, then the criterion is well met. Table 2 indicates that the most appropriate EOR methods for the studied oil fields appear to be CO_2 injection, immiscible gas injection and Alkali-Surfactant-Polymer/Polymer-Surfactant injection. Based on the history of the successful EOR projects results, the CO_2 injection (miscible flooding) seems to be the most appropriate EOR methods.

TABLE 2 SUMMARY OF THE SCREENING CRITERIA RESULTS FOR SOME OF THE EGYPTIAN OIL FIELDS IN THE WESTERN DESERT

No	Field Name	Reservoir	OOIP (bbl)	Remaining OIP (bbl)	Depth (mt)	Initial Pressure (MPa)	Current Pressure (MPa)	Temperature (°C)	° API	Viscosity (cp)	Most Suitable EOR Methods
1	CYG	UPPER Bah	13,300,000	12,645,000	1981	n/a	177	85	33	1.5	CO2MF, IMM
2		LOWER Bah	8,400,000	8,145,000	2286	n/a	183	87	33	1.5	CO2MF, IMM
3	BED15	ARC	38,000,000	21,900,000	3200	4750	1800	111	34	0.65	CO2MF
4	BED3C9	ARG	9,000,000	7,900,000	3400	5000	3000	116	42.2	0.25	CO2MF
5	BED3-8/3-13	ARC	11,000,000	7,500,000	3000	4363	2400	112	35	0.25	CO2MF
6	BED3-6/3-11	ARC	3,500,000	2,400,000	2875	4750	730	107	38	0.32	CO2MF
7	BED-1	ARC	15,800,000	14,200,000	2852	4273	1250	109	36.3	0.68	CO2MF
8		ARD	9,900,000	8,300,000	2960	4295	1405	113	33.8	0.8	CO2MF
9		Kharita	149,000,000	73,500,000	3600	5283	4500	128	40.6	0.5	CO2MF
10		Bahariya	33,000,000	28,400,000	3390	5200	1575	121	39.9	0.22	CO2MF
11	BED-9	Bahariya	12,000,000	11,400,000	3230	5000	3200	121	36.2	0.36	CO2MF
12	BAHGA	A.R.G	22,400,000	21,000,000	2812	4150	1400	114	33.2	1.14	CO2MF
13		L. Bah	9,000,000	8,560,000	3113	4497	3200	121	35.9	0.63	CO2MF
14	AL MAGD	North AR G"	4,390,000	4,210,000	3048	4494	1750	114	33.2	0.95	CO2MF
15		South A/R"G"	4,050,000	3,960,000	3044	4494	2185	114	33.2	0.95	CO2MF
16	AL BARQ	A/R"E"	16,100,000	15,730,000	2990	4520	2549	112	38.7	0.48	CO2MF
17		A/R "G"	16,100,000	15,730,000	3182	4818	2549	112	31.8	2.1	CO2MF
18	KARAM	ARC	10,000,000	9,910,000	4220	8000	5500	149	38.7	0.32	CO2MF
19	ASSIL	A/R "G"	32,000,000	32,000,000	3870	6887.5	6888	124	38.6	0.45	CO2MF
20		Bahariya	71,000,000	71,000,000	4074	6080	6080	128	9	0.45	N/A
21	AL FADL	Bahariya	73,000,000	70,010,000	1200	1770	1370	64	40.2	0.17	CO2MF, IMM, ASP
22	AL QADR	Bahariya	23,000,000	21,460,000	1200	1754	900	64	41.2	1.5	CO2MF, IMM, ASP
23	NEAG2	Bahariya	10,000,000	8,770,000	2600	3924	3912	96	42.8	0.87	CO2MF
24	NEAG2 EAST	Bahariya	7,000,000	7,000,000	2600	3922	3922	97	42.4	0.87	CO2MF
25	NEAG3	Bahariya	4,000,000	3,070,000	2513	3759	3751	92	41	0.87	CO2MF
26	JG (JD-2BLOCK)	LSA-East	60,000,000	53,220,000	3235	4865	2391	113	42	0.6	CO2MF
27	JG	LSA- West	22,000,000	16,820,000	3235	4827	224	114	37.5	0.77	CO2MF
28	JG(JD-7BLOCK)	LAC- West	10,000,000	7,090,000	3235	4846	4700	112	38	0.7	CO2MF
29	JG(JD-10BLOCK)	LSC- East	6,000,000	4,570,000	3235	4857	4700	112	33	0.5	CO2MF
30	JG	LSB	2,000,000	1,910,000	3260	4577	2523	112	38	0.6	CO2MF
31	SHIBA	Bahariya	8,000,000	7,200,000	2054	3050	0	96	36	0.6	CO2MF
32	SITRA-8 BLOCK	A.R.C	19,000,000	16,800,000	2860	4193	1800	109	29	0.4	CO2MF
33		A.R.C	8,000,000	7,830,000	2895	4240	3600	110	39	0.32	CO2MF
34		ARG Sand1	19,000,000	18,170,000	3270	4886	1500	127	31	1.29	CO2MF
35		ARG Sand2	15,000,000	14,490,000	3270	4886	2060	127	31	1.29	CO2MF
36		ARE	7,000,000	6,210,000	3070	4438	2100	114	39	0.5	CO2MF
37		UPPER Bah	12,000,000	11,500,000	3410	5121	1600	124	40	0.36	CO2MF

OOIP: Original Oil in Place   OIP: Oil in Place   ASP: Alkali-Surfactant-Polymer   IMM: Immiscible EOR method

CO2MF: CO_2 Miscible flooding

* The data of the fields were collected by the students of the Natural Gas Engineering Diploma at Cairo University - July 2012

Recent Files ▼

Title	BAPETCO (ASSIL-A/R "G")

API Gravity	38.6	Formation	Sandstone ▼	Depth [feet]	12693.6
Oil viscosity [cP]	.45	Thickness	> 20 ft With Dip ▼	Temperature [deg F]	255.2
Oil Saturation, fraction	.35	Composition	High % C5-C12 ▼	Permeability [mD]	30

Summary Screening | **Detail**

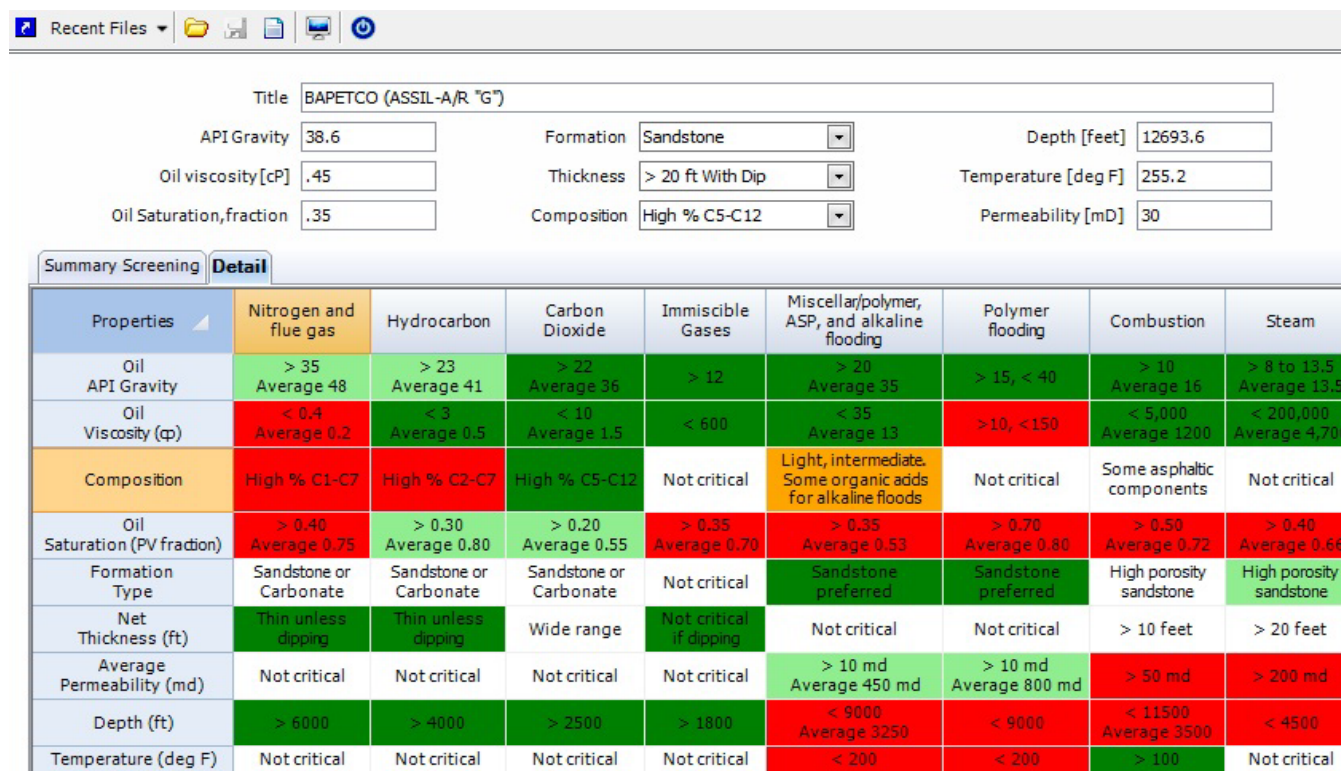| Properties	Nitrogen and flue gas	Hydrocarbon	Carbon Dioxide	Immiscible Gases	Miscellar/polymer, ASP, and alkaline flooding	Polymer flooding	Combustion	Steam
Oil API Gravity	> 35 Average 48	> 23 Average 41	> 22 Average 36	> 12	> 20 Average 35	> 15, < 40	> 10 Average 16	> 8 to 13.5 Average 13.5
Oil Viscosity (cp)	< 0.4 Average 0.2	< 3 Average 0.5	< 10 Average 1.5	< 600	< 35 Average 13	>10, <150	< 5,000 Average 1200	< 200,000 Average 4,700
Composition	High % C1-C7	High % C2-C7	High % C5-C12	Not critical	Light, intermediate. Some organic acids for alkaline floods	Not critical	Some asphaltic components	Not critical
Oil Saturation (PV fraction)	> 0.40 Average 0.75	> 0.30 Average 0.80	> 0.20 Average 0.55	> 0.35 Average 0.70	> 0.35 Average 0.53	> 0.70 Average 0.80	> 0.50 Average 0.72	> 0.40 Average 0.66
Formation Type	Sandstone or Carbonate	Sandstone or Carbonate	Sandstone or Carbonate	Not critical	Sandstone preferred	Sandstone preferred	High porosity sandstone	High porosity sandstone
Net Thickness (ft)	Thin unless dipping	Thin unless dipping	Wide range	Not critical if dipping	Not critical	Not critical	> 10 feet	> 20 feet
Average Permeability (md)	Not critical	Not critical	Not critical	Not critical	> 10 md Average 450 md	> 10 md Average 800 md	> 50 md	> 200 md
Depth (ft)	> 6000	> 4000	> 2500	> 1800	< 9000 Average 3250	< 9000	< 11500 Average 3500	< 4500
Temperature (deg F)	Not critical	Not critical	Not critical	Not critical	< 200	< 200	> 100	Not critical

FIG. 3 SCREENING CRITERIA RESULTS FOR APPLYING EOR TECHNOLOGIES TO ASSIL FIELD - ARG FORMATION

Experience from worldwide operations has demonstrated that the use of CO_2-EOR can increase oil recovery by 5% to 15% beyond what is achievable when using conventional recovery methods (Carcoana, 1992; Donaldson at al., 1985). The exact increased recovery fraction depends on the injection method used and the characteristics of each oil reservoir and crude oil it contains. In addition to the additional oil recovery, CO_2-EOR could help Egypt simultaneously reduce the emissions of CO_2 which are produced from several sources such as power plant. Power plant of 140 MW produces one million tons of CO_2 per year (Tzimas et al., 2005).

The classification of fields as potentially being suited to miscible flooding, immiscible displacement or chemical processes is very preliminary. More detailed field evaluation would be required for a more definitive assessment of the most appropriate technique to be deployed in a specific field. Some general considerations should be studied before the individual process screening criteria are carried out. First, detailed geological study is usually desirable, since operators have found that unexpected reservoir heterogeneities have led to the failure of many EOR field projects. Reservoirs that are found to be highly faulted or fractured typically yield poor recoveries from EOR processes. Second, some general comments pertaining to economics can be made. When an operator is considering EOR in particular applications, candidate reservoirs should contain sufficient recoverable oil and be large enough for the project to be potentially profitable. Also, deep reservoirs could involve large drilling and completion expenses if new wells are to be drilled. In addition, the available surface facilities, equipment and piping should be also taken into considerations during the screening phase and selection of the most suitable EOR method for a specific field (Abu El Ela, 2012; Abu El Ela, 2013).

The EOR method selection requires a life cycle analysis of the capital and operating expenditure (CAPEX/OPEX) trade-offs together with the required technical skills to prepare the project for the implementation phases. During the preliminary screening phase, preliminary commercial evaluation is conducted. The economic evaluation depends on different parameters such as the expected market prices, OPEX, CAPEX, cost recovery, cash flow, and profit share.

Laboratory Studies

Based on the results of the preliminary screening study, several laboratory studies should be run to evaluate and assess the performance of the selected EOR method. The laboratory studies are undertaken to estimate incremental oil recovery as a function of the injected volume and other process variables. The

relative permeability and displacement recovery tests on representative cores are conducted under simulated reservoir conditions. The physical properties of the system as related to injected agents are also established. The expected corrosion and scale problems to the surface piping and equipment should be carefully studied and analyzed.

Simulation Study

The reservoir simulation model, capable of mimicking reservoir dynamics as well as the chemical/physical interaction between injection fluid and oil, is a must for planning the full pilot and field project. In this phase, all EOR project design parameters as injectors/producers pattern - type of injection – pilot plant design… etc are highlighted. At the end of this phase, the production performance for several scenarios will guide to expect and identify the optimal hydrocarbon recovery and the required production facilities such as pipelines, processing units and storage tanks.

Project Feasibility

Selecting the best and the most feasible EOR technique to improve the recovery is carried out by comparing the net revenue of each proposed scenario. The net revenue for each proposed scenario depends on (1) the production performance and (2) the economic evaluation. Potential technical risks along with the commercial factors (sources of capital; economic selection criteria; market availability; price of oil; risk tolerance); political factors (economic climatic; issues of safety/security/stability; manpower and technology availability); and government policy (long-term focus; short-term objectives; conservation; posterity concerns; and; employment focus) are also identified and studied. Then, the necessary recommendations for pilot field application are drawn.

Field Pilot Implementation

The EOR technique should be tailored to the reservoir to ensure the efficiency of the selected EOR method in the field. It is specific for a specific reservoir. Field pilot is designed and conducted as a small scale project.

Pilot Performance Monitoring and Detailed Simulation Studies

The surface and subsurface design parameters along with the pilot response results are monitored, studied, analysed and interpreted. The pilot provides much-needed information for the final design and provides results that are very useful in fine ¬tuning of the reservoir simulation model. Then, the technical and commercial evaluation for the full field development plan is carried out. The technical evaluation will consider the following: existing wells location, fluid distribution, chemicals requirements, surface facilities requirements, preliminary sizing of the required equipment, associated risk..etc.

Full Field Project Development and Implementation

Field wide expansion follows a successful pilot project. This is the maturity phase of the project. In this phase, the detailed plan to maximize efficient production from the field while optimizing ultimate recovery in a practical timeframe is developed and implemented. The following design parameters are considered:

- Location of the existing facilities
- Capacity and process description of the existing plant
- Layout of the area to define the accessibility of the future expansion of the existing facilities
- Existing pipeline: size, length, maximum and minimum flow rate, battery limits, life time, turn down ratio of the existing pipeline
- The existing utilities: source of the power generation and the maximum producing power
- The available capacities of the existing storage tanks

Challenges and Main Technical Concerns in Applying EOR Technologies

Because of differences in density and viscosity between the injected fluid and the reservoir fluid(s), the miscible process often suffers from poor mobility. Viscous fingering and gravity override frequently occur. The simultaneous injection of a miscible agent and brine was suggested in order to take advantage of the high microscopic displacement efficiency of the miscible process and the high macroscopic displacement efficiency of a waterflood. The improvement was not as good as hoped since the miscible agent and brine tended to separate due to density differences, with the miscible agent flowing along the top of the porous medium and the brine along the bottom.

Several variations of the simultaneous injection scheme have been suggested and researched. They

typically involve the injection of a miscible agent followed by brine or the alternating of miscible agent–brine injection. The latter variation has been named the WAG (water alternate gas) process and has become the most popular. A balance between amounts of injected water and gas must be achieved. Too much gas will lead to viscous fingering and gravity override of the gas, whereas too much water could lead to the trapping of reservoir oil by the water. The addition of foam-generating substances to the brine phase has been suggested as a way to aid in reducing the mobility of the gas phase. Research is continuing in this area. Operational problems involving miscible processes include transportation of the miscible flooding agent, corrosion of equipment and tubing, and separation and recycling of the miscible flooding agent. Therefore, the available surface facilities should be taken into considerations as it has a big impact on CAPEX and OPEX of the miscible flooding project.

The most critical parameter with respect to miscible CO_2 flooding is the Minimum Miscibility Pressure (MMP). The MMP is required so that CO_2 becomes fully miscible with oil. The MMP depends on the composition of crude oil, the purity of CO_2 and the reservoir conditions (pressure and temperature). Hence, a miscible CO_2-dispacement technique can only be implemented when CO_2 can be injected at a pressure higher than that of MMP, which in turn must be lower than the reservoir pressure. In summary, low values for MMP, necessary for the applicability of the process to a large number of oilfields, are favored by (Tzimas et al., 2005):

- High CO2 densities, e.g. 0.4-0.75 g/cm3, necessary to achieve miscibility in the C5 to C30 hydrocarbons of the crude oil.

- Low temperature to maximize CO2 density

- Light and medium crude oils (lighter than 22°API) with a low concentration of aromatics.

- High CO_2 purity, since the presence of nitrogen, sulphur, SOX, NOx and other contaminants in the CO_2 stream increases MMP. This has significant implications for the required purity of CO_2 captured from combustion plants for EOR use.

Preferably, the injection pressure at the start of a CO_2 flood should be at least 14 bar above the MMP to achieve miscibility of CO_2 and reservoir oil. This means that the ratio between reservoir pressure and minimum miscible pressure (P/MMP) normally should be greater than 1, but CO_2 flood EOR is still possible for P/MMP greater than 0.9 (Terry, 2001).

Because of the uncertainties of both calculation of MMP and measured pressure data, reservoirs with P/MMP greater than 0.9 are regarded as suitable for CO_2 floods by this screening if the reservoir pressure is lower than the original reservoir pressure at the start of CO_2 injection. The MMP can nowadays be measured experimentally or predicted using empirical equations and thermodynamic modeling with a very good accuracy. Table 3 presents the commonly used CO_2–oil MMP correlations and models (Cronquist, 1978; Lee, 1979; Yellig and Metcalfe, 1980; Alston et al., 1985; Emera and Sarma, 2005; Glaso, 1985). The correlations approach are useful for screening reservoirs for suitability for miscible processes, specially, if there is sufficient margin in the operating pressure to allow for the potential error in correlation estimates. However, the pressure required for dynamic miscibility with CO_2 is determined from displacement experiments.

The main technical problems associated with thermal techniques are poor sweep efficiencies, loss of heat energy to unproductive zones underground and poor injectivity of steam or air. Poor sweep efficiencies are due to the density differences between the injected fluids and the reservoir crude oils. The lighter steam or air tends to rise to the top of the formation and bypass large portions of crude oil. Data have been reported from field projects in which coring operations have revealed significant differences in residual oil saturations in the top and bottom parts of the swept formation. Research is being conducted on methods of reducing the tendency for the injected fluids to override the reservoir oil. Techniques involving foams are being employed (Terry, 2001).

Large heat losses continue to be associated with thermal processes. The wet combustion process has lowered these losses for the higher-temperature combustion techniques, but the losses are severe enough in many applications to prohibit the combustion process. The losses are not as large with the steam processes because they involve smaller temperatures.

Steam flooding projects suffer from low sweep due to the formation of fingers and gravity override. The poor injectivity found in thermal processes is largely a result of the nature of the reservoir crudes. Operators have applied fracture technology in connection with the injection of fluids in thermal processes. This has helped in many reservoirs. Operational problems

include the following: the formation of emulsions, the corrosion of injection and production tubing and facilities, and the creation of adverse effects on the environment. When emulsions are formed with heavy crude oil, they are very difficult to break. Operators need to be prepared for this. In the high-temperature environments created in the combustion processes and when water and stack gases mix in the production wells and facilities, corrosion becomes a serious problem. Special well liners are often required. Stack gases also pose environmental concerns in both steam and combustion applications. Stack gases are formed when steam is generated by either coal- or oil-fired generators and, of course, during the combustion process as the crude is burned.

The main technical challenges associated with chemical processes include the following: (1) screening chemicals to optimize the microscopic displacement efficiency, (2) making contact with the oil in the reservoir, and (3) maintaining good mobility in order to lessen the effects of viscous fingering.

TABLE 3 COMMONLY USED CO_2–OIL MMP CORRELATIONS AND MODELS

Correlations/Model		Remarks
Cronquist (1978)	$MMP = 0.11027 - (1.8T_R+32)^Y$, Where, $Y = 0.744206 + 0.0011038*MW_{C5+} + 0.0015279*Vol$	The tested oil gravity ranged from 23.7 to 44°API. • The tested T_R ranged from 21.67 to 120°C. • The tested experimental MMP ranged from 7.4- 34.5 MPa.
Lee (1979)	$MMP = 7.3924 - 10^b$ Where, $b = 2.772 - (1519/(492+1.8 T_R))$	• Based on equating MMP with CO2 vapour pressure when T_R < CO2 critical temperature, while using the corresponding correlation when $T_R \geq$ CO2 critical temperature. • If MMP<P_b , the P_b is taken as MMP.
Yellig and Metcalfe (1980)	$MMP = 12.6472 + 0.015531*(1.8 T_R+32) + 1.24192*10^{-4}*(1.8T_R+32)^2 - 716.9427/(1.8T_R+32)$	• Limitations: 35° C $\leq T_R$<88.9°C • If MMP<P_b , the P_b is taken as MMP.
Alston et al. (1985)	$MMP = 6.056*10^{-6}*(1.8 T_R +32)^{1.06}*(MW_{C5+})^{1.78}*(Volatiles/interm.)^{0.136}$ When P_b<0.345 MPa, $MMP = 6.056*10^{-6}*(1.8T_R+32)^{1.06}*(MW_{C5+})^{1.78}$	• If MMP<P_b , the P_b is taken as MMP.
Genetic Algorithm Based Alston et al. Correlations (2005)	$MMP = 5.0093*10^{-6}*(1.8 T_R +32)^{1.164}*(MW_{C5+})^{1.2785}*(Volatiles/interm.)^{0.1073}$ When P_b<0.345 MPa, $MMP = 5.0093*10^{-6}*(1.8 T_R +32)^{1.164}*(MW_{C5+})^{1.2785}$	• Genetic Algorithm Based Alston et al. Correlations
Glaso's (1985) Original	When F_R > 18 mol% $MMP = 5:58657 - 0.02347739*MW_{C7+} + (1.1725*10^{-11}*MW_{C7+}^{3.73}*e$ ^$(786.8*MW_{C7+}^{-1.058})*(1.8 T_R +32))$ When F_R < 18 mol% $MMP = 20.33 - 0.02347739*MW_{C7+} + (1.1725*10^{-11}*MW_{C7+}^{3.73}*e$ ^$(786.8*MW_{C7+}^{-1.058})*(1.8 T_R +32)) -0.836*F_R$	• Considers the effect of intermediates (C2–C6) only when: F_R (C2–C6)<18 mol%
Genetic Algorithm Based Glaso Correlations (2005)	When F_R > 18 mol% $MMP = 474265308 - 0.0187974*MW_{C7+} + (278.6388*10^{-11}*MW_{C7+}^{3.023}*e$ ^$(803.9*MW_{C7+}^{-1.189})*(1.8 T_R +32))$ When F_R < 18 mol% $MMP = 9.690285 - 0.01817494*MW_{C7+} + (278.6388*10^{-11}*MW_{C7+}^{3.023}*e$ ^$(803.9*MW_{C7+}^{-1.189})*(1.8 T_R +32)) - 0.44796015*F_R$	Genetic Algorithm Based Glaso Correlations
F_R	: Mole percent C2 through C6 in the reservoir fluid, %	
Interm.	: Intermediates components, C1 –C4, H2S, and CO2, fraction	
MMP	: Minimum miscibility pressure, MPa	
MW_{C5+}	: Molecular weight of C5+ fraction	
MW_{C7+}	: Molecular weight of C7+ fraction	
P_b	: Bubble point pressure, MPa	
T_R	: Reservoir temperature, °C	
Vol.	: Mole percentage of the volatiles (C1 and N2), %	
Volatiles	: Volatile components, C1 and N2, fraction	

The requirements for screening of chemicals vary with the type of process. Obviously, as the number of components increases, the more complicated the screening procedure becomes. The chemicals must also be able to tolerate the environment they are placed in. High temperature and salinity may limit the chemicals that could be used.

The major problem experienced in the field to date in chemical flooding processes has been the inability to make contact with residual oil. Laboratory screening procedures have developed micellar–polymer systems that have displacement efficiencies approaching 100% when sand packs or uniform consolidated sandstones are used as the porous medium. When the same micellar–polymer system is applied in an actual reservoir rock sample, however, the efficiencies are usually lowered significantly. This is due to the heterogeneities in the reservoir samples. When the process is applied to the reservoir, the efficiencies become even worse. Research is being conducted on methods to reduce the effect of the rock heterogeneities and to improve the displacement efficiencies.

Mobility research is also being conducted to improve displacement sweep efficiencies. If good mobility is not maintained, the displacing fluid front will not be effective in making contact with residual oil. Polymers are subject to mechanical breakage, shear degradation, temperature sensitivity, and bacterial decay. Selection of right polymer for right application is very important. Some polymer solutions exhibit rate-sensitive behaviour. Some polymers exhibit increased effective viscosity while flowing in a reservoir. Adsorption of polymer by rock is a major design consideration.

Operational problems involve treating the water used to make up the chemical systems, mixing the chemicals to maintain proper chemical compositions, plugging the formation with particular chemicals such as polymers, dealing with the consumption of chemicals due to adsorption and mechanical shear and other processing steps, and creating emulsions in the production facilities.

Conclusions

- The general approach for the application of the EOR project to a specific reservoir is a lengthy process and involves several phases and stages.

- Each stage in the proposed approach is presented and explained

- A preliminary screening that nominate and recommend the most suitable EOR technologies to some of the Egyptian oil fields in the Western Desert is provided

- The most appropriate EOR methods for the studied Egyptian oil fields appear to be CO_2 injection, immiscible gas injection and Alkali-Surfactant-Polymer /Polymer-Surfactant injection. Based on the history of the successful EOR projects results, the CO_2 injection (miscible flooding) seems to be the most appropriate EOR methods.

- The challenges and the main technical concerns in applying EOR technologies in Egypt are presented.

REFERENCES

Abu El Ela, Mahmoud et al. "CO2 Use Could Boost Egypt's Western Desert Oil Recovery," Oil & Gas Journal, Volume 111, Issue 9, September 02, 2013.

Abu El Ela, Mahmoud et al. "Thermal heavy-oil recovery projects succeeded in Egypt, Syria" OGJ, Volume 106, Issue 48, December 22, 2008.

Abu El Ela, Mahmoud. "Egypt's Tut Field Candidate for CO_2 Miscible Flooding," OGJ, Volume 111, Issue 1, Jan. 07, 2013.

Abu El Ela, Mahmoud. "Egyptian Fields Have Large Potential For Enhanced Oil Recovery Technology," OGJ, Volume 110, Issue 10, October 1, 2012.

Alston, R.B. et al. "CO_2 Minimum Miscibility Pressure: a Correlation for Impure CO_2 Streams and Live Oil Systems," SPEJ, p. 268, April 1985.

Alvarado, Vladimir and Manrique, Eduardo. "Enhanced Oil Recovery: An Update Review," Energies, Volume 3, Issue 9, p. 1529, August 27, 2010.

Alvarez, Johannes and Han, Sungyun. "Current Overview of Cyclic Steam Injection Process," Journal of Petroleum Science Research (JPSR), Volume 2, Issue 3, July 2013.

Carcoana, Aurel. Applied Enhanced Oil Recovery, Prentice-Hall, Inc., 1992.

Cronquist, C. "Carbon Dioxide Dynamic Displacement with Light Reservoir Oils," Paper presented at the 1978 U.S. DOE, Annual Symposium, Tulsa, Aug. 28–30, 1978.

Donaldson, Erle C. et al. Enhanced Oil Recovery:

Fundamentals and Analysis, New York: Elsevier Science Publishing Co. Inc., 1985.

EGPC, Oil Potential in Egypt: Statistics & Analysis, EGPC, Sixth Technology Transfer Workshop, SPE Egypt Section, Cairo, May 2007.

Emera, Mohamed Kamal and Sarma, Hemanta K."Use of Genetic Algorithm to Estimate CO_2–Oil Minimum Miscibility Pressure—a Key Parameter in Design of CO_2 Miscible Flood," Journal of Petroleum Science and Engineering, Volume 46, p.37, 2005.

Farouq Ali, Syed Muhammad et al. Practical Heavy Oil Recovery, draft Volume, 1997.

Glaso, Oistein. "Generalized Minimum Miscibility Pressure Correlation," SPEJ, p. 927, Dec. 1985.

Koottungal, Leena. "2012 Worldwide EOR Survey," OGJ, Volume 110, Issue 4, April 2, 2012.

Koottungal, Leena. "2014 Worldwide EOR Survey," OGJ, Volume 112, Issue 5, May 5, 2014.

Lee, J.I., "Effectiveness of Carbon Dioxide Displacement under Miscible and Immiscible Conditions," Report RR-40, Petroleum Recovery Inst., Calgary, March, 1979.

Manrique, Eduardo Jose et al. "EOR Field Experiences in Carbonate Reservoirs in the United States," Paper No. SPE 100063-PA, SPE Reservoir Evaluation & Engineering Journal, Volume 10, No. 6, p. 667, Dec. 2007.

Moritis, Guntis. "2004 Worldwide EOR Survey," OGJ, Volume 102, Issue 14, p. 53, April 12, 2004.

Moritis, Guntis. "2010 Worldwide EOR Survey," OGJ, Volume 108, Issue 14, p. 41, April 19, 2010.

Natural Gas Engineering Diploma, Graduation Project Reports, Mining Studies and Research Center (MSRC), Cairo University, 2012.

Sayyouh, Mohamed Helmy and Al-Blehed, Mohamed. "Screening Criteria for Enhanced Recovery of Saudi Crude Oils," Energy Sources, Vol. 12, Issue 1, p. 71. 1990.

Taber, Joseph John et al. "EOR Screening Criteria Revisited - Part 1: Introduction to Screening Criteria and Enhanced Recovery Field Projects," Paper No. SPE 35385-PA, SPE Reservoir Engineering Journal, Volume 12, Number 3, p.189, August 1997.

Terry, Ronald E. "Enhanced Oil Recovery," In Encyclopedia of Physical Science and Technology, 3rd Edition, Vol. 18, Robert A. Meyers Ed., Academic Press, p. 503-518, 2001.

Tzimas, E. et al. "Enhanced Oil Recovery using Carbon Dioxide in the European Energy System," Report EUR 21895 EN, European Commission, Directorate General, Joint Research Centre, Institute for Energy, Petten, The Netherlands, December 2005.

Yellig, W.F., Metcalfe, R.S., "Determination and Prediction of CO_2 Minimum Miscibility Pressures," JPT, Jan. 1980.

Mahmoud Abu El Ela is an associate professor at the Petroleum Engineering Department, Cairo University, Egypt, and works also as a manager of projects "Acting" at WorleyParsons Engineers Egypt Ltd. Previously, he was a lead process engineer at WorleyParsons, assistant professor at the Petroleum Engineering Department at Cairo University, petroleum process consulting engineer for Khalda Petroleum Co., and a research engineer at Woodside Research Foundation (Curtin University of Technology, Australia). Since 1997, he has been a technical consultant in petroleum engineering for national and international companies. Abu El Ela holds a B.Sc. and M.Sc. in petroleum engineering from Cairo University, and a Ph.D. from Curtin University of Technology. He is a member of the Egyptian Engineers Syndicate and SPE.

Helmy Sayyouh is a professor in the petroleum engineering department, Cairo University. He is a consultant with Petroleum and Petrochemicals Engineering Consultants (PPEC) Group and Mining Studies and Research Center (MSRC) - Cairo University. He teaches training courses with OGCI-PetroSkills-USA. Since 1986, he has been a consulting engineer in the areas of petroleum reservoir engineering, enhanced oil recovery, reservoir simulation, and natural gas engineering. He was a consultant in Geisum Oil Company from 1995-96 and an active member in the Egyptian National Petroleum High Committee from 1995-2000 with the objective of proposing and evaluating means of maximizing recovery and optimizing production from Egyptian fields, and identifying and solving common problems faced by oil companies. He has B.Sc. and M.Sc. degrees in petroleum engineering from Cairo University-Egypt and a PhD from Penn State University-USA. Dr. Helmy supervised more than 50 M.Sc. and Ph.D. thesis. He published over 100 technical papers in specialized international journals and conference proceedings all over the world.

El Sayed El-Tayeb is a professor in the petroleum engineering department, Cairo University; and also works as a professor within Petroleum and Petrochemicals Engineering Consultants (PPEC) Group - Cairo University. He is the director of the

Mining Studies & Research Center (MSRC) at Cairo University. Since 1998, he has been a Consultant Engineer in the areas of petroleum reservoir engineering and enhanced oil recovery. El-Tayeb holds a BSc and MSc in petroleum engineering from Cairo University and a PhD from Laboratories des Sciences du Genie Chimique, ENSIC Nancy University - Nancy – France. He is a member of the Egyptian Engineers Syndicate and SPE.

A New Method of Productivity Model for Coal-bed Methane under Steady-state Based on Equivalent Continuous Media Theory

Xiao Cong[*1], Mingjin Liu[2], Tian Leng[3], Zhao Chao[4], Yanchen Wang[5]

[*1,3,4] China University of petroleum, Department of Petroleum Engineering, Beijing, 102249, China

[2,5] Souehwest University of petroleum, Department of Geoscience and Technology, Sichuan, 610500, China

[*1]987558984@qq.com; [2]1271357688@qq.com; [3]860036980@qq.com; [4]zhaochao0716@qq.com; [5]571143293@qq.com

Abstract

Multi-stage fractured horizontal well technology is applied to develop Coal-bed methane reservoir, besides, due to the existence of adsorption, desorption and diffusion in coal pore media, the seepage mechanisms of coal-bed methane are different from conventional gas reservoirs. It can induce large errors to analyze coal-bed methane with conventional binomial production equation. Therefore, in terms of natural fracturing coal-bed methane reservoir, this paper firstly establishes the equivalent continuous medium model with consideration of adsorption, diffusion and the anisotropy of fracture permeability, matrix permeability and gas diffusion parameter using parallel-plate theory, equivalent seepage resistance principle and equivalent continuous medium principle. As a result, the dual porosity fractured coal-bed methane reservoir is equivalent to a homogeneous gas reservoirs characterized with a certain equivalent permeability. By giving special values of the relevant parameters, the new model proposed in this paper can be simplified to a variety of conventional gas reservoirs. Some inflow performance relationship (IPR) curves of multi-stage fractured horizontal well are plotted. When considering the impact of desorption and diffusion of coal-bed methane, these curves are different from conventional gas reservoirs ,the smaller the Langmuir pressure , the deeper the curve concaves and the bigger the absolute open-flow rate, moreover, the smaller the Langmuir volume , the deeper the curve concaves and the smaller the absolute open-flow rate. Through the actual comparative analysis, the error of this model is less than 15% and this model has certain practical value.

Keywords

Coal-bed Methane; Adsorption; Diffusion; Parallel-Plate Theory; Equivalent Permeability; Steady State; IPR Curve

Introduction

Coal-bed methane (CBM) reservoirs are typically unconventional reservoirs, which consist of complex natural fractures network (Li Song, 2011, Wu Shiyue, 1999, Kong Qingli, 2012, Wu Xiaomin, 1995, Yang Chaopeng, 2013, Kan Yili, 2003). The pore media in coal-bed methane reservoir contain matrix pore and cleat (Karn FS, 1996, Spivey JP, 1995). Multi-fractured horizontal well currently has been proved to be an effective way to produce coal-bed methane, and this method can not only create several high-conductivity hydraulic fractures, but also activate and connect existing natural fractures so as to form large spacious network system (Clarkson, 2013).

Compared with the conventional reservoirs, coal-bed methane reservoir has its unique characteristics, such as adsorption, desorption, diffusion and so on, its seepage mechanism is different from conventional gas reservoirs. As is known to all, to release the adsorbed gas from the coal surface and to produce it through the natural cleat system, the reservoir pressure should be reduced to a critical desorption pressure by dewatering operation. Dewatering stage, desorption-diffusion stage and seepage stage are the three important stages which are taking place during the process of CBM production. Generally speaking, the intermediate-time and late-time are the main steady-state production stage of coal-bed methane, during which a large amount of gas and a small amount of water are produced, therefore, it is of significance to study this production principle of this stage. At present, the studies on coal-bed methane production capacity mostly apply to numerical simulation method (Ou Chenghua, 2011), the analytical solution is barely existing. Because of the existence of adsorption and diffusion, productivity prediction models (Ning Zhengfu, 2002, Lang Zhaoxin, 1994, Hujun, 1996, Xu Yanbo, 2006, Fu Yu, 2003) for conventional reservoirs are not suitable to coal-bed methane reservoir.

To sum up, the productivity analysis model of coal-bed methane at the steady -state production stage has not yet emerged. In this paper, steady-state production

stage is assumed to be approximate single-phase gas flow, however, it will lead to severe errors if conventional binomial equations (without considering gas adsorption and diffusion) are applied to analyze steady-state production of coal-bed methane. Therefore, in terms of natural fractured coal-bed reservoirs, this paper firstly establishes steady-state productivity model applied parallel-plate theory, equivalent seepage resistance principle and equivalent continuous medium principle. Based on this new productivity model, the inflow performance relationship (IPR) curves are plotted and the analysis of model simplification is conducted. Finally, this new model is approved to have great accuracy compared with a real production data.

Model Establishment

The schematic illustration in Fig.1A depicts a typical ideal natural fractured coal-bed methane reservoir model (Warren and Root, 1963), which consist of matrix block and cleat (fractures). Using parallel plate theory, one of arbitrary characteristic unit cube (seen from Fig.1B) is selected to analyze the flow mechanism, and its length, width and height respectively is equal to a, b and h. As well all know, the flow mechanism in this characteristic unit cube can represent that of the whole coal-bed methane reservoir. In the unit the width of the vertical fractures is equal to bf, vertical fracture is assumed to be penetrated fully throughout the unit, the line density of fractures is equal to df, the width remained matrix is equal to bm. Under steady-state conditions, the analysis of pressure and rate of characteristic unit is conducted with equivalent seepage resistance principle. Assuming that fracture permeability, matrix permeability and gas diffusion coefficient are anisotropy, therefore, we should analyze the seepage principle from the three orthogonal directions.
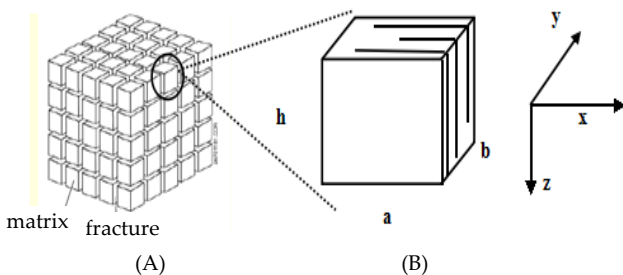

matrix fracture

(A)   (B)

FIG.1 (A) IDEAL MODEL OF FRACTURED COAL-BED METHANE, (B) CHARACTERISTIC UNIT OF FRACTURED COAL-BED METHANE

Note: the following parameters all apply for Darcy unit.

Equivalent Permeability at x-direction

Seen from Fig.2, the flow directions in fractures and matrix are all paralleled to the x direction. We can observe the flow process via magnifying part of the unit. The red spots represent the gas in fracture, and the blue spots represent the gas in matrix. It is apparent observed that the matrix and fracture are parallel. Based on the equivalent seepage resistance principle, the total production rate in this unit consists of two parts: rate in matrix and rate in fractures. The total rate can be presented as follow:

$$Q_t = Q_f + Q_m \tag{1}$$

where, the production rate in fracture can be presented base on Darcy'slaw:

$$Q_f = \frac{T_{sc} k_{fx} d_f b b_f h}{2 T p_{sc}} \frac{\Delta \varphi}{a} \tag{2}$$

Desorption and diffusion are the main flow regimes in matrix pore media. Under the steady-state condition, the total amount of desorption rate and inter-porosity rate is equal to the production output from the matrix. Using the Fick's law of diffusion and Darcy's law, the diffusion rate and inter-porosity rate can be respectively presented as:

$$Q_d = b_m h D_x \frac{\Delta C}{a} \tag{3}$$

$$Q_c = 6 \frac{T_{sc} k_{mx}}{T p_{sc}} b_m h \frac{\Delta \varphi}{a} \tag{4}$$

Combining Eq.(3) and Eq.(4), the total production rate of matrix is as follows:

$$Q_m = b_m h D_x \frac{\Delta C}{a} + 6 \frac{T_{sc} k_{mx}}{T p_{sc}} b_m h \frac{\Delta \varphi}{a} \tag{5}$$

We assume that the diffusion rate is equal to the adsorption rate under this steady-state condition. Thus, according to the Langmuir isothermal adsorption equation, one can obtain:

$$\frac{\Delta C}{a} = (1 - \phi_f - \phi_m) V_L \frac{\varphi_L}{(\varphi_L + \varphi)^2} \frac{\Delta \varphi}{a} \tag{6}$$

Submitting Eqs.(6) into Eq.(5), we can obtain the following equation:

$$Q_m = b_m h D_x (1 - \phi_f - \phi_m) V_L \frac{\varphi_L}{(\varphi_L + \varphi)^2} \frac{\Delta \varphi}{a} + 6 \frac{T_{sc} k_{mx}}{T_{sc} p_{sc}} b_m h \frac{\Delta \varphi}{a} \tag{7}$$

The x-direction equivalent permeability, kx is introduced in this paper. Applied to the equivalent seepage resistance principle, the kx can be presented

as follow:

$$\frac{T_{sc}k_x bh}{2Tp_{sc}}\frac{\Delta\phi}{a}=b_m h D_x(1-\varphi_f-\varphi_m)V_L\frac{\phi_L}{(\phi_L+\phi)^2}\frac{\Delta\phi}{a}+\frac{T_{sc}k_{fx}D_f bb_f h}{2Tp_{sc}}\frac{\Delta\phi}{a}$$
$$+6\frac{T_{sc}k_{mx}}{T_{sc}p_{sc}}b_m h\frac{\Delta\phi}{a}$$

(8)

Furthermore, Eq.(8) can be simplified as the following formation:

$$k_x=\frac{2Tp_{sc}}{T_{sc}}\frac{b_m}{b}D_x(1-\phi_f-\phi_m)V_L\frac{\varphi_L}{(\varphi_L+\varphi)^2}+k_{fx}D_f b_f+12k_{mx}\frac{b_m}{b}$$ (9)

An adsorption-diffusion relevant permeability at x direction can be defined as the following formation:

$$k_d=\frac{2Tp_{sc}}{T_{sc}}D_x(1-\phi_f-\phi_m)V_L\frac{\varphi_L}{(\varphi_L+\varphi)^2}$$

(10)

Therefore:

$$k_x=k_d+12k_{mx}+(k_{fx}-k_d-12k_{mx})D_f b_f$$ (11)

Based on the definition of porosity, one can obtain:

$$\phi_f=\frac{bD_f b_f ha}{hab}=D_f b_f$$

(12)

Finally, the final formation of x-direction equivalent permeability is presented as:

$$k_x=k_d+12k_{mx}+(k_{fx}-k_d-12k_{mx})\phi_f$$ (13)
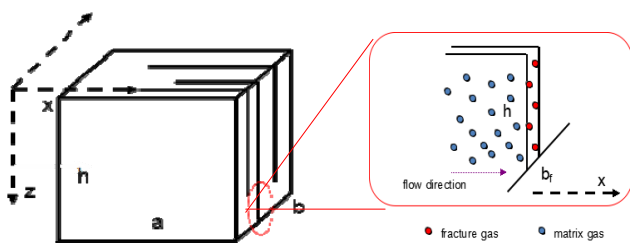
FIG. 2 THE IDEAL ILLUSTRATION OF GAS FLOW AT X-COORDINATION DIRECTION

Equivalent Permeability at z-direction

Seen from Fig.3, the flow directions in fractures and matrix are all paralleled to the z direction. We can observe the flow process via magnifying part of the unit. Similarly, the red spots represent the gas in fracture, and the blue spots represent the gas in matrix. It is apparently observed that the matrix and fracture are parallel. Based on the equivalent seepage resistance principle, the total production rate in this unit consists of two parts: rate in matrix and rate in fractures. The z-direction equivalent permeability can be presented as follows:

$$k_z=k_d+12k_{mz}+(k_{fz}-k_d-12k_{mz})\phi_f$$ (14)

where:

$$k_d=\frac{2Tp_{sc}}{T_{sc}}D_z(1-\phi_f-\phi_m)V_L\frac{\varphi_L}{(\varphi_L+\varphi)^2}$$ (15)
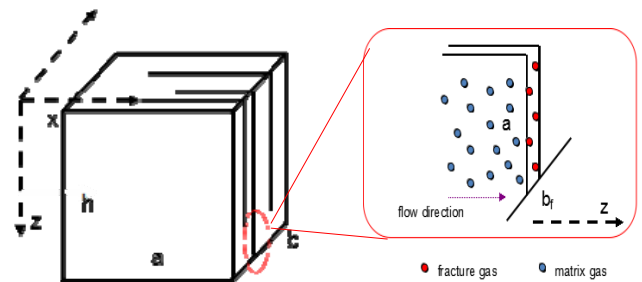

FIG. 3 THE IDEAL ILLUSTRATION OF GAS FLOW AT Z-COORDINATION DIRECTION

Seen from Fig.4, the flow directions in fractures and matrix are in series connection at the y direction. We can observe the flow process via magnifying part of the unit. Similarly, the red spots represent the gas in fracture, and the blue spots represent the gas in matrix. It is apparently observed that the matrix and fracture are in series connection. Based on the equivalent seepage resistance principle, the total pressure drop in this unit consists of two parts: pressure drop in matrix and pressure drop in fractures. The total pressure drop can be presented as follows:

$$\Delta p=\Delta p_f+\Delta p_m$$ (16)

Inside the matrix, the directions of diffusion and inter-porosity are parallel to each other. Similar with the Eqs.(7), the total rate of matrix can be presented using equivalent seepage resistance principle:

$$Q=ahD_y(1-\phi_f-\phi_m)V_L\frac{\varphi_L}{(\varphi_L+\varphi)^2}\frac{\Delta\varphi}{b_m}+6\frac{T_{sc}k_{my}}{Tp_{sc}}ah\frac{\Delta\varphi}{b_m}$$ (17)

Combining with the matrix and fractures, one can get the y-direction equivalent permeability:

$$\frac{2QTp_{sc}b}{T_{sc}k_y ah}=\frac{2QTp_{sc}D_f bb_f}{T_{sc}k_{fy}ah}+\frac{Qb_m}{ahD_y(1-\phi_f-\phi_m)V_L\frac{\varphi_L}{(\varphi_L+\varphi)^2}+6\frac{T_{sc}k_{my}}{Tp_{sc}}ah}$$ (18)

And then,

$$k_y=\frac{k_{fy}(k_d+12k_{my})}{k_{fy}+(k_d+12k_{my}-k_{fy})\phi_f}$$ (19)

Where:

$$k_d=\frac{2Tp_{sc}}{T_{sc}}D_y(1-\phi_f-\phi_m)V_L\frac{\varphi_L}{(\varphi_L+\varphi)^2}$$ (20)

Eq.(11), (12), (17)respectively represents the equivalent permeability at three different directions under steady-state condition. As the matter of fact, the actual

natural fractured coal-bed methane is made up of this countless characteristic units. Therefore, the flow mechanism of this unit can represent the whole coal-bed methane reservoir. It is also found that this new model can convert the dual-porosity reservoir into a homogeneous reservoir.
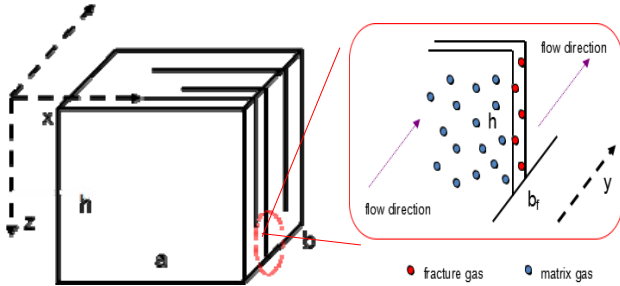

FIG. 4 THE IDEAL ILLUSTRATION OF GAS FLOW AT Y-COORDINATION DIRECTION

Analysis of Model Simplification

This paper establishes an equivalent continuum media model of fractured coal-bed methane reservoirs under steady-state condition. The anisotropic diffusion coefficient and permeability are considered as well. As a result, the equivalent permeability of the three orthogonal directions is solved. It is also found that the model can be simplified to different media types and reservoir conditions, as follows:

When $V_L=0$, the term of diffusion is eliminated, this new model can simplified as the conventional dual-porosity reservoir ignoring the diffusion and adsorption. Therefore, based on Eqs.(11), (12), (17), the equivalent permeability of three directions can be presented as follows:

$$k_x = 12k_{mx} + (k_{fx} - 12k_{mx})\phi_f \tag{21}$$

$$k_y = \frac{12\,k_{fy}\,k_{my}}{k_{fy} + (12\,k_{my} - k_{fy})\phi_f} \tag{22}$$

$$k_z = 12k_{mz} + (k_{fz} - 12k_{mz})\phi_f \tag{23}$$

Where:

$$k_d = \frac{2Tp_{sc}}{T_{sc}} D_i (1-\phi_f-\phi_m) V_L \frac{\varphi_L}{(\varphi_L+\varphi)^2}, (i=x,y,z) \tag{24}$$

When $k_m=0$, the term of inter-porosity is eliminated, this new model can simplified as dual-porosity coal-bed methane reservoir with consideration of the diffusion and adsorption and without consideration of viscous flow in matrix. Therefore, the equivalent permeability of three directions can be presented as follows:

$$k_x = k_d + (k_{fx} - k_d)\phi_f \tag{25}$$

$$k_y = \frac{k_{fy}\,k_d}{k_{fy} + (k_d - k_{fy})\phi_f} \tag{26}$$

$$k_z = k_d + (k_{fz} - k_d)\phi_f \tag{27}$$

When $k_m=0$, $V_L=0$ and $\Phi_m=0$, the terms of inter-porosity and diffusion are simultaneously eliminated, this new model can be simplified as a conventional homogeneous reservoir.

The Analysis of IPR Curves

The schematic illustration in Fig.5 shows a fully penetrating multi-stage fracturing horizontal well of infinite-acting coal-bed methane reservoir. The horizontal well is intercepted by some finite-conductivity hydraulic fractures. The number of hydraulic fractures is N, the length and width of the ith (i=1, 2, 3, ..., N) fracture respectively is equal to L_{Fi} and W, the formation thickness is H. The permeability of hydraulic fracture is k_F, and those fractures distributed evenly along to the horizontal well. To begin with, the reservoir fluid flow from formation into hydraulic fractures, and then flow from fracture into wellbore. Therefore, the total rate of the well is equal to sum of all fractures.
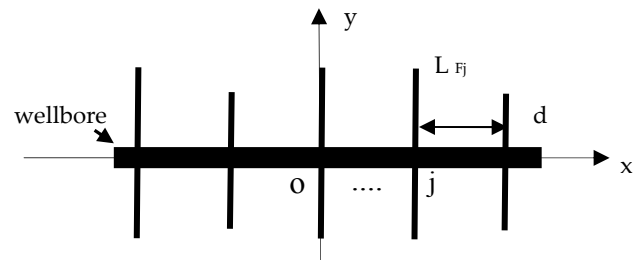

FIG. 5 THE ILLUSTRATION OF MULTI-STAGE HORIZONTAL WELL IN COAL-BED METHANE RESERVOIR

Appling parallel-plate theory, equivalent seepage resistance principle and equivalent continuous medium principle, the fractured dual-porosity coal-bed methane reservoir is equivalent to a homogeneous reservoir, the equivalent permeability can represent the characters of diffusion and adsorption. Based on the Darcy's law, the governing equation can be obtained as follow:

$$\frac{1}{r}\frac{d(r\frac{p}{\mu z}k(p)dp)}{dr} = 0 \tag{28}$$

A new pseudo-pressure is defined by the following formation:

$$\zeta = \int_{p_o}^{p} \frac{2k(p)p}{\mu z} dp \qquad (29)$$

Submitting Eq.(20) into Eq.(28), a new pressure can be obtained:

$$\varsigma = \frac{q_{sc}Tp_{sc}}{\pi h T_{sc}} \ln r + C \qquad (30)$$

According to the superposition principle, the pressure of the ith fracture can be presented as the formation:

$$\varsigma_{fi}(id,0) = \frac{Tp_{sc}}{\pi h T_{sc}} \sum_{j=1}^{N} q_{scj} arcch \sqrt{1+(\frac{id-jd}{L_{Fj}})^2} + C \qquad (31)$$

We assume that the radius of outer boundary is Re, the pressure at this position can be described as:

$$\varsigma_{ei}(R_e,0) = \frac{Tp_{sc}}{\pi h T_{sc}} \sum_{j=1}^{N} q_{scj} arcch \sqrt{1+(\frac{R_e-jd}{L_{Fj}})^2} + C \qquad (32)$$

Combing with Eq.(31) and Eq.(32):

$$\varsigma_e(R_e,0) - \varsigma_{fi}(id,0) = \frac{Tp_{sc}}{\pi h T_{sc}} \sum_{j=1}^{N} q_{scj}[arcch \sqrt{1+(\frac{R_e-jd}{L_{Fj}})^2}$$
$$-arcch \sqrt{1+(\frac{id-jd}{L_{Fj}})^2}] \qquad (32)$$

A half length of hydraulic fracture is far smaller than radius of wellbore, the flow pattern in the hydraulic fracture can be regarded as a radial flow. The thickness is W, the outer radius is H/2, the pseudo-pressure of outer boundary is ζ_{fi}, the pseudo-pressure of inner boundary is ζ_{wfi}.

$$\varsigma_{fi} - \varsigma_{wfi} = \frac{q_{sc}Tp_{sc}}{\pi w T_{sc}} (\ln \frac{H}{2r_w} + S) \qquad (33)$$

Thus, the pressure drop between reservoir and borehole can be presented with combing Eq.(33) and Eq.(34):

$$\varsigma_e(R_e,0) - \varsigma_{wfi}(id,0) = \frac{Tp_{sc}}{\pi h T_{sc}} \sum_{j=1}^{N} q_{scj}[arcch \sqrt{1+(\frac{R_e-jd}{L_{Fj}})^2}$$
$$-arcch \sqrt{1+(\frac{id-jd}{L_{Fj}})^2}] + \frac{q_{sci}Tp_{sc}}{\pi w T_{sc}} \ln \frac{h}{2r_w} \qquad (34)$$

Considering the wellbore infinite-conductivity, the pressure of every fracture is equivalent. Therefore, Eq.(35) can be rewritten as the following formation:

$$\varsigma_e - \varsigma_{wf} = \frac{Tp_{sc}}{\pi h T_{sc}} \sum_{j=1}^{N} q_{scj} \ln \frac{\sqrt{1+(\frac{R_e-jd}{L_{Fj}})^2} + \frac{R_e-jd}{L_{Fj}}}{\sqrt{1+(\frac{id-jd}{L_{Fj}})^2} + |\frac{id-jd}{L_{Fj}}|}$$
$$+ \frac{q_{sci}Tp_{sc}}{\pi w T_{sc}} \ln \frac{h}{2r_w} \qquad (35)$$

By rewriting Eq.(36) for all hydraulic fractures , we can get N equations with N unknowns parameters which are q_{sci}. Composing a N-order system linear algebraic equations. We assume that the well produces at the constant production in the flow pressure condition, thus, the total production rate of the well is the sum of all hydraulic fractures:

$$q_{sc} = \sum_{i=1}^{N} q_{sci}, (i=1,2,3...N) \qquad (36)$$

The Effects of Adsorption

Langmuir pressure and Langmuir volume are the characteristic parameters of adsorption, Selecting the basic parameters: kf = 0.1mD, Φ_m = 0.08, Φ_f = 0.001, D = 1.0cm^2/s, Pi = 10Mpa, N =3 , re=500m, h=10m, rw=0.1m, L$_F$=50m. Seen from Fig.6, the IPR curves are plotted with different Langmuir pressure P$_L$ (1.5Mpa, 2Mpa, 2.5Mpa) and Langmuir volume V$_L$ (20sm^3/m^3, 25sm^3/m^3, 30sm^3/m^3).
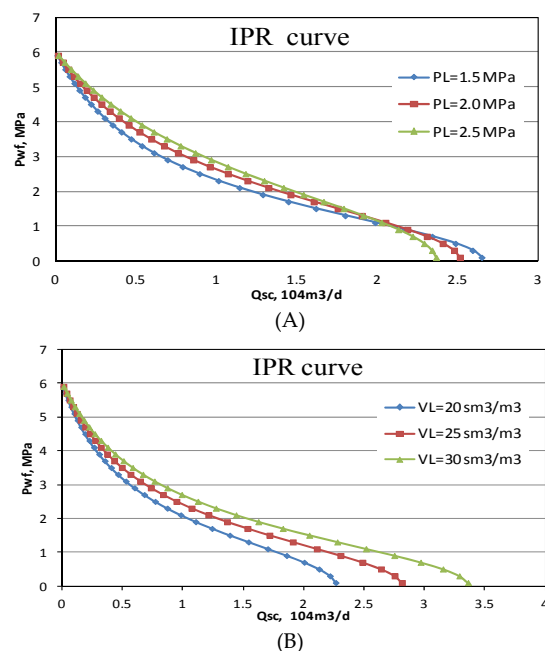

(A)

(B)

FIG. 6 THE ILLUSTRATION OF THE EFFECTS OF LANGMUIR PARAMETERS ON IPR CURVES: (A) LANGMUIR PRESSURE; (B) LANGMUIR VOLUME

Considering the impact of desorption in coal-bed methane, the shape of the IPR curves of coal-bed methane is greatly different from the conventional gas reservoir. Showing the shape of "dip", and with the increment of Langmuir pressure, IPR curve of coal-bed methane gradually transforms to conventional IPR curve, while the absolute open-flow rate decreased. From the analysis of its micro-mechanisms, the desorption does not occur when the formation pressure is bigger than the Langmuir pressure, and

then the flow characteristics of coal-bed methane are similar to the conventional gas reservoir. On the contrary, when the formation pressure is lower than Langmuir pressure, the gas desorption occurs, the bigger the value of Langmuir pressure, the earlier the desorption occurs, as a result, the more the production rate under the same production pressure drops (seen from fig.6(A)).

Similarly, the desorption does not occur when the formation pressure is bigger than the Langmuir pressure, as a result, the IPR curves are Coinciding although the Langmuir volume of each curve is different. When the formation pressure is lower than Langmuir pressure, the gas desorption occurs, and the larger the value of Langmuir volume, the bigger the total sum of adsorption gas, as a result, the more the production rate under the same production pressure drops. What's more, the absolute open-flow rate also increases with the increment of Langmuir volume. (seen from fig.6(B))

The Effects of Diffusion

This paper assumes that the diffusion pattern in matrix is steady-state diffusion and the diffusion coefficient D is the characteristic parameter of diffusion. Selecting the basic parameters: k_f = 0.1mD, k_m = 0.001mD, Φ_m = 0.08, Φ_f = 0.001, P_i = 10Mpa, P_L = 5Mpa, V_L = 3m³/m³, N = 3, rw=0.1m, L_F=50m.The IPR curves are plotted with different diffusion coefficient, D = 0.5cm²/s, 0.8cm²/s, 1cm²/s. (seen from Fig.7).
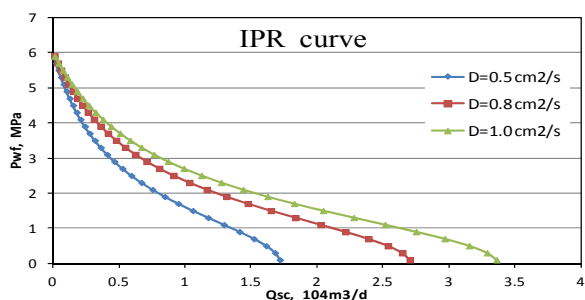

FIG. 7 THE ILLUSTRATION OF THE EFFECTS OF DIFFUSION COEFFICIENT ON IPR CURVES

Seen from Fig. 7, the smaller the value of diffusion coefficient, the deeper the shape "dip", and the smaller the absolute open-flow rate. From the analysis of the micro-mechanism, the diffusion coefficient represents the ability of gas diffusion in matrix, the less apparent the term of diffusion, the more apparent the term of seepage in fractures. As a result, the feature of IPR curves is more similar to the conventional gas reservoir. Generally speaking, the bigger the value of

diffusion coefficient, the stronger the ability of flowing, and the more the amount of absolute open-flow rate.

The Analysis of the Model Simplification

The new model proposed by this paper is simplified as the following situations: V_L = 0, D = 0, namely, the fractured dual-porosity conventional reservoir without consideration of adsorption and diffusion; km=0, namely, fractured dual-porosity coal-bed methane reservoir with consideration of diffusion in matrix, the inter-porosity is ignored; k_m = 0, V_L = 0 and Φ_m = 0, namely, the terms of diffusion, and inter-porosity in matrix are ignored, the new model is simplified as the basic model conventional homogeneous reservoirs. In terms of the above situations, the relevant IPR curves are respectively plotted (seen from Fig. 8).

Seen from Fig.5, curveⅠand curve Ⅲ is the very IPR curves without consideration of desorption, it is apparently shows that the character of the two IPR curves is similar to the conventional gas reservoirs. By comparing the two curves, the production rate with consideration of inter-porosity in matrix is more than that without consideration of inter-porosity in matrix. Curve Ⅱ is the very IPR curve with consideration of diffusion and adsorption in matrix, while the inter-porosity is ignored. We can find that the shape of curve Ⅱ is like "dip", and is greatly different from conventional gas reservoirs (such as curveⅠand curveⅢ), besides, the absolute open-flow rate is higher than conventional gas reservoirs. Curve Ⅳ represents the new model proposed in this paper, the productivity capacity decrease when we take the desorption, diffusion and inter-porosity flow into account, and absolute open-flow rate reaches the maximum.
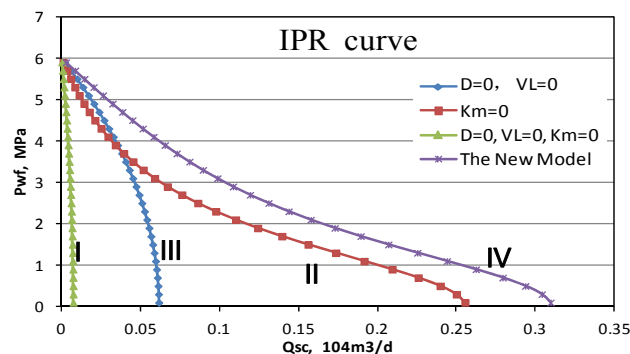

FIG. 8 THE ILLUSTRATION OF DIFFERENT IPR CURVES WITH MODEL SIMPLIFICATION

Case analysis

A certain coal-bed methane reservoir, Shanxi Province in China. The basic property parameters are as follows: k_f=0.124mD,k_m=0.0012mD,Φ_m=0.052,Φ_f=0.001,D=1.5cm^2/s,Pi=9.8Mpa,h=10.7m,Re=1500m,L=800m, the average Langmuir pressure P_L=2Mpa, VL=25.3m^3/m^3, N=10. Based on the date of real production pressure data and real production rate data, it is found that the steady flow pressure is approximate equal to 2.5 MPa and the corresponding rate is approximate equal to 15000 m^3/d. Seen from the Fig.9, the IPR curve is plotted using the above parameters and the new model, the theoretical production is approximate 17000m3/d. Therefore, the relative error is 11.6%. In conclusion, this new model has certain practical value.
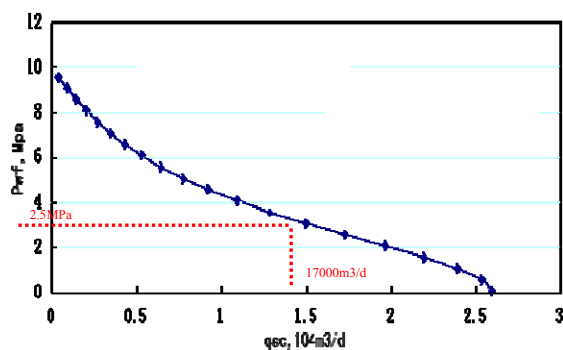
FIG.9 THE ILLUSTRATION OF DIFFERENT IPR CURVES WITH MODEL SIMPLIFICATION

Conclusions

In terms of natural fractured coal-bed reservoirs, this paper initially establishes steady-state productivity analysis model with parallel-plate theory, equivalent seepage resistance principle and equivalent continuous medium principle, and the unique characters of diffusion, adsorption of coal-bed methane are considered as well.

Considering the impact of desorption and diffusion of coal-bed methane, the IPR curves are different from that conventional gas reservoirs, the smaller the Langmuir volume, the deeper the curves concave and the smaller the absolute open-flow rate. The smaller the Langmuir pressure, the more serious the curves concave, however, the bigger the absolute open-flow rate.

This new model can have certain representativeness, it can be easily simplified as various familiar models. What's more, compared with the real field case, the accuracy is moderate and has certain practical value. Generally speaking, although the numerical simulation method is applied to predict the production rate of coal-bed methane, this new model is far easier and also can save much time compared with the numerical simulation method, it also can meet certain accuracy requirement.

REFERENCES

Clarkson, C.R, 2013. Production data analysis of unconventional gas wells: Review of the theory and best practices. Int. J, Coal Geoal.109-110,101-149.

Fu Yu, Guo Xiao, Long Hua. Productivity method of fractured horizontal wells in coal-bed gas[J].Journal of the Southwest university of petroleum.2003,25(3):44-46.

Gas Research Institute. A guide to coalbed methane reservoir engineering. GRI reference No. GRI-94/0397, Chicago, Illinois; 1994.

Hamm S Y, Bidaux P. Dual-Porosity Fractal Models for Transient Flow Analysis in Fissured Rocks[J]. Water Resources Research, 1996, 32(9): 2733-2745.

Hujun Li,et al.A new method to predict performance of fractured horizontal wells[C].SPE37051,1996:179～185.

Kan Yili, Luo Pingya. Discussion of development classification for coal reservoir[J].Journal of the Southwest university of petroleum.2003,25(6):19-22.

Karn FS, Friedel RA, Thames BM, Sharkey AG. Gas transport through sections of solid coal. Fuel 1970; 49(3):249–56.

Kong Qingli. Research of percolation and desorption mechanism in dual-porosity media for coal-bed methane[J]. Northeast university of petroleum.2012.

Lang Zhaoxin et al.Investigation on productivity of fractured horizontal well.Journal of the university of petroleum.1994, 18(2):43-46.

LI Q, WANG W, ZHU C, et al. Analysis of fault water-inrush mechanism based on the principle of water-resistant key strata[J]. Journal of Mining & Safety Engineering, 2009, 1: 020.

Li Song, Tang Dazhen, Xu Hao et al. The analysis of

formation properties for different coal structure[A][J]. Paper Content of coal-bed methane academic discussion. 2011.

Ning Zhengfu, Han Shugang, Chen Lingsong, Li Chunlan.Productivity calculation method of fractured horizontal wells in low permeability oil or gas field.ACTA PETROLEI SINICA.2002,23(2):68-71.

Ou Chenghua, Liang Chenggang, Jiang Jianli, Zhang Juncheng. A stage-by-stage flow model of coal-bed methane gas considering adsorption and deformation[J]. Natural Gas Industry.2011, 31(3):48-51.

Spivey JP, Semmelbeck ME. Forecasting long-term gas production of dewatered coal seams and fractured gas shales. In: SPE 29580, presented at the low permeability reservoirs symposium, Denver, Colorado; March 19–22; 1995.

Van Milligen B P, Bons P D, Carreras B A, et al. On the applicability of Fick's law to diffusion in inhomogeneous systems[J]. European journal of physics, 2005, 26(5): 913.

Warren, J. E, Root, P, J. The Behavior of Naturally Fractured Reservoirs. SPE Journal, 1963, 3(3):245-255.

Wu Shiyue, Guo Yongyi. Research of transport principle for coal-bed methane[J]. 1999, 24(1)65-69.

Wu Xiaomin, Tu Chunze. The determination of basic size and analysis of typical fracture geometry for fractured coal reservoir[J]. Journal of the china university of geology, 1995, 20(1):112-116.

Xu Yanbo, Qi Tao, Yang Fengbo, Li Huaiyin, Zhou Shouxin. New model for productivity test of horizontal well after hydraulic fracturing. ACTA PETROLEI SINICA.2006, 27(1):89-96.

Yang Chaopeng, Gao Shusheng, Liu Guangdao et al.Current situation and tendency of percolation mechanisms for tight sandstone gas reservoir[J]. Technology and Engineering, 2013, 20(32):8606-8613.

Yin Y. Adsorption isotherm on fractally porous materials[J]. Langmuir, 1991, 7(2): 216-217.

Xiao Cong born in 1989, male, Hubei life extension, Mater, the membership of SPE. Studying in China University of Petroleum (Beijing) from the year of 2013. He engaged in oil and gas field development technology and reservoir engineering research.

Mingjin Liu born in 1991, female, Hubei life extension, Master, the membership of SPE. Studying in Southwest University of Petroleum (Chengdu) from the year of 2013 . He engaged in oil and gas field geology development and reservoir engineering research.

Tian Leng born in 1977, male, Heilongjiang life extension, PhD, lecturer. Graduated from China University of Petroleum (Beijing) in 2001 with a doctorate degree in June, 2006. He engaged in oil and gas well testing technology and reservoir engineering teaching and research.

Zhao Chao born in 1990, male, Hubei life extension, Mater, the membership of SPE. Studying in China University of Petroleum (Beijing) from the year of 2013. He engaged in oil and gas field development technology and reservoir engineering research.

Yanchen Wang born in 1990, male, Shandong life extension, Master, the membership of SPE. Studying in Southwest University of Petroleum (Chengdu) from the year of 2013. He engaged in oil and gas field development and reservoir engineering research.

Finite Element Study of the Paleostress and Natural Fracture Development in the Bakken Formation, Nesson Anticline Area, North Dakota

Peng Pei[*1], Zhengwen Zeng[2], Kegang Ling[3]

[1]Institute for Energy Studies, University of North Dakota, USA

243 Centennial Drive, Grand Forks, ND, USA, 58202

[2]Department of Geology and Geological Engineering, University of North Dakota, USA

81 Cornell St., Grand Forks, ND USA, 58202

(Current address: 501 Westlake Park Blvd, Houston, TX, USA, 77079)

[3]Department of Petroleum Engineering, University of North Dakota, USA

243 Centennial Drive, Grand Forks, ND, USA, 58202

[*1]peng.pei@und.edu; [2]zhengwen.zeng@bp.com; [3]kegang.ling@und.edu

Abstract

The Bakken formation is a tight oil play with continuous oil accumulation. Fractures play an important role in both exploration and production of the oil. As considered to be one of the most promising plays in the world, oil production from the Bakken largely depends on presence of natural or artificially-created fractures. There also exist arguments about the oil migration patterns in and out of the Bakken. This paper reviews the tectonic history of the Nesson anticline in the Williston basin, North Dakota, USA, and a numerical model of the study area has been built to reconstruct the paleostress under the far-field effect of the Laramide orogeny in late Cretaceous. The modeling results show that tensile horizontal stress was developed in most parts around the Nesson master fault in the study area during the Laramide event, and tensile fractures are very likely to be generated in the north and south sides of the fault. These tensile fractures could enhance the reservoir quality in both porosity and permeability. Zones of possible fracture development are identified based on the stress profile. In the fault zone, the paleostress has a lower magnitude of compressive stress than that in the host rock, so driving force may be provided to push the oil migrate from the host rock to the fault zone. However, after the hydrocarbon accumulated in the fault, fractures presented around the fault may function as additional pathways for migration again.

Keywords

Bakken Formation; Nesson Anticline; Paleostress; Natural Fractures; Finite Element

Introduction

The late Devonian to early Missippian Bakken formation holds a significant amount of recoverable oil. It is considered as one of the most promising tight oil plays in the world. The Bakken formation, which covers a large area of 200, 000 square miles in parts of Montana, North Dakota, Saskatchewan and Manitoba, is one of many hydrocarbon producing formations in the Williston basin (Vincent 2011).

The Williston basin is a roughly oval-shaped, subsurface sedimentary basion. With the deepest location in its center, the strata becomes shallower and thinner towards its margins (Ling et al. 2014). Major structural features in the North Dakota portion include the Nesson anticline, Little Knife anticline, Billings anticline, and part of the Cedar Creek anticline (Figure 1).

First described and named in 1953, the Bakken had not become an actively producing play until recent years (Nordeng 2010). The estimated original oil in place (OOIP) in the Bakken appeared on literature ranges from billions of barrels to hundreds of billions of barrels (LeFever et al. 1991; Pitman et al. 2001; Flannery and Kraus 2006; Nordeng 2009; Clark 2009; Pilcher et al. 2011). However, the recovery factor of Bakken formation is very low. In most areas, recovery factor is less than 5%, or even less than 1%; in a few

areas, the recovery factors might range as high as 5% to possibly 15%. Historic value of recovery factor listed on the website of North Dakota Industry Commission (NDIC) ranges from 1% to 19% (Clark 2009). With the successful application of horizontal drilling and hydraulic fracturing, coupled with the high oil price, oil production from the Bakken has increased rapidly, from 100,000 barrel per day in 2007 to over 1,000,000 barrels per day in 2014 (U.S. Energy Information Administration, 2014). It is predicted that the production will reach 800,000 barrels per day during 2016-2018 (Stark 2011).
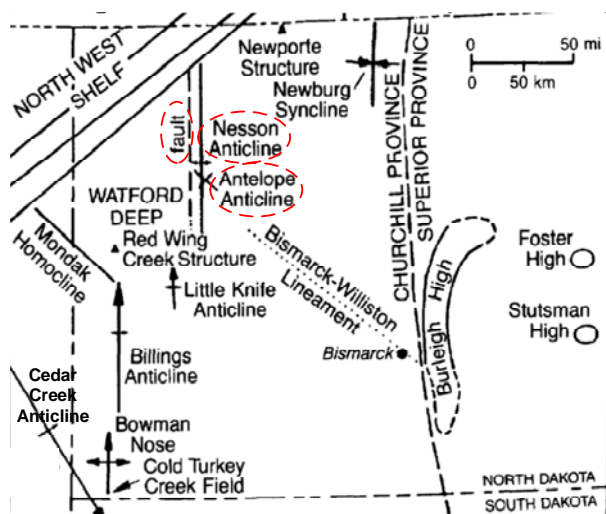
Fig. 1 MAJOR STRUCTURAL FEATURES OF THE WILLISTON BASIN, NORTH DAKOTA PORTION (AFTER GERHARD ET AL. 1991)

The Bakken formation is a wide and relatively thin unit. Petroleum accumulations cover large areas, with poorly defined margins (Pei et al. 2014). As a continuous oil accumulation with an unconventional development model, natural fractures significantly enhance the reservoir quality of such a tight formation, forming the "sweetspots". Production with economic success usually depends on the presence of natural or artificially-created fractures (Nordeng 2009; Pilcher et al. 2011; He et al. 2013; Wang et al. 2013). Bakken has geology that is very conducive to horizontal drilling and hydraulic fracturing (Tertzakian, 2012). Most of the current production activities focus on the Middle Bakken member. In North Dakota, this Middle member typically consists of gray interbedded siltstones and sandstones. At depths of 9,500 to 11,000 feet (ft), thickness of the Middle member can reach about 80 ft (Vincent 2011). Along the Nesson anticline is the most intensively drilled, and most profitable produced area of the Bakken formation in the Williston basin. The Bakken formation reaches its maximum thickness, with greatest amount of mature

petroleum in this area. The Nesson anticline is a drag-fold deformation and was created by the activation of the Nesson master fault through the Paleozoic, especially a movement during late Cretaceous as a response to the Laramide orogeny. It is also thought that, at the same time, the Bakken was buried to its maximum depth within the oil window.

We think that there are two reasons why it is difficult to estimate the reserves in the Bakken formation and why the estimated figures are so varying according to different literature: the fact that high productive spotty areas distributed in a large region, and controversy among researchers about the hydrocarbon migration and accumulation patterns from the Bakken source rock. To assist better estimate the reserve and provide support to production plan, it is of importance to understand the distribution of the natural fractures, the paleostress and current in situ stress profiles in the Bakken formation.

This paper presents a finite element study which reconstructs the paleostress profile of the Nesson anticline area during the Laramide event. Based on the simulated paleostress, possibility of development of natural fractures and hydrocarbon migration patterns are discussed.

Geological Background of the Nesson Anticline Area

Geological and Structure Settings

The Nesson anticline is a north-trending structural feature located near the center of the Williston basin. Beneath the west side of the anticline crest there is a major normal fault, which is referred to as the Nesson master fault (Lindsay et al. 1988; Gerhard et al. 1991). The anticline is about 175 km long, with nearly continuous distribution of oil production wells along a north-south line from just south of Canadian border to the Killdeer Mountains, south of the Missouri River. The Nesson master fault bounds the structure from the Beaver Lodge Field to 70 km in the south, with its west side downthrown (Lindsay et al. 1988).

The Nesson anticline has a large bifurcation on its southeast side – the Antelope anticline (Figures 1 and 2). The Antelope anticline trends NW-SE, with a much smaller size comparing to the Nesson anticline. A fault occurs along the northeast side of the Antelope anticline, with its northeast side downthrown. In this paper, the authors refer to this fault as the Antelope fault. The Antelope fault is thought to have affected Devonian and younger strata (Lindsay et al. 1988).
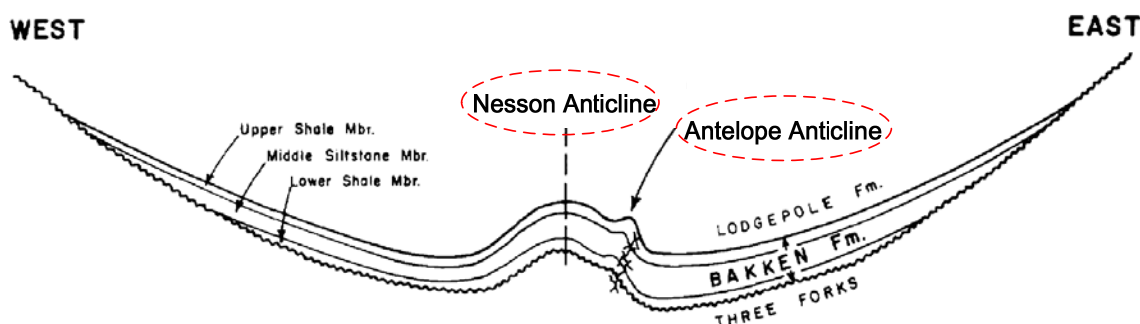
FIG. 2 SCHEMATIC CROSS-SECTION OF THE NESSON ANTICLINE AND ANTELOPE ANTICLINE (AFTER MESSNER 1978)

Presence of the Nesson master fault and the Antelope fault can influence the local in situ stress field. Both the magnitude and the direction of the in situ stress in the fault zone differ from those in the host rock (Gudmundsson et al. 2010). The Nesson anticline area has the most intensive oil production in the Williston basin. Horizontal drilling and hydraulic fracturing are extensively applied in this area. It is of great interest to understand the distribution of the natural fractures and the in situ stress in this region.

The characteristics of the natural fractures, especially origination mechanisms, in the Bakken formation have been investigated by many researchers (Murray 1968; Meissner 1978; Druyff 1991; Pitman et al. 2001; Stockton 2009; Mullen et al. 2010; Warner 2011). As early as 1968, Murray applied the curvature method to study the fracture development in the Devonian Sanish pool in the Antelope field, and the contribution of the natural fractures to reservoir quality. In general, natural fractures in the Bakken formation can be categorized into three types according to different origination mechanisms: 1) fractures caused by structural tectonics; 2) fractures as a result of regional stress; and 3) fractures associated with super-lithostatic pressure increase due to the hydrocarbon expulsion during maturation.

The Bakken is also regionally overpressured and featured with a very high pore pressure. Documented fluid-pressure gradient is as high as 0.73psi/ft in the Antelope filed. These high pressures are discretely confined to the Bakken interval (Meissner 1978) and are beneficial for oil production.

We consider that there are several reasons why the Nesson anticline area has appeared to be the highest producing area in the basin: 1) the Bakken reaches its maximum thickness along the Nesson anticline, so it contains the largest amount of hydrocarbon in this area; 2) the greatest volume of oil was generated in the Bakken shale in the area around the Nesson anticline

(Flannery and Kraus 2006); 3) natural fractures are probably more developed in this area, therefore the reservoir quality is enhanced; and 4) paleostress difference probably had driven mature hydrocarbon from nearby areas into the fault zone. The last reason is delivered from the modeling results which will be presented in next parts in this paper.

Tectonic History of The Nesson Anticline

Different explanations have been proposed about the tectonic history of anticlines in the Williston basin. Redly and Hajnal (1995) proposed that these foldings were formed as a result of the subsidence of the basin. They considered that subsidence of a circular segment of a spherical surface, such as the Williston basin, gave rise to two types of folding: circular folding at the dynamic rim, and radial folding at the central part. According to their description, the Cedar Creek anticline, with a proven ENE dipping (basin center direction) western boundary fault, was an example of circular folding. The Nesson anticline, which is toward to the center of the basin, is a radial folding.

However, most of other studies consider that the fold structures in the basin are the result of deep basement-linked normal faults reactivated several times during the Paleozoic. We tend to agree with this explanation and follow this explanation in the modeling process presented in this paper. The tectonic history of the Nesson anticline is given as following.

The Nesson anticline was created by a drag fold and its deformation was controlled mainly by the vertical movement along the normal Nesson master fault beneath the west side of the anticline crest (Figure 1). This fault system has been present and active since Precambrian time. The Nesson anticline underwent periodic deformations through the history of the Williston basin. The most recent and strongest reactivation of the fault occurred in response to the Laramide orogeny during late Cretaceous (Thomas

1974; Meissner 1978; Brown and Brown 1987; Gerhard et al. 1987; Lindsay et al. 1988; Gerhard et al. 1991; Warner 2011). This event is considered to have largely resulted in the current structure of the anticline, and the tectonic stress may have induced natural fractures. The detailed stress model used to explain the behavior of the fault and consequent deformation is described as below.

In the Williston basin, a series of basement-weakness zone, represented as lineament at the surface, trend northeasterly and northwesterly. These weakness zones define a framework of basement blocks. These basement blocks and bounding weakness zones appear to have influenced the development of structural features in the basin. The Nesson fault is located in the Weldon basement which trends northeasterly (Figure 3). In late Cretaceous, the Laramide orogeny provided regional compressive

stresses from the southwest, and the response of the basement blocks to the Laramide teconism can be analyzed by analogy to a hypothesized cardboard model (Figure 4). According to the simple shear model proposed by Thomas (1974) and the wrench-style deformation model proposed by Brown (1978), the regional stress regime created the dominant left-lateral adjustment on the northwesterly trending blocks, and the subordinate right-lateral adjustment on the northeasterly trending blocks. Therefore, the Weldon block, where the Nesson anticline was set, subjected to a right-lateral adjustment and experienced right-lateral stress and tensile stress during the Laramide event (Figure 4). This stress profile in the block rejuvenated the vertical displacement along the Nesson master fault (Figure 5). Gerhard et al. (1987) described that during the event, the master fault had a down-to-the-west displacement of about 120 meters (m), or 400 ft,
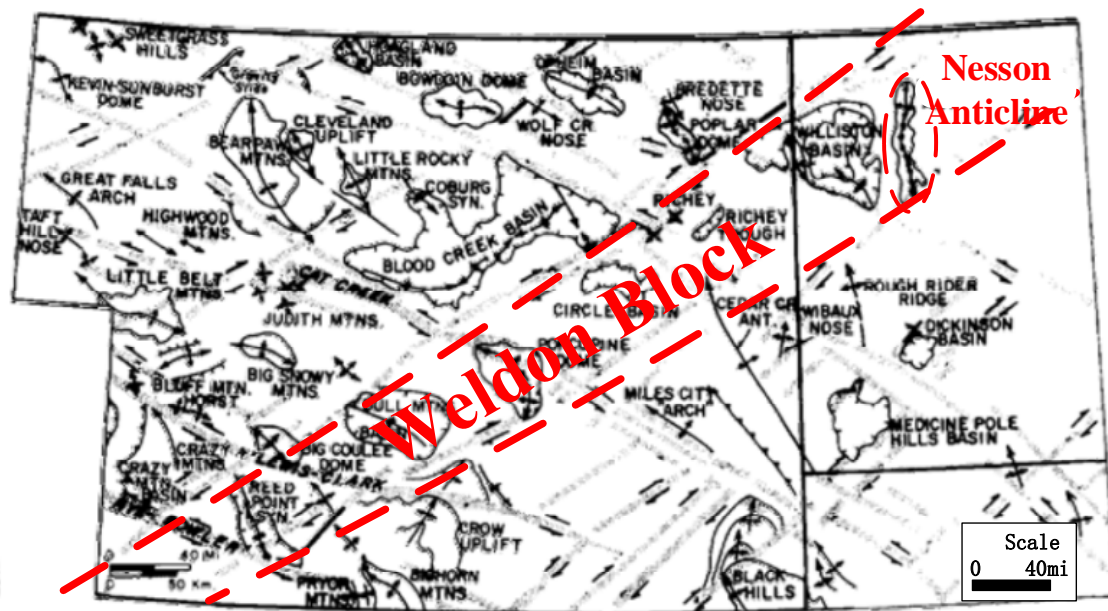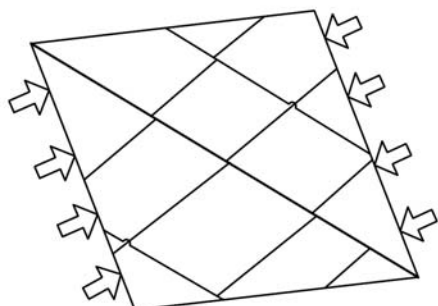

FIG. 3 BASEMENT BLOCKS OF THE WILLISON-BLOOD CREEK BASIN (AFTER THOMAS 1974; WARNER, 2011)
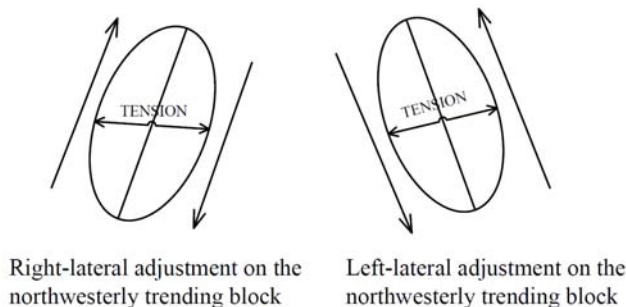

FIG. 4 REGIONAL STRESS APPLIED ON THE BASEMENT BLOCKS DURING THE LARAMID OROGENY, AND RESPONSE OF THE NORTHEASTERLY TRENDING BLOCKS AND NORTHWESTERLY TRENDING BLOCKS, ACCORDING TO THE SIMPLE SHEAR MODEL (AFTER THOMAS, 1974)
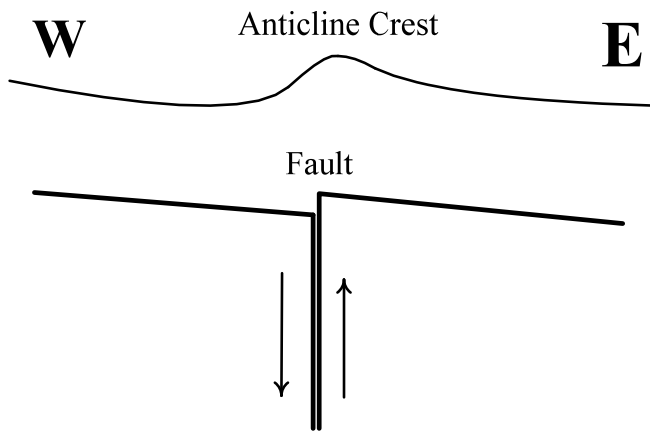
FIG. 5 THE LARAMIDE OROGENY TECTONISM REJUVENATED THE VERTICAL MOVEMENT OF THE NESSON MASTER FAULT, AND RESULTED THE DRAG-FOLD DEFORMATION

FIG. 6 BAKKEN FORMATION BURIAL CURVE FROM THE CENTER OF THE WILLISTON BASIN IN NORTH DAKOTA. (AFTER PITMAN ET AL. 2001; TRAVIS 2011)

while the Antelope fault appeared to have been relatively quiescent. The vertical offset resulted in the fold-drag deformation and set the current structure of the anticline. It is worthy of noticing the descriptions given by Pilcher et al. (2011) that the structural features with NW-SE trend, such as the Antelope and Cedar Creek anticlines, were oriented optimally and strongly inverted by the Laramide tectonism. However, in this modeling work, we consider that the Antelope anticline is relative quiescent with minor displacement.

It is also believed that, during late Cretaceous, or even until early Tertiary, the Bakken was buried in its maximum depth within the oil window, as shown in Figure 6 (Pitman et al. 2001; Flannery and Kraus 2006; Warner 2011). It was very possible that the fold deformation and oil maturation occurred at the same time, and it was likely that tensile fractures could be generated during the Laramide event. Comparing to shear fractures, tensile fractures are more beneficial to reservoir quality due to their higher conductivity. On the other hand, the presence of the Nesson master fault and Antelope fault would change both the direction and magnitude of the local principal stresses, influencing the distribution and orientation of natural fractures around the faults. The tensile fractures would also function as pathways for mature hydrocarbon to migrate out of the Bakken. This paper uses finite element method (FEM) to reconstruct the paleostress during the Laramide event in Nesson anticline area based on the information from previous studies. With the simulated paleostress profile, possibility of development of natural fractures is discussed.
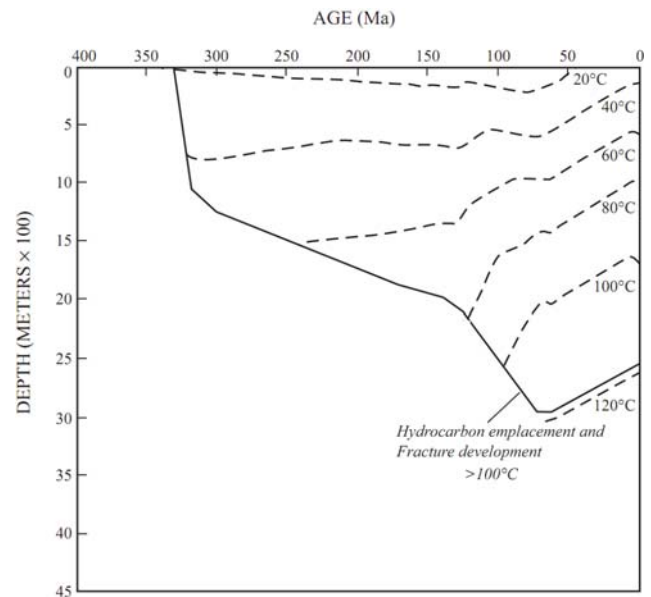
Elastic Properties

Literature review has been conducted to investigate the modeling approach and to collect related properties of the formation (Beekman et al. 2000; Zhao and Muller 2001; Gundmumdsson et al. 2010). In numerical modeling of in situ stress and structural deformation, the fault usually is modeled as a lineament, with a lower Young's modulus and higher Poisson's ratio comparing to the host rock. Gundmundsson et al. (2010) suggest that a fault zone can be modeled as a fault core in the center, sandwiched by damage zones on both sides.

Comparing the current experimental results on Bakken samples obtained by our group and other available information (Crammer 1992; Kuhlman and Claiborne 1992; Reynolds et al. 2002; Wang and Zeng 2011; Spikes 2011; Haven 2011), the Young's modulus and Poisson's ratio of the fault and the host rock used in this model are determined as in Table 1.

TABLE 1. ELASTIC PROPERTIES OF DIFFERENT MATERIALS USED IN THE MODEL.

Material No.	Geological portion	Young's modulus	Poisson's ratio
1	Fault core	5 GPa	0.32
2	Damage zone	10 GPa	0.27
3	Host rocks	45 GPa	0.27

Modeling of the Paleostress

The finite element modeling package ANSYS (2010) is used in this study. The shell element provided by

ANSYS can well model the stress and strain profile of the geological formation. The modeling area should be set large enough to offset the impact of boundary conditions to the results. The main modeling part of the three dimensional model is a rhomboid in plan view with a side length of 120 kilometers (km), and a rectangle in side view with a thickness of 1 km, starting from the basement of the basin to the top of the Bakken formation. The fault and the fautls also have a thickness of 1 km in this mdoel. The structure of the main block is shown in Figure 7. As the cardboard model described above (Figure 4), the blocks in the basin interacted with each other under the far-field effect of the Laramide tectonism. The Weldon block would subject to compressive and frictional forces from its neighboring blocks. Therefore, two rectangular blocks, A and B, are added and contact with to rhombic block on its north and south sides. The two additional blocks provide compressive and frictional effects from the neighboring blocks (Figure 8).

The Nesson master fault (about 60 km long) and the Antelope fault (about 25 km long) are put in the center of the model. The Nesson fault is represented by a fault core sandwiched by two damage zones. The Antelope fault is modeled as a damage zone because of its smaller size. Material attributes are listed in Table 1 and shown in Figure 9. In the model, 6-node and 8-node shell elements are used.
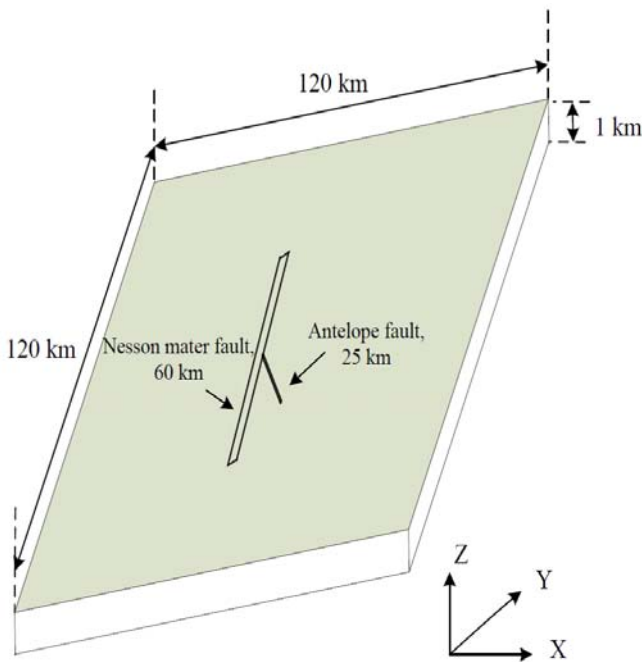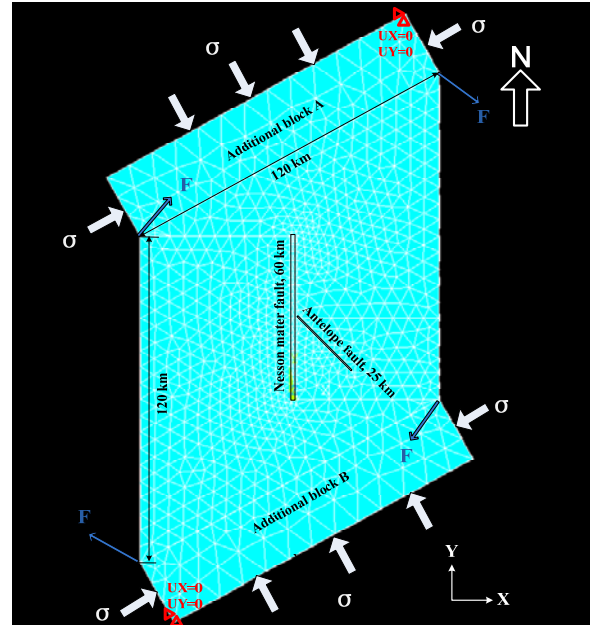

FIG. 8 PLAN VIEW FROM Z (VERTICAL) DIRECTION OF THE FINITE ELEMENT MODEL
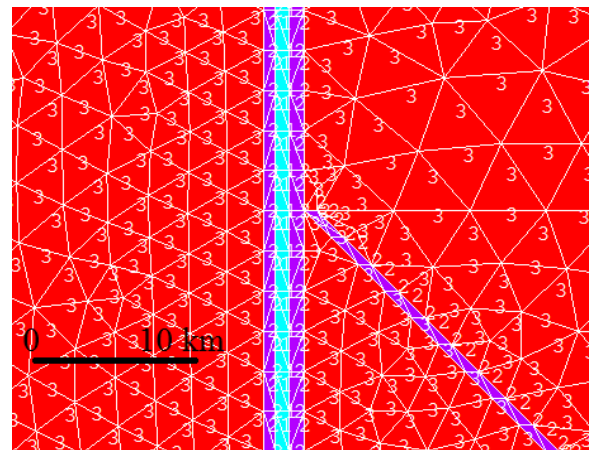

FIG. 9 DIFFERENT MATERIALS USED FOR THE ELEMENT: CYAN (1) – FAULT CORE, PURPLE (2) – DAMAGE ZONE, AND RED (3) – HOST ROCK

Displacement constraints on X and Y directions are applied on the northeast and southwest corners of the additional blocks. A vertical pressure of 70 MPa is applied to simulate the overburden pressure. Horizontal stress is applied on the three lateral faces of the additional blocks A and B. Therefore, right lateral force, or frictional forces can be provided on the contact surface between the main rhombic block and the additional blocks. To account the driving force from the corners of neighboring blocks, we add four concentrated forces at each corner of the main block, pointing to the SE, SW, NW and NE directions respectively (Figure 8). The applied stresses and forces are adjusted until the offset between the east and west of the Nesson master fault reaches about 120 m as described in the literature (Gerhard et al. 1987).

FIG. 7 STRUCTURE OF THE MAIN RHOMBIC BLOCK IN THE THREE DIMENSIONAL MODEL, WITH EXAGGERATION IN THE Z (VERTICAL) DIRECTION

Modeling Results

The modeling results show that, during the Laramide event, the maximum principal stress is in the vertical direction, and the other two principal stresses are horizontal. Figure 10 shows the contour maps of the minimum horizontal stress, maximum horizontal stress, vertical stress and stress intensity. The stress intensity is defined as (σ1-σ3), corresponding to two times of the maximum shear stress in geological convention (ANSYS 2010). For the minimum horizontal stress from Figure 10, it can be seen that tensile stress (negative value) was developed in most parts around the fault. Stresses of lower magnitude (larger tensile stress) appear in north and south of the Nesson master fault. The lowest value (maximum tensile stress) is less than -12 MPa just next to the north and south ends of the fault. There is an obvious change of the stress magnitude in and out of the fault zone. The presence of the faults, especially the Nesson master fault, has a significant impact to the magnitude of the vertical and horizontal stresses. In general, stresses in the fault zone have a lower value than those in the host rock. This is consistent to other researchers' modeling results (Gundmundsson et al. 2010)

According to Kuhlman and Claiborne (1992) and Haven (2011), it can be assumed that the tensile strength of the Bakken shale is about 6 to 9 MPa. Based on the magnitude of the minimum horizontal stress, zones of possible tensile fracture development can be recognized. Due to the accuracy of the model, it is hard to say that fracture zones can be accurately identified. However, it is fair to say that the lower the tensile stress value, the more likely the tensile fractures could be generated. Therefore, we classify the possible fractural zones as Class I and II (Figure 11). Class I refers to areas with the very low value of minimum horizontal stress (< -6 MPa), so tensile factures are developed in this zone. Class II refers to areas with minimum principal stress between -3 and -6 MPa. Tensile fractures are less developed in this zone. In zones of Class I and II, porosity and permeability could be enhanced by the fractures, and these zones are likely form "sweetspots" in the reservoir. For other areas with minimum principal stress of negative values, some tensile fractures probably exist in this zone, but not in large scale.

However, it is possible that the claystone is fractured, providing channels for the water movement and hence Figures 12 to 14 show the maps of trajectories of maximum horizontal stress in areas around the north, middle and south portions of the Nesson master fault

respectively. Due to the existence of the lateral force, the direction of the principal stresses varies across the study area. However, in general the maximum horizontal stress is in NNW direction, and the minimum horizontal stress is in ENE direction. Therefore, if any possible tensile fractures were generated under the effect of the Laramide event, fractures should be in the NNW direction, parallel to the maximum horizontal paleostress. This modeling result agrees with the hydraulic fracturing test result conducted by the Bakken Research Consortium (Headington Oil LLC and XTO Energy Inc 2008; Sturm and Gomez 2009). The project area is in Section 36-T156N-R95W in eastern Williams County, North Dakota, which is on the eastern flank of Nesson anticline, next to the Nesson master fault on its northeast. Three horizontal wells were drilled and a hydraulic fracturing test was conducted. Natural fractures encountered in the drilling are primarily in the NW direction.
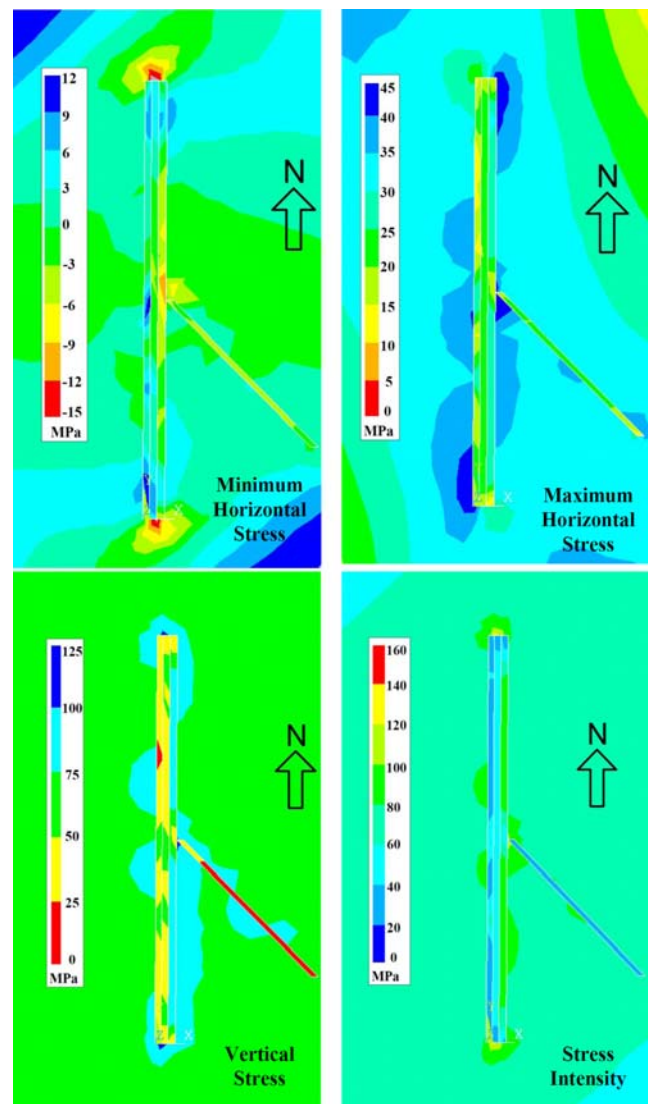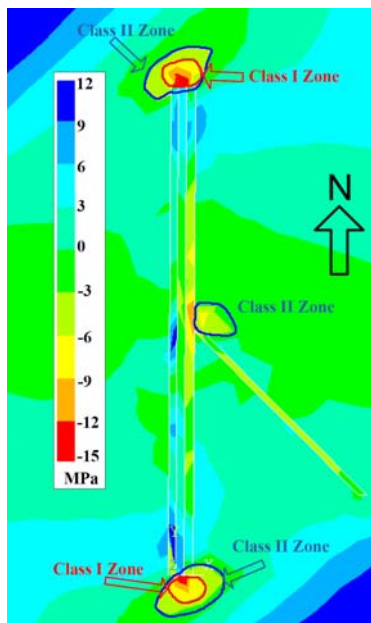

FIG. 10 CONTOUR MAP OF STRESSES

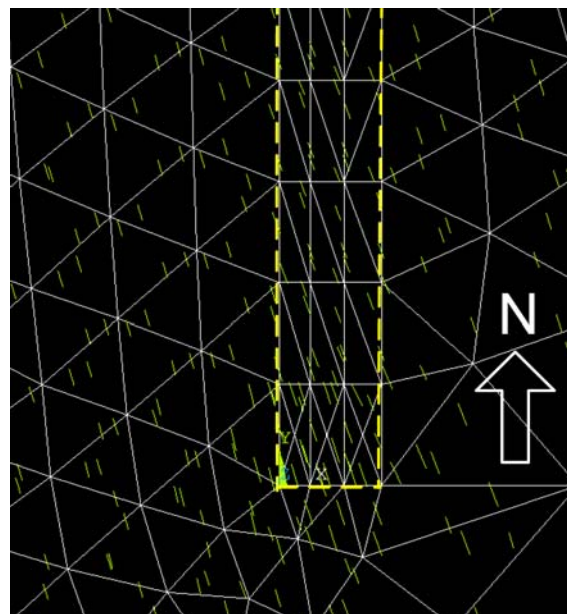FIG. 11 POSSIBLE ZONES FOR NATURAL TENSILE FRACTURE DEVELOPMENT

FIG. 14 TRAJECTORIES OF THE MAXIMUM HORIZONTAL STRESS, SOUTH PART OF THE NESSON MASTER FAULT

Discussion and Conclusion

The deformation of the Nesson anticline is controlled by the Nesson master fault beneath the west side of its crest. The vertical movement of the fault under the far-field effect of the Laramide orogeny largely determined the deformation of the fold. On the other hand, the Nesson master fault, and a secondary fault – the Antelope fault, have an obvious influence on the local in situ stress. The paleostress profile during the Laramide event has been reconstructed by using a three-dimensional finite element elastic model, which treats the geological formation as shell elements. The modeling result indicates that, in late Cretaceous, horizontal tensile stress was probably generated in areas around the Nesson master fault, and vertical stress was the maximum principal stress. On the north and south ends of the fault, the minimum principal stress reaches its lowest value; hence tensile factures are very likely developed. As a continuous, tight, self-sourced reservoir, natural tensile fractures can form "sweetspots" and greatly enhance the reservoir quality in terms of both porosity and permeability. According to the vector map of the principal stresses, the natural tensile fractures around the Nesson anticline should be in the NNW direction. The modelling result provides support to identify the "sweetspots", assess the recoverable volume, and make fplan production plan.

The modeling result also provides information for discussion of the oil migration and accumulation pattern. The Bakken shale is an excellent source rock in the Williston basin. There have been arguments that
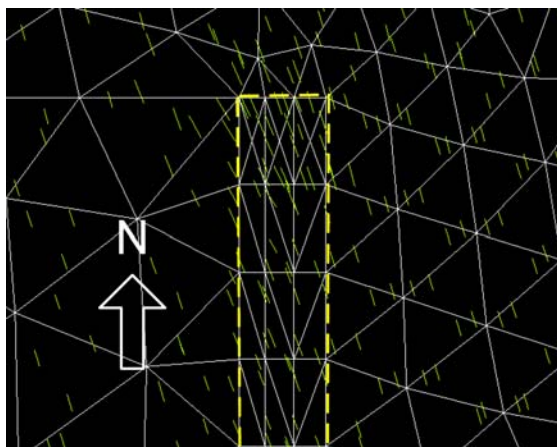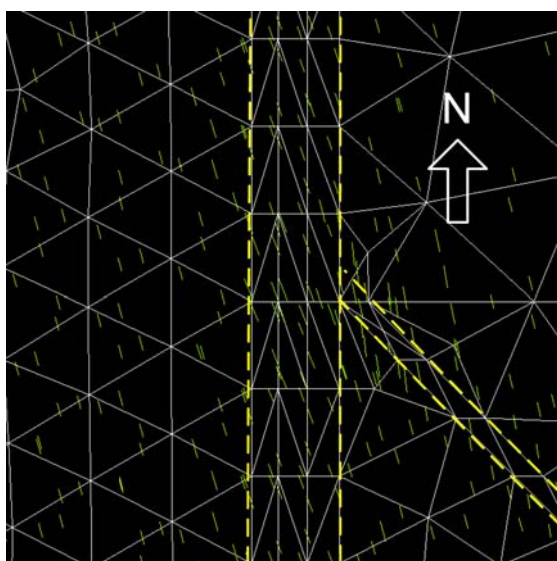

FIG. 12 TRAJECTORIES OF THE MAXIMUM HORIZONTAL STRESS, NORTH PART OF THE NESSON MASTER FAULT

FIG. 13 TRAJECTORIES OF THE MAXIMUM HORIZONTAL STRESS, MIDDLE PART OF THE NESSON MASTER FAULT

whether the generated oil is confined in Bakken or the Bakken shale is also the source rock for other Mississippian reservoirs in the basin (Dow 1974; Meissner 1978; Webster 1984; Price et al. 1984; Osadetz and Snowdon 1986; Price and LeFever 1994). As shown in the contour maps of principal stresses (Figure 10), the fault zone generally presents as an area of low stress magnitude comparing to the host rock. If the modeled paleostress regime had lasted until the post-maturation of hydrocarbon in the source rock, the stress regime should have an impact to the oil migration. It is known that the Bakken shale in the area around the Nesson anticline has generated the largest volume of oil comparing to other areas in the basin (Figure 15). The high compressive stresses in the host rock could provide driving force pushing the mature hydrocarbon to the low-stress zone in the fault from both sides. As the hydrocarbon accumulated in the fault zone, the vertical fractures may provide additional pathways for outward migration to overlying formations and other areas in the basin until suitable caprock is encountered.

In previous literature, horizontal fractures on the Bakken core samples are reported, and it is doubted that these fractures were generated by the super-lithostatic pressure due to the hydrocarbon expulsion in the shale rocks when it reached the maturation window. Since the direction of the fractures is orthogonal to the minimum principal stress, the vertical stress had to be the minimum principal stress so that the horizontal fractures could be generated when the hydrocarbon reached maturation during late Cretaceous. Nevertheless, there is no sound evidence by far that the minimum stress was vertical stress during that time. Warner (2011) suspected that the contemporaneous Laramide orogeny far-field tectonism probably generated a maximum horizontal stress regime, then joint propagation in the Bakken at that time would have likely been horizontal. However, the modeling results in this paper show that the vertical stress was the maximum principal stress under the effect of Laramide orogeny. Therefore, these reported horizontal fractures are probably generated by other mechanisms, or just caused by pressure-release during coring.

The modeling work presented in this paper provides an alternative approach to reconstruct the paleostress in the Williston basin. As mentioned early in this paper, natural fractures in the Bakken have been generated by different mechanisms at different times in the history. This modeling work focuses on the late Cretaceous period and gives an image where the tensile fractures were probably developed, as well as possible hydrocarbon migration patterns based on the paleostress profile. The model can be improved if a more accurate three dimensional geological model could be built with seismic profile and a better well control. It is also suggested that some laboratory test can be carried out to investigate the effect of stress difference on hydrocarbon migration in tight formations.
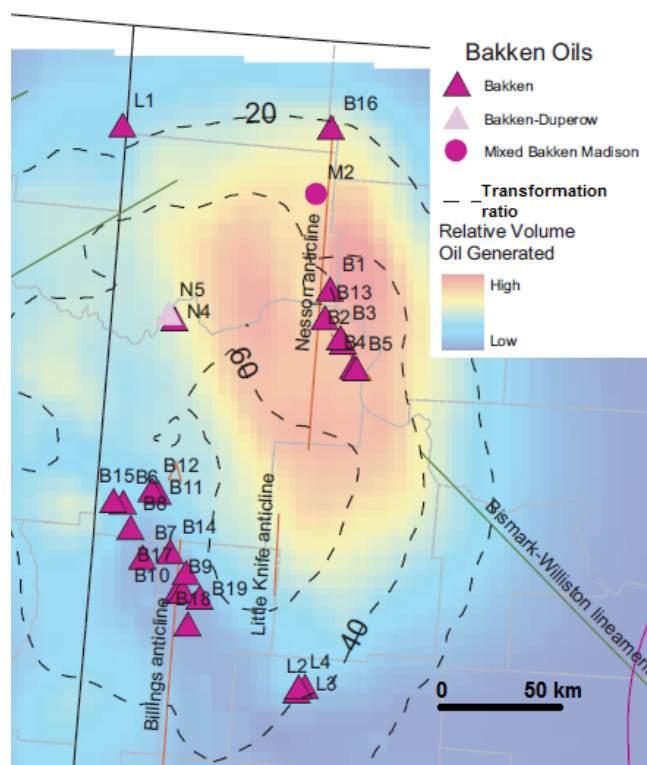

FIG. 15 RELATIVE VOLUME OIL GENERATED FROM THE BAKKEN SHALE. TRIANGLES AND CIRCLES PRESENT DATA WELLS (AFTER FLANNERY AND KRAUS 2006)

ACKNOWLEDGMENT

REFERENCES CITED

ANSYS, version 13.0, Canonsburg, Pennsylvania: The ANSYS, Inc., 2010.

Beekman, F., M. Badsi, and J. van Weesl, "Faulting, fracturing and in-situ stress prediction in the Ahnet Basin, Algeria – a finite element approach". Tectonophysics". 320 (3): 311-329, 2000.

Brown, D. L., "Wrench-style deformational patterns associated with a meridional stress axis recognized in Paleozoic rocks in parts of Montana, South Dakota, and Wyoming". In D. Rehrig, eds., Economic geology of the Williston Basin: the 24th Montana Geological Society Annual Conference and Williston Basin Symposium, Billings, Montana, 17-31, 1978.

Brown, D. L., and D.L. Brown, "Wrench-style deformation and paleostructural influence on sedimentation in and around a cratonic basin". In J.A. Peterson, D.M. Kent, S.A Anderson, R.H. Pilatzke, and M.W. Longman, eds., Williston Basin: anatomy of a cratonic oil province: Rocky Mountain Association of Geologists, 57-70, 1987.

Clark, A., "Determination of the recovery factor in the Bakken Formation, Mountrail County, North Dakota". SPE Annual Technical Conference and Exhibition, New Orleans, Louisiana, October 4-7, 2009.

Crammer, D.D., "Treating-pressure analysis in the Bakken Formation". Journal of Canadian Petroleum Technology, 44 (1): 20-27, 1992

Dow, W.G., "Application of oil correlation and source-rock data to exploration in the Williston Basin". AAPG Bulletin, 58: 1253-1262, 1974.

Druyff, L., "Reservoir properties of the Bakken Shale (abstract)". In B. Hansen, eds., Geology and horizontal drilling of the Bakken Formation: Montana Geological Society, p.91, 1991.

Flannery, J., and J. Kraus, "Integrated analysis of the Bakken Petroleum System, U.S. Williston Basin". In AAPG Annual Convention, Search and Discovery article #10105, Houston, Texas, April 10-12, 2006.

Gerhard, L. C., S.B. Anderson, and J.A. LeFever, "Structural history of the Nesson Anticline". In J.A. Peterson, D.M. Kent, S.A Anderson, R.H. Pilatzke, and M.W. Longman, eds., Williston Basin: anatomy of a cratonic oil province: Rocky Mountain Association of Geologists, 337-353, 1987.

Gerhard, L. C., S.B. Anderson, and D.W. Fischer, "Petroleum geology of the Williston Basin". In M. Leighton, D. Kolata, D. Oltz, and J. Eidel, eds., Interior cratonic basins: AAPG Memoir 51, p. 507-559, 1991.

Gudmundsson, A., T.H. Simmenes, B. Larsen, and S.L. Philipp. "Effects of internal structure and local stresses on fracture propagation, deflection, and arrest in fault zones". Journal of Structural Geology, 32 (11): 1643–1655, 2010.

Haven, J. "Mechanic properties of the Bakken Formation". Master's thesis, Colorado School of Mines, Golden, Colorado, 110 p, 2011.

He, Jun, Peng Pei, Kegang Ling, Zhenwen Zeng, and Hong Liu. "Quantificiaton of rock porosity changes before and after freezing". Journal of Petroleum Science Research 2 (3): 128-137, 2013.

Headington Oil LLC and XTO Energy Inc. "Hydraulic fracturing and microseismic monitoring project". Final report submitted to the North Dakota Industrial Commission, Contract No. G-015-028:
http://www.undeerc.org/bakken/pdfs/G-015-028_Nov_2008_Final_Report_FINAL_DRAFT_%2812_15_08%29.pdf, 2008, accessed June 4, 2012.

Kuhlman, R. D., and E. B. Jr. Claiborne. "Microfracture stress tests, anelastic strain recovery and differential strain analysis assist in Bakken Shale horizontal drilling program". Society of Petroleum Engineers Rocky Mountain Regional Meeting, Casper, Wyoming, May 18-21, 1992.

LeFever, J.A., C.D. Martiniuk, E.F.R. Dancsok, and P.A. Mahnic. "Petroleum potential of the Middle Member, Bakken Formation, Williston Basin". In J.E. Christopher, and F. Haidl, eds., Saskatchewan Geological Society Special Publication 11: Proceedings of the Sixth International Williston Basin Symposium, October 7-9, 1991, Regina, Saskatchewan: Saskatchewan Geological Society, 79-94, 1991.

Lindsay, R.F., S.B. Anderson, L.C. Gerhard, and R.D. LeFever. "Structural history and reservoir characteristics (Mississippian) of Nesson Anticline, North Dakota". In A.J. Lomando and P.M. Harris, eds., Giant oil and gas fields 2: Society for Sedimentary Geology, p. 741—802, 1988.

Ling, K., J. He, and P. Pei. "Gas-oil-water production and water-gas injection forecast in Williston Basin". Journal of Petroleum Science Research, 3(3): 119-129, 2014.

Meissner, F.F. " Petroleum geology of the Bakken Formation Williston Basin, North Dakota and Montana". In D. Rehrig, eds., Economic geology of the Williston Basin: the 24th Montana Geological Society Annual Conference and Williston Basin Symposium, Billings, Montana, 159-179, 1978.

Mullen, M., J. Pitcher, D. Hinz, M. Everts, D. Dunbar, G. Calstrom, and G. Brenize. " Does the presence of natural fractures have an impact on production? A case study from the Middle Bakken Dolomite, North Dakota". Society of Petroleum Engineers Annual Technical Conference and Exhibition, Florence, Italy, September 19-22, 2009.

Murray, G.H., Jr. " Quantitative facture study: Sanish pool, McKenzie County, North Dakota". AAPG Bulletin, 52: 57-65, 1968

Nordeng, S.H. "The Bakken Petroleum System: an example of a continuous petroleum accumulation". North Dakota Department of Mineral resources Newsletter, 36(1): 19-22, 2009.

Nordeg, S.H. "A brief history of oil production from the Bakken Formation in the Williston Basin". North Dakota Department of Mineral resources Newsletter, 37(1): 5-9. 2010.

Osadetz, K. G., and L.R. Snowdon. "Speculation on the petroleum source rock potential of portions of the Lodgepole Formation (Mississippian) of Southern Saskatchewan". In Current Research, Part B, Geological Survey of Canada, Paper 86-1 B, 647-651, 1986.

Pei, P., J. He, and K. Ling. "Correlating geomechanical properties of the Bakken formation rocks with lithofacies and sequence". In the 48th US Rock Mechanics/Geomechanics Symposium, Minneapolis, Minnesota, USA, 1-4 June 2014.

Pilcher, R.S., J.M. Coisek, K. McArthur, J. Homan, and P.J. Schmitz. "Ranking production potential based on key geological drivers—Bakken case study". In the proceedings of International Petroleum Technology Conference, Bangkok, Thailand, February 7-9, 2011.

Pitman, J.K., L.C. Price, and J.A. LeFever. "Diagenesis and fracture development in the Bakken Formation, Williston Basin: implication for reservoir quality in the Middle Member". Professional Paper 1653: U.S. Geological Survey, 2001.

Price, L.C., T., Ging, T. Daws, A. Love, M. Pawlewicz, and D. Anders. "Organic metamorphism in the Mississippian-Devonian Bakken Shale North Dakota Portion of the Williston Basin". In J. Woodward, F.S. Meissner and J.L. Clayton, eds., Hydrocarbon source rocks of the greater Rocky Mountain Region: Rocky Mountain Association of Geologists, 83-133, 1984.

Price, L.C., and J.A. LeFever. "Dysfunctionalism in the Williston Basin: the Bakken/mid-Madison Petroleum System". Canadian Petroleum Geology Bulletin, 42(2): 187-219, 1994.

Redly, P. and Z. Hajnal. "Tectono-stratigraphic evolution of the Williston Basin — a Regional seismic stratigraphic study". In L.D. Hunter and R.A. Schalla, eds., Proceedings of Seventh International Williston Basin Symposium: Montana Geological Society, 341-350, 1995.

Reynolds, S.D., D. D. Coblentz, and R.R. Hills. "Tectonic forces controlling the regional intraplate stress field in Continental Australia: results from new finite element modelling". Journal of Geophysical Research, 107(7): 2131-2146, 2002.

Spikes, K.T. "Modeling elastic properties and assessing uncertainty of fracture parameters in the Middle Bakken Siltstone", Geophysics, 76(4): 117-126, 2011.

Stark, P. "Perspective 2011: Is the U.S. on the verge of a game changer in oil?". In M. Eckhardt, et al. eds., The U.S. Energy Information 2011 Review: IHS Inc, p. 30-32, 2011.

Stockton, S.L. "The use of 3-component seismic data to indentify sweet spots in fractured Bakken reservoirs". AAPG International Conference and Exhibition, Calgary, Canada, September 12-15, 2009.

Sturm, S.D., and E. Gomez. "Role of natural fracturing in production from the Bakken Formation, Williston Basin, North Dakota". AAPG Annual Convention and Exhibition, Denver, Colorado, June 7-10, 2009.

Tertzakian, P. "Rush to oil follows shale gas trends, Journal of Canadian Petroleum Technology". 49(12): 4-6. 2012.

Thomas, G.E. "Lineament-block tectonics: Williston-Blood Creek Basin". AAPG Bulletin, 58(7): 1305-1322, 1974

U.S. Energy Information Administration. "Bakken oil production forecast to top 1 million barrels per day next month":

http://www.eia.gov/todayinenergy/detail.cfm?id=13811 accessed June 17, 2014.

Vincent, M.C. "Restimulation of unconventional reservoirs: where are refracs beneficial?". Journal of Canadian Petroleum Technology, 50(5): 36-59, 2011.

Wang, C., and Z. Zeng. "Overview of geomechanical properties of Bakken Formation in Williston Basin, North Dakota". In 45th US Rock Mechanics Symposium and 5th US-Canada Rock Mechanics Symposium, San Francisco, California, June 26–29, 2011.

Wang Fei, Shicheng Zhang, Bailong Liu. "Pressure transient analysis of multi-stage hydraulic fractured horizontal wells". Journal of Petroleum Science Research, 2 (4): 163 – 166, 2013

Warner, T.B. "Subsurface horizontal microfracture propagation within the Middle Member of the Bakken Formation, Williston Basin, North Dakota: evidence and implications". Master's Thesis, West Virginia University, Morganton, West Virginia, 59 p., 2011.

Webster, R. L. "Petroleum source rocks and stratigraphy of the Bakken Formation in North Dakota". In J. Woodward, F.S. Meissner, and J.L. Clayton, eds., Hydrocarbon source rocks of the Greater Rocky Mountain Region: Rocky Mountain Association of Geologists, p. 5781, 1984.

Zhao, S., and R.D. Muller. "Three-dimensional finite-element modeling of the tectonic stress field in Continental Australia". In R.R. Hillis and R.D. Muller, Evolution and dynamics of the Australian Plate, Geological Society of Australia Special Publication No.22: Geological Society of Australia, p. 65-83. 2001.

Peng Pei is currently a research engineer in the Institute for Energy Studies, University of North Dakota. He holds a Ph.D. degree from University of North Dakota and an M.S. Mechanical Engineering from University of North Dakota. He also has a B.S. in Mechanical Engineering from North China Electrical Power University. His research area focuses on energy-related rock mechanics.

Zhengwen Zeng is currently a senior engineer at BP America. The work reported in this paper was completed when he was an associate professor at The University of North Dakota. His research interest is geomechanics. He holds a B.S. and M.S. degree in Engineering Geology from Southwest Jiaotong University, China, a D.Sc. degree in Tectonophysics from Institute of Geology, State Seismological Bureau, China, and a Ph.D. degree in Petroleum & Geolgoical Engineering from The University of Oklahoma, USA.

Kegang Ling is an assisstant professor in Petroleum Engineering at University of North Dakota. His research interests are in the area of production optimization. He holds a B.S. degree from the China Unviersity of Petroleum in Geology, an M.S. degree from University of Louisiana at Lafayette, and a Ph.D. degree from Texas A&M University, both in Petroleum Egnieering.

Research on the Technology for Stable Production of Weathering Crust Carbonate Gas Reservoir of Jingbian Gas Field in China

Ailin Jia[1], Haijun Yan[2]

[1,2] Research Institute of Petroleum Exploration & Development, PetroChina Company Limited, Beijing,100083, China

[1]jal@petrochina.com.cn; [2]yhj010@petrochina.com.cn

Abstract

Carbonate gas reservoir plays an important role in the development of natural gas industry and its output accounts for about 30% of total output in China. Jingbian gas reservoir is the first supergiant carbonate gas field in China. By the end of 2013, the cumulative gas production of Jingbian is $654.3 \times 10^8 m^3$. That is to say Jingbian gas field has remained stable production of $50 \times 10^8 m^3$ scale for more than 10 years(Jia Ailin, 2012). Because of the cutting action of different scale troughs to formation and no uniform corrosion process to reservoir, gas field shows strong heterogeneity. On the other hand, the structure amplitude of gas reservoir is low and formation water is not active. On the whole, Jingbian gas field is a weathering crust stratigraphic – lithological reservoir(Denis Lavoie, 2011). At present, gas reservoir has entered the later period of development. The gas reservoir stable production faces three problems. Firstly, the formation pressure is low in the middle and high yield region. Secondly, the producing degree of reserves is very unevenly distributed. Lastly, intermittent wells are increasing and the productivity of gas well is low. Aiming at these problems, the stable production technology series are formed. These techniques include fine gas reservoir description, infilling adjustment, horizontal well development, booster development and fine gas reservoir management. These techniques will provide strong support for the long-term stable production and efficient development of Jingbian gas field.

Keywords

China; Jingbian Gas Field; Weathering Crust; Stable Production; Development Characteristics; Development Technology

Introduction

Jingbian gas field is a weathering crust carbonate gas reservoir and is the first found and overall developed one in the past decades in China. The overall structure is a regional large West dip monocline. The gradient of it is 7m/km~10 m/km(Huang jinla, 2011). The gas field has remained the stable production of $50 \times 10^8 m^3$ scale for more than 10 years. At present, the formation pressure is low in the middle and high yield region, Secondly, the producing degree of reserves is very unevenly distributed. Lastly, intermittent wells are increasing. Therefore, on the basis of reviewing the development history, analysis the problems in the process of development and research on the stable production technologies have great significance on realizing the long-term stable production and efficient development of Jingbian gas field.

Overview

Erdos basin is the second largest oil and gas bearing basin in China. Its area is about $25 \times 10^4 km^2$. It is a large-scale down warping basin from north to south. Jingbian gas field is located in North Shanbei Slope in the middle of Erdos basin (Figure1), and its distribution range is approximately 6000km². The major producing layers of Jingbian gas field are $Ma5_1$, $Ma5_2$, and $Ma5_4^1$ of lower Ordovician Majiagou Formation (the division of Majiagou Formation is showen in Table 1).

TABLE 1 THE DIVISION OF MAJIAGOU FORMATION

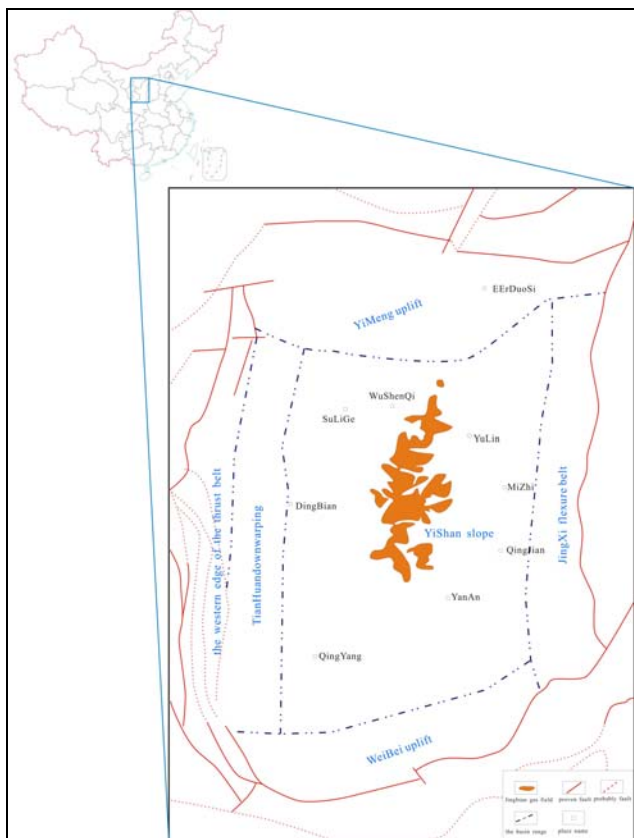| Series	Formation	Member	SubMember	Bed
Low Ordovician	Majiagou	Ma5	$Ma5_1$	$Ma5_1^1$
				$Ma5_1^2$
				$Ma5_1^3$
				$Ma5_1^4$
			$Ma5_2$	$Ma5_2^1$
				$Ma5_2^2$
			$Ma5_3$	$Ma5_3^1$
				$Ma5_3^2$
				$Ma5_3^3$
			$Ma5_4$	$Ma5_4^1$
				$Ma5_4^2$
				$Ma5_4^3$
			$Ma5_5$	$Ma5_5^1$
				$Ma5_5^2$

FIG. 1 THE LOCATION OF JINGBIAN GAS FIELD

The reservoir space includes pore, fracture and hole formed by the karstification(Su Zhongtang, 2011). Affected by the sedimentary facies and karst zone, Jingbian gas reservoir is layered distribution (Figure 2). Jingbian gas field is a typical low porosity, low permeability, low abundance carbonate gas reservoir(Shi Jianchao, 2013). In addition, Jingbian gas field has other characteristics which include strong reservoir heterogeneity, the existence of local resident water, and no edge and bottom water. The basic parameters of gas field are shown in Table 2.

TABLE 2 THE BASIC PARAMETERS OF JINGBIAN GAS FIELD

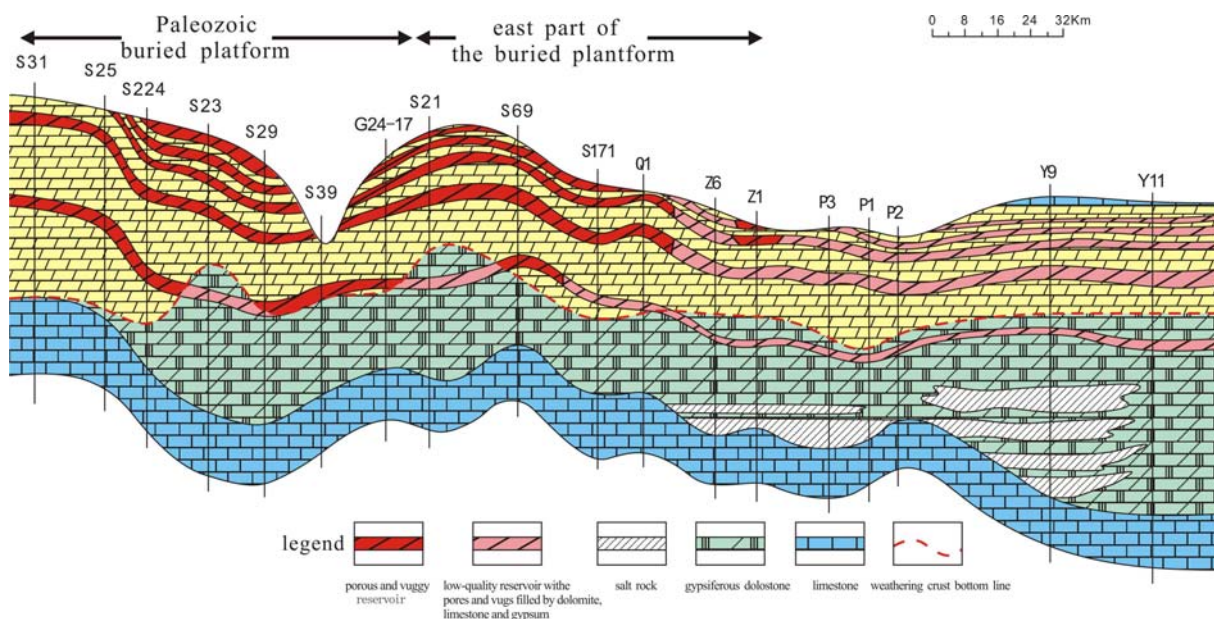| name	Jingbian gas field
region tectonic position	North Shanbei Slop in the middle of Erdos basin
discovery time	1989
proved reserves	$5477 \times 10^8 m^3$
reserves abundance	$0.91 \times 10^8 m^3/km^2$
trap types	palaeotopography and lithology comples trap
the timing of trap formation	Hercynian period
the hight of gas reservoir	-1860~-2130m
reservoir buried depth	3150~3765m
formation pressure	30.99~31.92MPa,with an average of 31.425MPa
pressure coefficient	with an average of 0.945
major layer	$Ma5_1, Ma5_2, Ma5_4^1$
sedimentary environment	tidal flat
total thickness	15~35m, with an average of 25m
effective thickness	1.4~13.7m, average 5.4m
lithology	fine powder crystal dolomite, fine-crystalline dolomite and grained dolomite
pore types	dissolved pore, intercrystalline pore and intergranular dissolved pore are the main pore types, followed by moldic pore, intercrystalline pore and microfracture
fracture types	network fractures, oblique fractures
gas water distribution	local resident water
porosity	2.53%~15.2%, with an average of 6.2%
permeability	2~10mD, with an average of 6.7mD
gas saturation	with an average of 79%

FIG. 2 PROFILE OF JINGBIAN CARBONATE GAS RESERVOIR

Development History

Jingbian gas field development had experienced four stages(Wu Yongping,2007). The production history of Jingbian gas field is displayed in Fig.3.
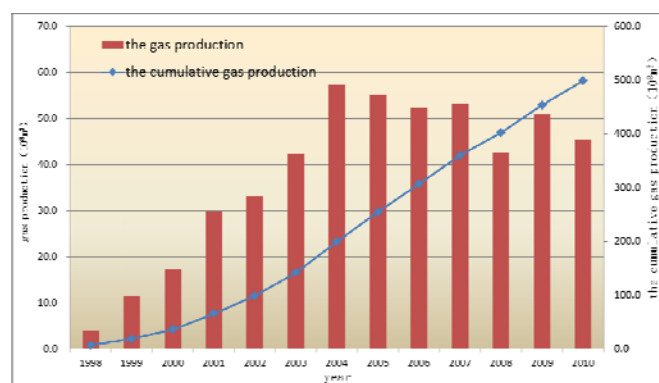

FIG. 3 THE PRODUCTION HISTOGRAM OF JINGBIAN

(1)The comprehensive evaluation and development test stage (1991~1996). The main work included reservoir comprehensive evaluation, seismic lateral predication, productivity evaluation and the establishment of preliminary development plan. This stage mainly completed gas reservoir evaluation and technology storage to lay the foundation for the field scale development.

(2)The exploratory well production testing stage (1997~1998). This stage built production capacity of $12\times10^8m^3$ and $30\times10^8m^3$ framework matching project. The study of this stage identified the major controlling factors on the distribution of highly productive gas wells and formed the well location optimization technology to provide guarantees for the efficient development of gas field.

(3)The scale development stage (1999~2003). This stage built $50\times10^8m^3$ production capacity, realized gas supply to Shanxi, Ningxia, Neimenggu, Beijing, Tianjin and the whole East China area and formed development matching technologies. At this stage, Jingbian gas field has realized the efficient development.

(4)The stable production stage (2004~now). The main works in this stage were the evaluation of surrounding areas to screen good drilling position, the infill drilling development in the internal of gas reservoir and the drilled new wells to build production capacity in the east part of the Palaeozoic buried platform and the experiment of horizontal well and side-tracking well development. The main purpose of these works was to ensure long-term stable production of Jingbian gas field.

Geological Characteristics

The gas-bearing beds of Jingbian gas field are $Ma5_1$, $Ma5_2$, $Ma5_4$ of Ordovician Majiagou Formation. The geological characteristics of gas reservoir could be summerized as followe(Jia Ailin Yan Haijun, 2013).

The Reservoir is Thin.

The $Ma5_1$ and $Ma5_2$ average reservoir is 6m to 7m in thick. $Ma5_1^3$, the main gas bearing bed, is only 3m in thick on average. Other than that, local reservoir is very tight(Wan Li, 2012).

The Reservoir is Buried Deeply.

The two Members of $Ma5_1$ and $Ma5_2$ are from 3150m to 3765m in buried depth, with an average depth of about 3500m.

The Buried Groove is Common.

More than ten Palaeozoic buried grooves from the west to the east were developed, with more than 200 less-grand buried grooves intersection with them. The two buried grooves spacing is roughly from 10km to 20 km. The groove is from 1km to 3.5km in width and from 3km to 15km in length. The maximum cutting depth is from 10m to 20m.

Local Structure is Complex.

As a whole, the structure of Jingbian gas field is a regional large West dip monocline. The gradient of it is 7m/km~10 m/km. But, there are also a series of compound nose-type folds, northeast or east-northeast trend and its uplift amplitude is from 10m to 40m. At the same time, parts of Jingbian gas field is developing nose-like sturesture and its structure amplitude is from 10m to 30m.

Development Characteristics

At present, the development of Jingbian gas field had entered the mid-late period development. The development process mainly showed the following characteristics (Sun Laixi, 2006) (Jia Ailin Yanhaijun, 2013).

(1) Due to the strong reservoir heterogeneity, the development process showed obvious unbalanced production characteristic.

Because the reservoir heterogeneity was strong, the development status of different blocks showed different characteristic. For high permeability blocks, the production time is long, and the cumulative output is high, as well as the formation pressure is

dropping quickly. So, the ability of stable production is strong, and the development effect is good. But for low permeability blocks, the production time is short, and the total output is low, as well as, the formation pressure is dropping slowly. So the formation pressure is relatively high. Consequently, the whole gas field formed some pressure drop funnels. These funnels taken middle and high yield wells as center.

(2) The development characteristic of different blocks showed great difference.

The south region of Jingbian gas field had been developed for many years and belonged to the relatively high production areas. This region showed the following characteristics in the development process. The gas wells in this region put into production early in time. So, the cumulative gas production of single well was large. At the same time, the water gas ratio was low. On the other hand, the producing degree of reserves was high and the well pattern in this region was basically perfect. So, the reserves in this region had been effectively controlled. The region of South Two belonged to water-producing area and the water production was relatively high. Its main development characteristics were put into production early in time, large water yield and high water-gas ratio, but the cumulative water production was contributed only by a handful of gas wells which produced high water yield. Now, the daily water production of 15 gas wells was more than 1m³. The water production of 7 wells among them, which daily water production was more than 3m³, accounted for 78.5% of the total water production. Another typical block was the region of 106. The 106 region belonged to low producing degree block and gas production in this region was relatively low. Its major characteristics were put into production later in time, small single well cumulative gas production, low water-gas ratio and many inefficient wells.

Main Problems

In the past years, the development practice of many years had proved that there were many problems in gas field development and these problems seriously restricted the sustainable and efficient development of Jingbian gas field. These problems mainly included the following three aspects(Jia Ailin Yan Haijun, 2014).

Low Formation Pressure in the High Yield Region Seriously Influenced the Stable Production Ability of Total Gas Field.

By the end of 2008, the average formation pressure of

Jingbian gas field was 19.98MPa. But the figure in high yield region was only 15.78MPa, which was 48.9% lower than the original formation pressure and 21% than the current average formation pressure. In August 2009, the average gas wellhead pressure was 11.23MPa. That figure was only 9.37 MPa in high yield region and was very close to outside transmission pressure (Fig.4). The geological reserves in the middle and high yield region accounted for 36.3% of total reserves. Meanwhile, the cumulative gas production in this region accounted for 50.9% of the total gas production. These regions of middle and high yield were the important foundation for the stable production of Jingbian gas field. With the gradual reduction of formation pressure, this problem will directly affect the ability of stable production and peak shaving of the whole gas field.
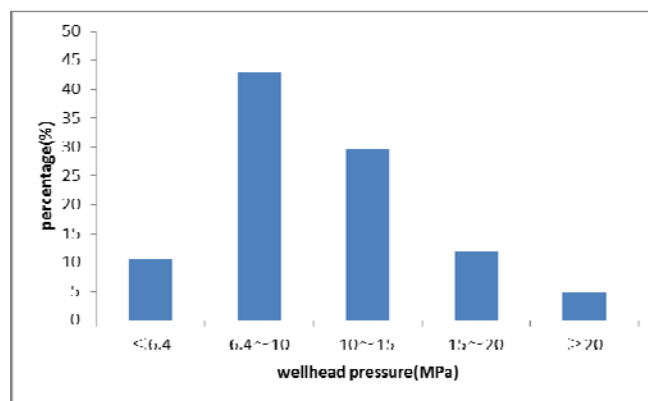

FIG. 4 WELHEAD PRESSURE DISTRIBUTION CHARACTERISTICS OF JINGBIAN GAS FIELD

The Producing Degree of Reserves was Unbalanced

The imbalance of the reserves producing degree was mainly reflected in the high producing degree in middle and high region and the low producing degree in low permeability or aquifer region. Morever, the producing degree of reserves was high in principal producing formation but the value was low in no-essential producing formation.

The biggest single well dynamic reserves was over 13×10⁸m³ but the smallest was less than 0.5×10⁸m³ according to the comprehensive evaluation results of 516 wells dynamic reserves relying on a variety of dynamic methods. the dynamic reserves of 204 wells was more than 2×10⁸m³ and the dynamic reserves of 125 wells was less than 0.5×10⁸m³. Evaluation results showed that the reserves producing degree was high in middle and high permeability zone, and the wells whose dynamic reserves was more than 2×10⁸m³ were mainly distributed in medium and high yield area. At the same time, the wells whose dynamic reserves was

less than $0.5 \times 10^8 m^3$ were mainly distributed in the low permeability or acquifer region. According to the layered testing data of 71wells from 2000 to 2006 , the producing degree of the $Ma5_1^3$ Bed was up to 96.8%, and $Ma5_1^1$, $Ma5_1^2$, $Ma5_1^4$ was 65%~ 79%, but $Ma5_2$ was only 62.2%. According to the analysis of individual well gas-producing profile, the contribution rate of gas production of $Ma5_1^3$ was generally greater than 80%, and the ratio of no-essential producing formation was less than 10% (Table 3).

TABLE 3 GAS PRODUCING PROFILE TEST RESULTS
OF G17-10 AND G26-14 WELLS

Well name	Test time	Formation	Gas production ($10^4 m^3$/d)	Contribution ratio (%)
G17-10	2005.7.18	$Ma5_1^1$	0.0801	2.37
		$Ma5_1^2$	0.0000	0.00
		$Ma5_1^3$	3.2972	97.63
		$Ma5_1^4$	0.0000	0.00
		$Ma5_2^2$	0.0000	0.00
		$Ma5_4^1$	0.0000	0.00
	2006.7.19	$Ma5_1^1$	0.0964	3.17
		$Ma5_1^2$	0.0361	1.19
		$Ma5_1^3$	2.8205	92.86
		$Ma5_1^4$	0.0000	0.00
		$Ma5_2^2$	0.0000	0.00
		$Ma5_4^1$	0.0844	2.78
G26-14	2005.6.23	$Ma5_1^1$	1.3532	15.95
		$Ma5_1^2$	0.2226	2.62
		$Ma5_1^3$	6.8275	80.49
		$Ma5_1^4$	0.0175	0.21
		$Ma5_2^2$	0.0387	0.46
		$Ma5_4^1$	0.0228	0.27
	2006.8.19	$Ma5_1^1$	0.8529	8.43
		$Ma5_1^2$	0.5243	5.18
		$Ma5_1^3$	5.5360	54.69
		$Ma5_1^4$	0.1235	1.22
		$Ma5_2^2$	0.4133	4.08
		$Ma5_4^1$	2.6726	26.40

The Intermittent Production Wells Were Increasing Gradually and the Production Capacity of these wells was Low at the Same Time
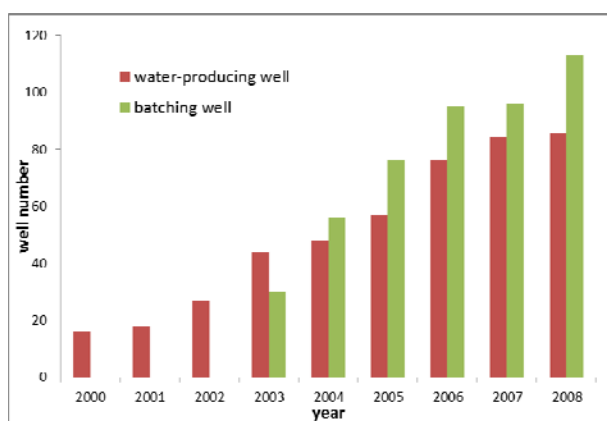

FIG. 5 THE HISTOGRAM OF BATCHING WELLS AND WATER-PRODUCING WELLS IN JINGBIAN GAS FIELD

With the formation pressure decreasing, some gas wells can't produce continuously because of low gas production ability and poor liquid-carrying capacity. In 2008, intermittent production wells had reached 113 (Fig.5). The average daily output of this kind of gas wells was $0.58 \times 10^4 m^3$/d, and the average cumulative gas productionwas $0.12 \times 10^8 m^3$. So, the average single well controlled reserves was only $0.43 \times 10^8 m^3$.

The Gas well Productivity Built is Difficult

Firstly, the proved geological reserves wsa almost all producing and the producing degree had reached 95.44% in the internal area of Jingbian gas field. The region of low productivity, low permeability area and groove edge has certain potential, but the risk of successful drilling was big. Secondly, the gas well productivity built in the external area was difficult. On the one hand, in the external area, the distribution of erosion grooves was very complicated, and the gas well control degree was low. At the same time, the reservoir physical property was more and more poor and the surface condition was more complex. On the other hand, it was difficult to build gas productivity because of the low reserves abundance.

Development Technologies

For many years, based on the development problems, some highly individualized works were carried out in order to keep the stable production and improve the recovery efficiency of Jingbian gas field. These works included well pattern infilling modification, horizontal well development, booster production experiment and so on.

Fine Gas Reservoir Description

Aiming at the main contradiction and geological problems in the process of gas field development and gas well production management, some researches were studied. These researches were including fine structure interpretation, sedimentary microfacies fine description, fine depicting ancient buried grooves, dense facies belt distribution characteristics, rich water region distribution division, reservoir property distribution characteristics and so on. These researches relied mainly on comprehensive analysis of the drilling, seismic, logging and dynamic production datas. Combining with the research results of producing degree of reserves, the result of fine gas reservoir description can supply reasonable well position for Jingbian gas field(Chen Fengxi, 2012).

Jingbian gas field was a weathering crust gas reservoir

characterized by developing different level grooves. So, the first problem in the process of Jingbian gas field is to slove this difficulty(Guo Qing, 2013). At present, the most effective way to depict reservoir groove and research its distribution was well and seismic combination. To Jingbian weathering crust carbonate gas reservoir, further research had depicted 26 three-level groove and more than 40 four-level grooves based on original 9 first-level and 16 second-level grooves. So, the description of the reservoir architecture was more precise using more and more data. These datas included seismic, single well, core, drilling, production and so on. Furthermore, reservoir classification evaluation standard had been established (Zhang Haiyong, 2012)(Table 4). The establishment of reservoir classification evaluation standard can greatly help us to research reservoir distribution characteristics of Jingbian gas field.

TABLE 4 RESERVOIR CLASSIFICATION EVALUATION STANDARD OF JINGBIAN GAS FIELD

Classification prarmeter	Type Ⅰ	Type Ⅱ	Type Ⅲ
porosity (%)	6.3~12	6.3~4	4.0~2.5
logging permeability (mD)	＞0.2	0.2~0.04	0.04~0.01
gas saturation (%)	75~90	80~70	75~60
interval transit time (μs/m)	165~188	165~160	160~155
shale content (%)	＜5	＜5	＜5
mercury injection curve type (Fig.6)	AⅠ, BⅠ	AⅡ, BⅡ	AⅢ, BⅢ
open flow potential (10⁴m³/d)	＞20	20—5	＜5

Three kind of reservoir characteristics were as follows.

- Type Ⅰ. Such reservoir was dominated by dissolved dolomite, the dissolved hole could up to 3-5mm in diameter and the fractures were also developed. So, the physical property of type Ⅰ was the most best reservoir.

- Type Ⅱ. The reservoir of this type was dominated by dissolved dolomite. Moreover, caves were relatively developed, but the caves were filled by dolomite, limestone and gypsum.

- Type Ⅲ. This reservoir was low-quality reservoir and was composed of fine crystalline dolomite. At the same time, micro fracture was highly developed. According to the common sense, the physical property of reservoir was not too bed. But, type Ⅲ had the highest filling degree of pores and micro fractures, so the reservoir physical property was the most poorest among these three types.
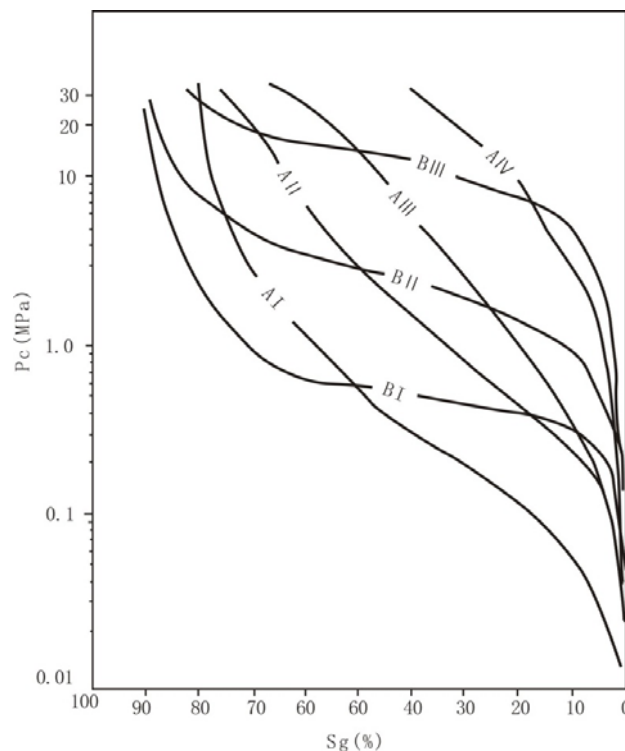

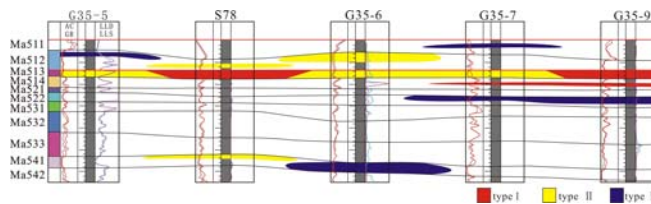FIG. 6 MERCURY INJECTION CURVE TYPE CHARACTERISTICS

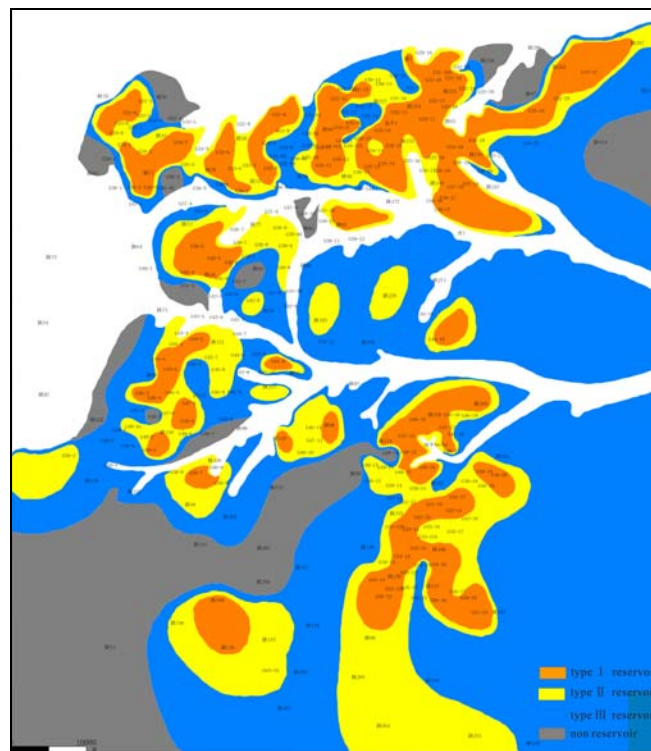FIG. 7 GAS RESERVOIR PROFILE OF JINGBIAN GAS FIELD

FIG. 8 GAS RESERVOIR PLAN MAP OF JINGBIAN GAS FIELD

Finally, it was pointed out that the distribution characteristics of different types of reservoir in vertical and horizontal direction. In the vertical direction, the reservoir was divided into two sets (the upper and the lower) (Fig.7)and the overall distribution was relatively stable. The type Ⅰ reservoir was mainly developed in the layer of Ma5$_1^3$ and the type Ⅱ was mainly developed in Ma5$_1^3$ and Ma5$_4^1$(Fig.7). But the reservoir of type Ⅲ distributed very separately(Fig.7). In the plan direction, the reservoir of type Ⅰ had a banding distribution with 3 km ~ 6 km in width and 20km in maximum length. The type Ⅱ was continuous distribution connecting with type Ⅰ reservoir in borders and bridging way. And type Ⅲ is widely distributed (Fig.8).

Well Pattern Infilling Modification

Aiming at the development potential evaluation of the body region, Jingbian gas field can successfully drill infilling wells to increase the producing degree of reserves, especially to inefficient reserves. Based on the result of fine gas reservoir description, this technique mainly included the following two aspects.

(1) Formation pressure evaluation.

The main problem in the process of formation pressure is that the pressure recovery is slow to Jingbian low permeability gas field, so just using only a single method is difficult to obtain the accurate formation pressure(Chen Jine, 2013). In recent years, we gradually formed a set of comprehensive method to determine formation pressure. This method included the establishment of monitoring well network, spot pressure test, pressure build-up well testing, whole block well shutdown and other techniques. In 2008, we had acquired 181 wells formation pressure data relying on monitoring well, spot pressure test, and pressure test of the new wells. The 181 wells, 36% of the enter gas field, provided direct basis for accurate evaluation of formation pressure. On the other hand, basing on the dynamic monitoring data and combining with the characteristics of Jingbian gas reservoir, we gradually formed a series of formation pressure evaluation technology in no well shutdown case. These methods included the pressure drawdown method, wellhead reduced pressure method, binomial productivity equation method, pseud steady state mathematical model method, and unstable yield analysis method.

The result of the formation pressure evaluation indicated that the distribution of it was not balanced.

The main factors were uneven topography of ancient structure and karst development, unbalanced micro fracture distribution and development, and large difference of the reservoir connectivity. There are 12 pressure drop units which are bordered by grooves and sub grooves. The 12 units was S17, S24, S37, S45, S62, S66, S78, S106, S121, S150, S175 and G5-8. Low pressure area, whose formation pressure was less than 16 MPa, was located in the centre of various pressure units respectively. The area of it was 683 square kilometres. The gas wells in this region were dominated by the wells of class Ⅰ. The formation pressure around the low pressure region was increasing from the centre to the edge. The area of high pressure region, whose formation pressure was more than 22 MPa, was about 1803.3 square kilometres, 48.8% of the total gas field. The high pressure region was dominated by the wells of class Ⅱ and class Ⅲ. Within the pressure units, the region with an extensive fracture distribution and good reservoir connectivity had a large range low pressure area distribution. These units include S24, S45, S17, S37, S62, S121, S78 and G5-8. Such as the S45 unit, gas well drainage radius was bigger than the half of well spacing (Fig.9).
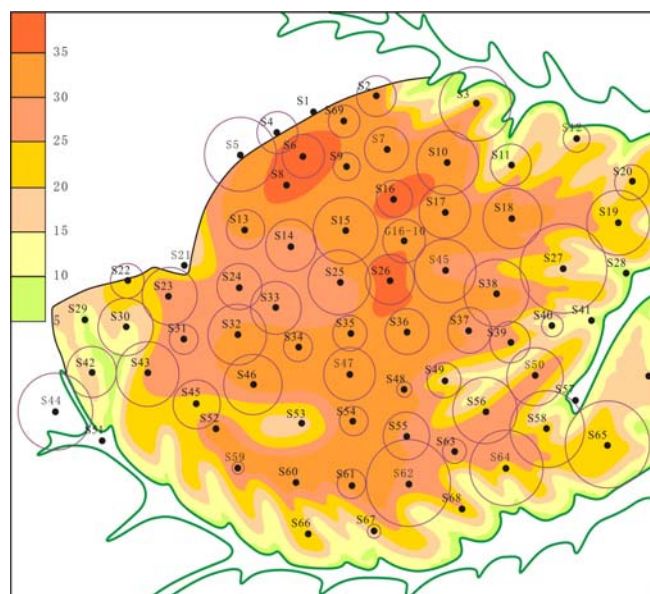
FIG. 9 THE DRINAGE RADIUS OF S45 WELL BLOCK

There is an uneven distribution of high and low pressure area in the region with a slight fracture and tight reservoir development. These units included the northern part of S106, S66, S175, around area of S37, the western part of S78 and S181. Low pressure area was isolated and centred with the well location. Such as S66 well block, gas well drainage radius was only about 674m and the connectivity between wells was poor, so there was forming five low-pressure well

points. These low-pressure points include S66, G34-11, G35-12 and G35-11 well points (Fig.10).

FIG. 10 THE FORMATION PRESSURE DISTRIBUTION OF S66 WELL BLOCK

(2)Remaining reserves evaluation.
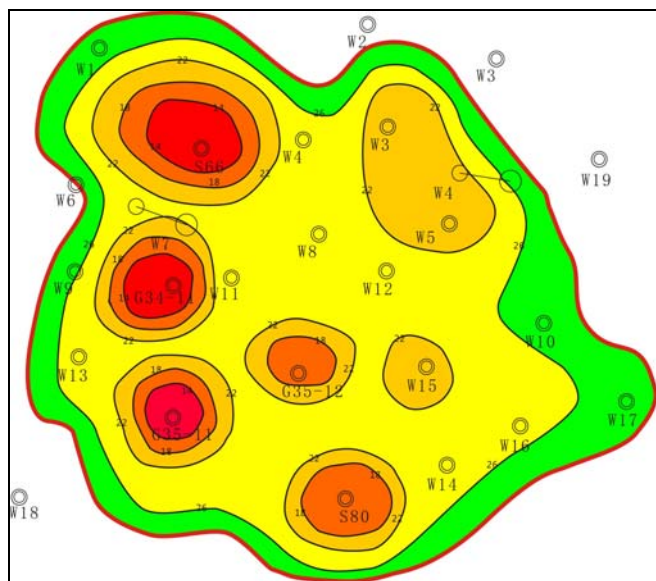
By the end of August 2009, the cumulative gas production of Jingbian gas field was $421.96 \times 10^8 m^3$, the remaining moveable reserves was $1078.04 \times 10^8 m^3$, and the remaining immovable reserves was $1231.5 \times 10^8 m^3$. In order to analyze the distribution characteristics of remaining reserves, the important way was relying on the result of gas reservoir numerical simulation in combination with geological characteristics and development dynamic characteristics of Jingbian gas field. Analysis results showed that the remaining reserves was mainly distributed in high pressure region around the centre of pressure drop unit. The formation pressure in this region was bigger than 22 MPa. Such as S17, the ratio of dynamic reserves to static reserves of the centre of pressure drop unit was as high as 90.7% and the remaining reserves was $11.96 \times 10^8 m^3$. But, this ratio in the region around the centre was only 19.2% and the remaining reserves was $85.91 \times 10^8 m^3$. According to the results of calendar gas producing profile test and gas well production dynamic data, the difference of producing degree between layers was big, and the immovable reserves was mainly distributed in $Ma5_1^2$, $Ma5_1^4$ and $Ma5_2$. The results of numerical simulation prediction showed the formation pressure of non-main layers was high, and the remaining reserves was relatively concentrated. The formation pressure of $Ma5_1$ and $Ma5_4$ layers was low but the producing degree of reserves was big. To $Ma5_2^1$, $Ma5_2^2$ and $Ma5_3$, the formation pressure of most

areas was close to the original formation pressure, and the producing degree was low. So, the remaining reserves of these beds accounted for a big proportion.

Based on the gas reservoir description, according to the results of formation pressure evaluation and remaining reserves evaluation, 35 infilling wells were drilled to increase the producing degree of reserves in body region of Jingbian gas field.

Horizontal well Development

Horizontal well development is one of the important technologies to increase the single well production and improve the recovery efficiency of the whole gas field especially for the low permeability gas field(Zhang Haiyong, 2013).

(1)Problems faced on horizontal well development in Jingbian gas field.

The problems are including the following four aspects.

- The complexity of erosion groove distribution;
- The thinness of main gas reservoir layer;
- The quickly changes of the small amplitude structure;
- The heterogeneity of gas reservoir.

(2)Technical ideas and deployment principles of horizontal well development.

Aiming at the problems faced on horizontal well development, we formed the horizontal well development technical ideas and deployment principles(Liu Haifeng, 2013).

The technical ideas of horizontal well development consist of the following four aspects.

- The fine prediction more fine level grooves and small amplitude structure;
- The fine description of formation pressure and dynamic reserves;
- Strengthen the fine gas reservoir description around the body region and research the reservoir distribution characteristics of $Ma5_1^3$ layer;
- Priority will be given to skeleton wells, adjust the horizontal deployment according to the skeleton wells implementation.

The deployment principles of horizontal well development included the following four aspects.

- The formation thickness of $Ma5_1$ and $Ma5_2$ is bigger than 20 meter, the gas reservoir

thickness of Ma5$_1^3$ is bigger than 3 meter;

- The structure is relatively gentle;
- There are seismic lines to support the horizontal well deployment;
- The deployment of horizontal wells must meet the requirements of well pattern system of the whole gas field.

(3)The effect of horizontal well development.

The horizontal well technology in Jingbian gas field had reduced the selected layer thickness of horizontal wells from 4 meters to 2 meters. This technology supplied an effective method to improve the reserves producing degree especially to low permeability area. Horizontal wells development had a very obvious effect in Jingbian gas field.

On the one hand, the drilling ratio of horizontal wells was increasing year by year (Fig.11). Such as the horizontal well of JP012-6, the horizontal section length is 1181 meters, the drilled effective reservoir is 1048 meters and the drilling ratio of effective reservoir is 90.3%. On the other hand, the open flow potential of horizontal wells is increasing gradually (Fig.11). In 2011, 9 horizontal wells was drilled in Jingbian gas field and the average horizontal section length was 1145 meters. The average open flow potential of 5 tested wells was 108×10^{4}m^3 per day, almost nine times of vertical wells.
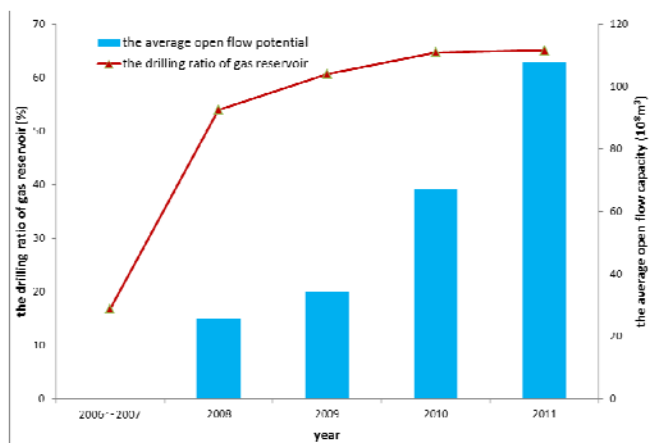

FIG. 11 THE AVERAGE OPEN FLOW POTENTIAL AND THE DRILLING RATIO OF GAS RESERVOIR OF HORIZONTA WELLS IN JINGBIAN GAS FIELD

Booster Production

Controlled by the production time and reservoir heterogeneity, the pressure drop of the whole gas filed was not balanced and wellhead pressure of part wells had dropped to the ground gathering system pressure. Therefore, it is needed to carry out the pilot test of

booster production. In January 2007, we conducted pilot test in gas gathering station of S66 of South Third block. In February 2009, we conducted pilot test again in gas gathering station of West First block. These tests had achieved remarkable effect. Firstly, the booster production can improve the production ability of gas wells. For example, the average daily volume of single well had increased from 0.84 ×10^{4}m^3 to 1.5×10^{4}m^3 of 9 wells in South Third block. Secondly, the booster production can improve the liquid-carrying capability to keep wells continuously producing. The average daily water production was increased from 4.2 m^3 to 8 m^3. Finally, the booster production can prolong the stable production period. In the process of test, the gas well allocation was 13.56 ×10^4 m^3 per day, the ratio of pressure drop was 0.0072 MPa per day, and inlet station pressure decreased from 6.4 MPa to 1.7 MPa. All of these can prolong the stable production period of 1.8 years.

Fine Management of Gas Field

In view of the huge development differences in different regions of Jingbian gas field, fine management of gas field is an indispensable work in order to realize the long-term stable production and high efficient development. According to the geological characteristics and production conditions of Jingbian gas field, we conducted a detailed division of development units in Jingbian gas field. Based on the dynamic and static parameters including production performance, gas water distribution, reservoir properties, fluid properties and the present formation pressure, we established the classification standards of development units in Jingbian gas field (Table 5).

TABLE 5 THE CLASSIFICATION STANDARDS OF DEVELOPMENT UNITS

Classification parameters	Class I	Class II	Class III
the ratio of dynamic reserves to static reserves (%)	>30	15~30	in the water rich area
the average open flow capacity (10^{4}m^3/d)	>20	<20	
the gas production per unit pressure drop (10^{4}m^3 /MPa)	>900	<900	
the degree of recovery (%)	>10	<10	
the average reasonable production allocation (10^{4}m^3 /d)	>3	2~3	
water gas ratio (m^3/10^{4}m^3)	<0.18	<0.2	>0.6
units number of classification	13	17	6

Based on the classification of development units, we put forward countermeasures of different development units to maintain long-term stable production.

①The units of Class Ⅰ. These units was mainly distributed in the body region of gas field and the technical countermeasures were fine description, profoundly exploit potentiality and enhance gas recovery. In the plane, infilling wells can improve the producing degree of reserves. Supplementary perforation and side drillings can improve the producing degree of reserves in vertical direction. At the same time, these units should reduce the gas well allocation to control the gas production rate and ensure stable gas supply in winter.

② The units of Class Ⅱ. These units was mainly situated on the east side of the gas field. The technical countermeasures were block optimization, continually build productivity and dramatically improve the single well production. Therefore, the most effective methodwas horizontal well development to improve the gas reservoir development benefit.

③ The units of Class Ⅲ. These units are mainly affected by the water production. Therefore, the technical countermeasures were strengthening evaluation and optimizing drainage water devices to produce more gas. The most important purpose is to improve the drainage water effect in the existing well network.

Conclusions

(1)The development practice of many years has proved that there are many problems in Jingbian gas field development. These problems include four aspects. ① Low formation pressure in high yield region seriously influences the stable production ability of the whole gas field.② The producing degree of reserves is unbalanced in different region.③ The intermittent production wells are increasing gradually, and the production capacity of these wells is low. ④ The productivity built of the whole gas filed is difficult.

(2) Based on the research of development problems, Jingbian gas field has formed some individual technologies. These technologies include fine gas reservoir description, well pattern infilling modification, horizontal well development, booster production and fine management of gas field. These technologies can keep the stable production and improve the recovery efficiency of Jingbian gas field.

REFERENCES

Jia Ailin, Fu Ninghai, Cheng Lihua, Guo Jianlin, Yan Haijun. (2012)."The Evaluation and Recoverability Analysis of Low-quality reserves in Jingbian gas field." Acta Petrolei Sinica, 33(S2): 160-165.

Jia Ailin, Yan Haijun, Guo Jianlin, He Dongbo, Cheng Lihua, Jia Chengye. (2013)."Development Characteristic for Different Types of Carbonate Gas Reservoirs." Acta Petrolei Sinica, 34(5): 914-923.

Jia Ailin, Yan Haijun. (2014)."Problems and Countermeasures for Various types of Typical Carbonate Gas Reservoirs Development." Acta Petrolei Sinica, 35(3): 519-527.

Sun Laixi, Zhang Liehui, Wang caili. (2006). "Recognition Distribution and Genesis of the Water-Rich strata in the Jingbian Gas Field." Sedimentary Geology and Tethyan Geology, 26(2): 63-67.

Wu Yongping, Wang Yuncheng. (2007)."Factors Influencing Natural Gas Enrichment in Jingbian Gas Field, Ordos Basin." Oil &Gas Geology, 28(4):473-478.

Su Zhongtang, Chen Hongde, Lin Liangbiao, Zhao Junxing, Liu Mingren, Ma Xueping. (2011). "Characteristics and Control Factors of Palaeokarst Reservoir of the Majiagou Formation of Lower Ordovician in Northern Jingbian Gas Field of Ordos Basin." J Mineral Petrol, 31(1):89-96.

Huang Jinla, Sun Wei, Ren Dazhong, Shi Tiaotiao, Feng Qianghan, Zhang Baoguo, Liu Haifeng. (2011). "Study on Low Amplitude Structure of Reservoir in Well J Area, Jingbian Gas Field, Ordos Basin."Geoscience, 25(2):289-296.

Wan Li, Hou Mingcai, Chen Hongde.(2012). "Sedimentary Microfacies Assemblages and Heterogeneity Controlling of Middle Ordovician Majiagou $5_4{}^1$ Sunmember Reservoir in the North Par of Jingbian Gas Field, Ordos Basin." Marine Origin Petroleum Geology, 17(4):39-48.

Chen Fengxi, Feng Qianghuan, Wang Yong, Xue Yunlong, He Liu, and Zhang Baoguo.(2012). "Fine Reservoir Description of Lower Paleozoic Gas Reservoirs and Their Development Potential in the Peripheral Area of Northern Jingbian Gas Field."Low Permeability Oil & Gas Fields, 17(3):72-76.

Zhang Haiyong, He Shunli, Men Chengquan, Gu Daihong. (2013)."The Horizontal Wells Development Optimization for the Different to Exploit Reserves in Jingbian Gas Field." Science Technology and Engineering, 13(1):140-144.

Chen Jine, He Shunli, Men Chengquan. (2013). "Applicability Research of Formation Pressure Evaluation Method in Jingbian Gas Field." Reservoir Evaluation and Development, 3(1):27-35.

Shi Jianchao, Sun Wei, Zhang Chuang, Li Hao, Huang Wei, Han Zongyuan, Zhang Zonglin. (2013). "Characteristics and Influential Factors of the Carbonaete Reservoir: a Case of M5$_4^1$ Gas Reservoir in Shanan 200 Borefield of Jingbian Gasfield." Journal of Northwest University (Natural Science Edition), 43(3):455-460.

Zhang Haiyong, He Shunli, Men Chengquan, Gu Daihong. (2012). "The Countermeasures and Application of Geological Modeling in Complex Carbonate Reservoir: Example from the Jingbian Gas Field." Natural Gas Geoscience, 23(6):1155-1162.

Liu Haifeng, Wang Dongxu, Xia Yong, He Liu, Xue Yunlong, Zhang Baoguo. (2013). "Development Geology Key Technology for Horizontal Wells of Carbonate Gas Reservoir with Low Permeability and Thin layer." Natural Gas Geoscience, 24(5):1037-1041.

Guo Qing, Sun Wei, Yu Xiaolei, Zeng Lingbang, Wang Yan. (2013). "Interpretation techniques of the Top Ordovician Erosional Surface in Jingbian Gas Field, Western Region of the Ordos Basin." Journal of Northwest University (Natural Science Edition), 43(6):947-951.

Denis Lavoie, Guoxiang Chi, Martin G. Fowler. (2011)."The Lower Devonian Upper Gaspe Limestones in Eastern Gaspe: Carbonate Diagenesis and Reservoir Potential." Bulletin of Canadian Petroleum Geology, Volume.49, Number2.

Ailin Jia, Beijing, the People's Republic of China, is a professor of PetroChina Research Institute of Petroleum Exploration & Development, Beijing, China. He holds doctor and master degree from the above institute and a bachelor degree from China University of Petroleum (east China), Dongying, Shandong provience, China, both in Oil & Gas Field Development Engineering. His research interests include oil and gas field development geology, tight gas development, carbonate gas development and enhance oil and gas recovery in low permeability gas reservoir. He has been working for more than 20 years in PetroChina Research Institute of Petroleum Exploration & Development, Beijing, China. Jia ailin is a member of the Society of Petroleum Engineers, International Association of Sedimentologists and China Petroleum Institute.

Haijun Yan, Beijing, the People's Republic of China, is a engineer of PetroChina Research Institute of Petroleum Exploration & Development, Beijing, China. He holds a bachelor degree from Northeast Petroleum University, Daqing, Heilongjiang provience, China and a master degree from PetroChian Research Institute of Petroleum Exploration & Development, Beijing, China, both in Oil & Gas Field Development Engineering. His interests include oil and gas field development geology and carbonate gas reservoir development. Yan Haijun is a member of Society of Petroleum Engineers.

Analytical Derivation of the Temperature Dependence of Absolute Permeability of a Porous Medium

Adango Miadonye[*1], and Mumuni Amadu[2]

[1]Department of Chemistry, Cape Breton University, Sydney, NS, Canada.

[2]Department of Preocess Engineering and Applied Science, Dalhousie University, Halifax, Canada.

[*1]adango_miadonye@cbu.ca; [2]mm846771@dal.ca.

Abstract

The ability of a porous medium to transmit its fluid content under an applied pressure gradient is what is called the absolute permeability when it is fully saturated with the flowing fluid. A number of publications have appeared in the petroleum literature that shows experimentally derived data on decreasing absolute permeability with temperature. By starting with the most widely cited empirical relationships between absolute permeability, porosity, irreducible water saturation and specific surface this paper has presented analytical equations first for permeability, porosity and irreducible water saturation and secondly for absolute permeability, porosity and specific surface relationship (Kozeny equation). Results of equations have been compared with published experimental work and have been found to perfectly explain observed experimental trends in absolute permeability dependence on temperature.

Keywords

Absolute Permeability; Specific Surface; Irreducible Water Saturation; Temperature Coefficients; Porosity

Introduction

The permeability of a porous medium is an intrinsic property that measures its ability to transmit fluids. It is determined by the macroscopic properties of the medium namely porosity, pore size distribution, tortuosity and specific surface. Under normal circumstances the value of permeability is independent of the type of fluid used in the porous medium where Newtonian fluids are used for measurements. Since a porous medium contains pores, the applications of thermal science to the system leads to an intuitive believe that the thermal expansion coefficient of the solid component will cause volumetric expansion with changes in temperature. Consequently, the expansion of the solids and the

matrix material of the porous medium will combine to decrease the pore spaces available for fluid flow. In this regard, thermo mechanical effects in addition to the macroscopic properties of the porous medium can lead to permeability change.

Another closely related parameter used in quantifying the ability of a fluid phase to flow in the porous medium in the presence of another is the effective permeability which is the permeability for a given saturation of the medium. Relative permeability has been found to depend on temperature [Weinbrandt et. al., Nakornthap and Evans, and Miller and Ramey Jr]. A number of publications have addressed the issue of temperature dependence of absolute permeability [Weinbrandt et. al., and Nakornthap and Evans] but no referenced literature so far has approached the issue from the mathematical point of view. Information available on temperature dependence consists of experimental presented in graphical forms. It is the prime objective of this paper to approach the temperature dependence of permeability from a purely analytical point with the view to explaining experimentally established trends in temperature dependence of permeability from the outcome of the mathematical model.

Literature Review

For the successful development of hydrocarbon accumulation, proper and systematic measurements of the permeability of core plugs from reservoirs is essential. A reasonably accurate relationship for estimating permeability of sandstones from *in situ* measurements of porosity and residual fluid saturation would be instrumental in eliminating the expense of coring. To establish such a relationship

several possibilities were tested, through laboratory measurements of permeability, porosity, and residual water saturation on 155 sandstone samples from three different oil fields in North America. The result was an empirical equation, that is widely cited in petroleum engineering literature, which was also presented in a chart format [William; and Timur]. This equation is given as:

$$K = \frac{0.136 \varphi^{4.4}}{S_{iw}^2} \qquad (1)$$

Where:

K = Permeability, md

φ = Porosity, fraction

S_{iw} = Irreducible water saturation, fraction

In addition to this equation, several empirical and semi-empirical relationships have also been developed for relating the permeability of a porous medium to other petrophysical properties [Weinbrandt et. al]. One of the most commonly used relations for permeability estimation was first developed by Blake and later, independently, by Kozeny [Weinbrandt et. al], It is known as the Kozeny equation, given as:

$$K = A_1 \frac{\varphi^3}{S^2} \qquad (2)$$

K = Permeability, md

S = Specific surface per unit bulk volume, 1/m

φ = Porosity, percent of bulk volume

A_1 = Kozeny constant

This empirical equation has also taken a different form as follows:

$$K = A_1 \frac{\varphi^3}{(1-\varphi) S_o^2} \qquad (3)$$

S_o = Specific surface per unit bulk volume

Temperature Dependence of Relative Permeability

The entire relative permeability of wetting and non wetting phases have been found [Weinbrandt et. al.,

Nakornthap and Evans, and Miller and Ramey Jr] to depend on temperature in accordance with the following already derived equations [Nakornthap and Evans]:

$$\frac{dk_{rw}}{dT} = -\frac{2+\lambda}{\lambda} \frac{(S_w - S_{wi})^{2\left(\frac{1+\lambda}{\lambda}\right)} (1 - S_w)}{(1 - S_{wi})^{2\left(\frac{1+2\lambda}{\lambda}\right)}} \frac{dS_{wi}}{dT} \qquad (3a)$$

$$\frac{dk_{ro}}{dT} = \left[\left(\frac{2+\lambda}{\lambda}\right) \frac{(S_w - S_{iw})^{2/\lambda} (1 - S_w)^3}{(1 - S_{iw})^{2\left(\frac{1+2\lambda}{\lambda}\right)}} \right] \\ + \left[1 - \left(\frac{S_w - S_{iw}}{1 - S_{iw}}\right)^{\frac{2+\lambda}{\lambda}} \right] \frac{(1 - S_w)^2}{(1 - S_{iw})^3} \frac{dS_{iw}}{dT} \qquad (3b)$$

λ = Pore size distribution index

The derivative of irreducible water saturation with temperature is positive [Nakornthap and Evans]. From equation (3b) this fact makes change of oil relative permeability with temperature positive. This means that the relative permeability of the non wetting phase (oil) increases with temperature. On the contrary, since irreducible saturation change with temperature is positive this makes the rate of change of relative permeability of water with temperature negative, an indication of relative permeability decrease with temperature. Thus, the ratio of oil relative permeability to water relative permeability will show increases with increasing temperature as illustrated by Weinbrandt et. al.

Thermal Expansivity

It is well known that the vast majority of materials expand on heating, an indication of a positive coefficient of thermal expansion [Evans]. At the simplest level this phenomenon can be traced back to the asymmetric shape of a typical interatomic potential well. For a simple diatomic molecule, the gradual population of higher energy vibration levels will lead to an increase in bond distance as temperature increases [Evans]. For more complex systems, such as most inorganic solids, one considers the population of the entire phonon density of states as a function of temperature and the population of higher energy irrational modes tends to give rise to thermal

expansion. Apart from materials with positive thermal expansion coefficient, there are certain categories of materials for which the underlying thermal expansion of chemical bonds may become dominated by other factors which tend to lead to a contraction in volume. Within certain temperature ranges such materials show the more unusual property of negative thermal expansion. The effects of vibrational energy versus interatonic distances and the thermal expansion of quartz for different scenarios corresponding to temperature increases have been well illustrated by Timur and Pape et. al respectively.

Generally, vibration modes will lead to an increase in interatomic distances and hence positive thermal expansion. Gruneisen's relationship relates the thermal expansion of a material to its volume (V), specific heat at constant volume (C_v) and isothermal compressibility C by the equation: [Evans]

$$\alpha = \gamma \frac{C_V C}{V} \tag{4}$$

γ = Gruneisen parameter ranging from 1 to 3

α is the thermal expansion coefficient. C and α_v are defined by:

$$C = -\frac{1}{V}\frac{\partial V}{\partial P} \tag{5}$$

$$\alpha_v = \frac{1}{V}\frac{\partial V}{\partial T} \tag{6}$$

α_v is the volume coefficient of the material at a constant pressure.

The thermal expansion data for a material can be used directly to obtain some information about the material in different thermal states. Equation (4) shows how the thermal expansion coefficient is related to the heat capacity and compressibility of a material via the Gruneisen parameter. Consider a porous cylindrical solid of bulk volume, V_s. An increase in temperature ∂T will lead to volume increase given by:

$$\partial V_s = \alpha_v V_s \partial T \tag{7}$$

V_s = initial solid volume

By definition, the sum of void volume and solid volume will give the bulk volume. Since for positive thermal expansion coefficient materials the volume increase affects the solid grains this expansion occurs with physical reduction in pore volume in order to maintain the balance with the net effect of a decrease in porosity.

Mathematical Modeling of the Thermal Effect

To model the thermal effect on absolute permeability empirical equation (1) will be used. This equation shows the dependence of absolute permeability on two parameters namely porosity and irreducible water saturation. From this equation therefore the following mathematical statement can be made:

$$K = \frac{0.136\varphi^{4.4}}{S_{iw}^2} \Rightarrow K = K\left(S_{iw},\varphi\right) \tag{8}$$

The total change in permeability is given by:

$$dK = \left.\frac{\partial K}{\partial \varphi}\right|_{S_{iw}} d\varphi + \left.\frac{\partial K}{\partial S_{iw}}\right|_{\varphi} dS_{iw} \tag{9}$$

The first term on the right hand side represents the partial derivative of permeability with regard to porosity at constant irreducible water saturation while the second term represents the partial derivative with regard to irreducible water saturation at constant porosity.

The partial derivative in equation (9) can be obtained individually by carrying out partial differentiations of equation (1) leading to the following:

$$\left.\frac{\partial K}{\partial \varphi}\right|_{Siw} = \frac{0.136*4.4\varphi^{3.4}}{S_{iw}^2} = \frac{0.5984\varphi^{3..4}}{S_{iw}^2} \tag{10}$$

$$\left.\frac{\partial K}{\partial S_{iw}}\right|_{\varphi} = \frac{-2*0.136.4\varphi^{4.4}}{S_{iw}^2} = \frac{-0.272\varphi^{4.4}}{S_{iw}^3} \tag{11}$$

Substituting equations (10) and (11) into equation (9) for partial derivatives gives:

$$dK = \frac{0.5984}{S_{iw}^2} d\varphi + \frac{-0.272\varphi^{4.4}}{S_{iw}^3} dS_{iw} \qquad (12)$$

To model the temperature dependence of absolute permeability the derivative of permeability with regard to temperature is considered. Therefore dividing equation (12) through by temperature change gives:

$$\frac{dK}{dT} = \frac{0.5984\varphi^{3.4}}{S_{iw}^2} \frac{d\varphi}{dT} + \frac{-0.272\varphi^{4.4}}{S_{iw}^3} \frac{dS_{iw}}{dT} \qquad (13)$$

The derivative of porosity with regard to temperature is negative due to expansion of solid grains and matrix that takes up available pore volume. The derivative of water saturation with regard to temperature is positive [Nakornthap and Evans, and Simons and Balluffi]. In other words irreducible water saturation increases with increasing temperature. Consequently, the derivative of permeability with regard to temperature is negative, an indication of permeability decrease with increasing temperature. To throw more light on this the mathematical development will be carried further.

In line with positive gradient and negative gradient with respect to irreducible water saturation and porosity respectively, gradient being considered with respect to temperature the following equations can be written:

$$\frac{d\varphi}{dT} \langle 0 \qquad (14)$$

$$\frac{dS_{iw}}{dT} \rangle 0 \qquad (15)$$

Assuming a linear relationship between irreducible water saturation and temperature and a similar relationship between porosity and temperature for simplicity the following equations can be written:

$$S_{iw} = S_{iw}^o + \mu T \qquad (16)$$

$$\varphi = \varphi_0 - \tau T \qquad (17)$$

From equation (16) and (17) the following equations can be written:

$$\frac{dS_{iw}}{dT} = \mu \qquad (18)$$

$$\frac{d\varphi}{dT} = -\tau \qquad (19)$$

Substituting these derivatives into equation (13) gives a final differential equation that models absolute permeability change with temperature accordingly as:

$$\frac{dK}{dT} = -\frac{0.5984\varphi^{3.4}}{S_{iw}^2}\tau - \frac{0.272\varphi^{4.4}}{S_{iw}^3}\mu \qquad (20)$$

Substituting linear equations for porosity and irreducible water saturation in equations (16) and (17) gives the following equation:

$$\frac{dK}{dT} = -\frac{0.5984(\varphi_0 - \tau T)^{3.4}}{(S_{iw}^0 + \mu T)}\tau - \frac{0.272(\varphi - \tau T)^{4.4}}{(S_{iw}^0 - \mu T)}\mu \quad (21)$$

Multiplying through by temperature change gives:

$$dK = -\frac{-\tau 0.5984(\varphi_o - \tau T)^{3.4}}{(S_{iw}^0 + \mu T)^2}dT$$
$$-\mu\frac{0.272(\varphi_0 - \tau T)^{4.4}}{(S_{iw}^0 + \mu T)^3}dT \qquad (22)$$

Equation (22) represents an ordinary differential equation that links permeability to temperature all other parameters being constants at reference state values. Integrating between limits gives:

$$\int_{K_0}^{K} dK = -\int_{T_0}^{T} \frac{\tau 0.5984(\varphi_o - \tau T)^{3.4}}{(S_{wi}^0 + \mu T)^2}dT$$
$$-\int_{T_0}^{T} \mu\frac{0.272(\varphi_0 - \tau T)^{4.4}}{(S_{wi}^0 + \mu T)^3}dT \qquad (23)$$

Thus:

$$K = K_0 - \int_{T_0}^{T} \frac{\tau 0.5984\left(\varphi_o - \tau T\right)^{3.4}}{\left(S_{wi}^0 + \mu T\right)^2} dT$$
$$- \int_{T_0}^{T} \mu \frac{0.272\left(\varphi_0 - \tau T\right)^{4.4}}{\left(S_{wi}^0 + \mu T\right)^3} dT \qquad (22a)$$

$$K = K_0 - \left[\int_{T_0}^{T} \frac{\tau 0.5984\left(\varphi_o - \tau T\right)^{3.4}}{\left(S_{wi}^0 + \mu T\right)^2} dT \right.$$
$$\left. + \int_{T_0}^{T} \mu \frac{0.272\left(\varphi_0 - \tau T\right)^{4.4}}{\left(S_{wi}^0 + \mu T\right)^3} dT \right] \qquad (23a)$$

K_0 and T_0 are reference values of absolute permeability and temperature respectively.

Equation (23a) can be written as:

$$K = K_0 - K(T) \qquad (24)$$

In this notation K is an arbitrary function of temperature T.

This final equation shows that with increasing temperature the initial reference state permeability K_o is reduced due to expanding solid grains and rock matrix K_o taking up pore spaces. The integration in equation (23) can be performed numerically but this effort requires accurate laboratory determination of the temperature coefficients of porosity and irreducible water saturation. In the absence of these vital data, one way to test this mathematical model is to endeavour to interpret experimentally derived curves in the light of this equation to see if these experimentally established or published work agree with the mathematical formulation.

Mathematical Modeling Using Kozeny's Equation

Kozeny's equation links the permeability of the porous medium to porosity and the specific surface per unit bulk volume. The specific surface is the sum of all internal surfaces of pores in a porous sample divided by the bulk volume of the porous sample.

The total specific surface area (SA) is a factor that can relate grain-scale properties to macro-scale physical and chemical properties of a porous medium [Miller and Ramey Jr]. In some studies attempts have been made to establish the relationships between SA and general soil physical properties namely soil texture, cation exchange capacity (CEC), and volatile organic vapor adsorption and water retention.

For a porous sample with varying particle sizes the total surface area is given by: [Lowell and Shields]

$$S_t = 4\pi\left(r_1^2 N_1 + N_2 r_2^2 + ...N_i r_i^2\right) = 4\sum_{i=1} N_i r_i^2 \qquad (25)$$

The bulk volume is given by:

$$V_t = \frac{4}{3}\pi\left(r_1^3 N_1 + N_2 r_2^3 + ...N_i r_i^3\right) = \frac{4}{3}\sum_{i=1} N_i r_i^3 \qquad (26)$$

Denoting specific surface S as the total surface area per unit bulk volume this parameter can be written as:

$$S = \frac{S_t}{V_t} = 3\frac{\sum_i N_i r_i^2}{i\sum N_i r_i^3}$$

Where M is the product of grain density and grain volume. For a porous sample with a given mean radius the specific surface is defined by:

$$S = \frac{S_t}{V_t} = \frac{3}{r_m} \qquad (27)$$

Substituting this into Kozeny's equation 2 gives:

$$K = A_1 \frac{\varphi^3}{\frac{3^2}{r_m^2}} = A_1 \frac{\varphi^3}{9} r_m^2 \qquad (28)$$

This equation shows absolute permeability dependence on porosity and mean pore radius of the porous medium. The mathematical modeling of the thermal effect can be derived from the total differential of equation (28) as follows:

$$dK = \left.\frac{\partial K}{\partial \varphi}\right|_{r_m} d\varphi + \left.\frac{\partial K}{\partial r_m}\right|_{\varphi} dr_m \qquad (29)$$

$$\left.\frac{\partial K}{\partial r_m}\right|_{\varphi} = \frac{2}{9} A_1 \varphi^3 r_m \qquad (30)$$

$$\left.\frac{\partial K}{\partial \varphi}\right|_{r_m} = \frac{1}{3} A_1 \varphi^2 r_m^2 \qquad (31)$$

Multiplying equations (30) and (31) by a sphericity factor (S_f) to account for non spherical grain shapes and substituting partial derivatives into equation (29) gives:

$$dK = \frac{1}{3} A_1 \varphi^2 r_m^2 d\varphi + \frac{2}{9} A_1 \varphi^3 r_m dr_m \qquad (32)$$

Dividing equation (32) through by temperature change to model the thermal effect yields:

$$\frac{dK}{dT} = \frac{1}{3} S_f A_1 \varphi^2 r_m^2 \frac{d\varphi}{dT} + \frac{2}{9} S_f A_1 \varphi^3 r_m \frac{dr_m}{dT} \qquad (33)$$

For a porous medium consisting of solid spherical grains increasing temperature will cause thermal expansion with a resulting increase in mean radius. Therefore the temperature coefficient of the mean radius is positive. Assuming a linear relationship between mean radius and temperature the following equation can be written:

$$r_m = r_m^0 + \beta T \qquad (34)$$

Thus:

$$\frac{dr_m}{dT} = \beta \qquad (35)$$

Equations (17) and (34) can be substituted in equation (33) to yield:

$$\frac{dK}{dT} = \frac{-1}{3} S_f A_1 \left(\varphi^0 - \tau T \right)^2 \left(r_m^0 + \beta T \right)^2 \tau$$
$$+ \frac{2}{9} S_f A_1 \left(\varphi^0 - \tau T \right)^3 \left(r_m^0 + \beta T \right) \beta \qquad (36)$$

The thermal expansivity of a geomaterial such as quartz which is the predominant mineral of sandstone is very small. The typical values for alpha quartz and silica are $42*10^{-6}$ 1/T and $7.8*10^{-6}$ 1/T respectively [Evans]. To simplify the mathematical model for a reasonable interpretation the second term on the right hand side of equation (36) will be simplified by neglecting terms with beta and tau square. Algebraic manipulation leads to:

$$\frac{dK}{dT} = \frac{-1}{3} S_f A_1 \left(\varphi^0 - \tau T \right)^2 \left(r_m^0 + \beta T \right)^2 \tau$$
$$+ \frac{2}{9} S_f A_1 \varphi^2 r_m^0 \beta \left[\beta \varphi - 3\beta \tau T \right] \qquad (37)$$

Since beta and porosity are too small their product is negligible and equation (37) can be written as:

$$\frac{dK}{dT} = \frac{-1}{3} A_1 \left(\varphi^0 - \tau T \right)^2 \left(r_m^0 + \beta T \right)^2 \tau - \frac{2}{9} A_1 \varphi^2 r_m^0 \beta \left[3\beta \tau T \right] \qquad (38)$$

Further rearrangement gives:

$$\frac{dK}{dT} = - \left[\frac{1}{3} S_f A_1 \left(\varphi^0 - \tau T \right)^2 \left(r_m^0 + \beta T \right)^2 \tau + \frac{2}{3} S_f A_1 r_m^0 \beta \tau T \right] \qquad (39)$$

This equation shows that the rate of change of permeability with temperature is negative.

Multiplying through by temperature change gives:

$$dK = \frac{-1}{3} S_f A_1 \left(\varphi^0 - \tau T \right)^2 \left(r_m^0 + \beta T \right)^2 \tau dT$$
$$- \frac{2}{3} S_f A_1 \varphi^2 r_m^0 \beta \tau T dT \qquad (40)$$

Integrating between limits give:

$$K = K_0 - \frac{1}{3} A_1 S_f \int_{T_0}^{T} \left(\varphi^0 - \tau T \right)^2 \left(r_m^0 + \beta T \right)^2 \tau dT$$
$$- \int_{T_0}^{T} S_f A_1 \frac{2}{3} \beta r_m^0 \tau \left(\varphi^0 - \tau T \right)^2 dT \qquad (41)$$

Equation (41) shows that increasing the temperature of the reservoir will lead to a decrease in the reference permeability and hence a decrease in absolute permeability.

Model Verification

In the analytical approach a linear model has been assumed for the case of porosity, irreducible water and mean grain density dependence on temperature. In thermal physics the linear relationship between the length of a material and temperature is already established by Simons and Balluffi, and Gibbons. The linear relationship between irreducible water saturation and temperature has been illustrated by Timur. In this study the linear model between porosity and temperature will be sought using the data, in Table 1, extracted from Figure 8 [Weinbrandt et. al].

TABLE 1: TEMPERATURE AND PERMEABILITY DATA [WEINBRANDT ET. AL]

Temperature (ᴼF)	Permeability (Darcy)
88.75	1.2
121.25	1.0
146.25	0.92
175	0.80
203.75	0.71
243.75	0.64
281.25	0.59

Porosity Computation

A relationship between permeability and porosity is given by the equation: [Pape et.al]

$$K = 191(10\varphi)^{10} \tag{42}$$

Thus:

$$\frac{K}{191*10 \wedge 10} = (\varphi)^{10} \Rightarrow \varphi = \left[\frac{K}{191*10 \wedge 10}\right]^{\frac{1}{10}} \tag{43}$$

Using equation (43) the following Table 2 gives values of porosity versus temperature:

TABLE 2: POROSITY VERSUS TEMPERATURE

Temperature (ᴼF)	Permeability (Darcy)	Porosity
88.75	1.2	0.0151
121.25	1.0	0.0148
146.25	0.92	0.0147
175	0.80	0.0145
203.75	0.71	0.0143
243.75	0.64	0.0142
281.25	0.59	0.0141

To verify the linear model employed in this paper the following plots are carried out:

1. The whole range of porosity versus temperature plots and a least square regression approach using linear and polynomial curve fittings.

2. Plots of porosity versus temperature for temperature range (88.75-175 ᴼF) with linear and polynomial fittings, and

3. Plots of porosity versus temperature for temperature range (175-281.25 ᴼF) with linear and polynomial fittings

The Figures 1 to 6 below indicate the individual plots for the linear and polynomial models. By comparing Figure 1, a plot of the linear model for a lower temperature range to Figure 6, a linear model plot for higher temperature range the regression coefficient for the lower temperature range is found to be more closed to one. For the entire temperature range the polynomial model appears to give a better fit than does the linear model but the difference of 0.99 for the polynomial and 0.97 for the linear model is minimal.
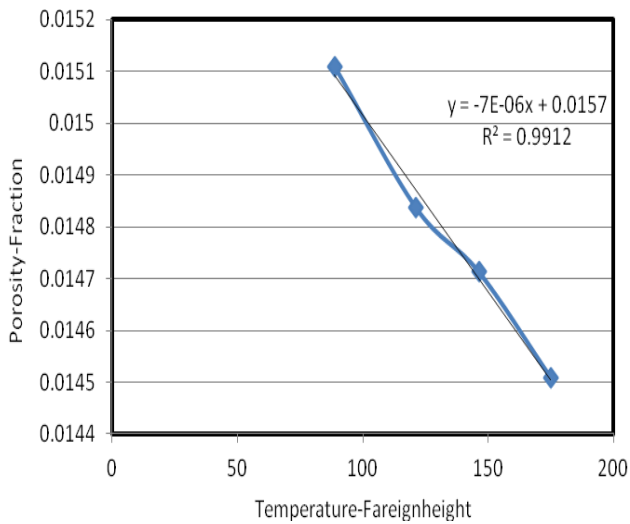
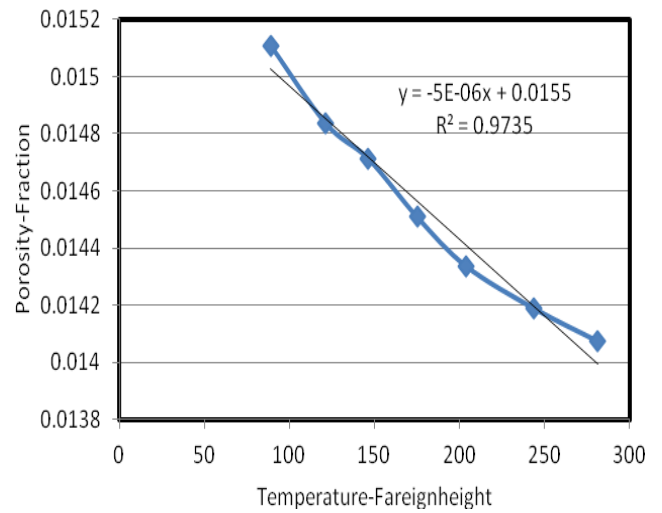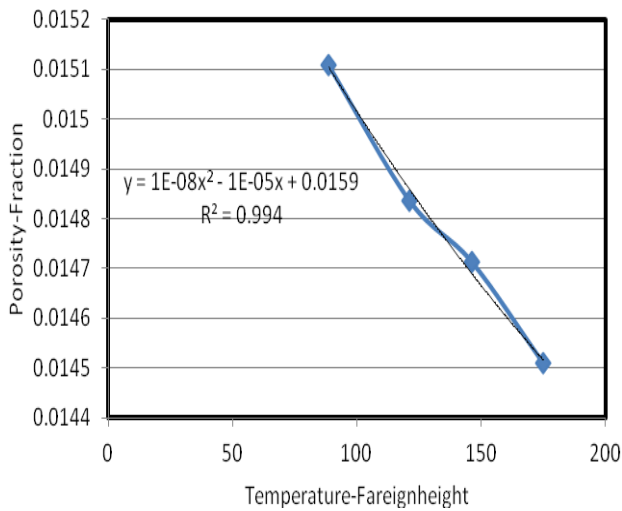FIGURE 1: LINEAR MODEL FOR TEMPERATURE RANGE FROM 88.75 - 175ºF FOR POROSITY VERSUS TEMPERATURE.

FIGURE 2: POLYNOMIAL MODEL FOR TEMPERATURE RANGE FROM 88.75-175ºF FOR POROSITY VERSUS TEMPERATURE.

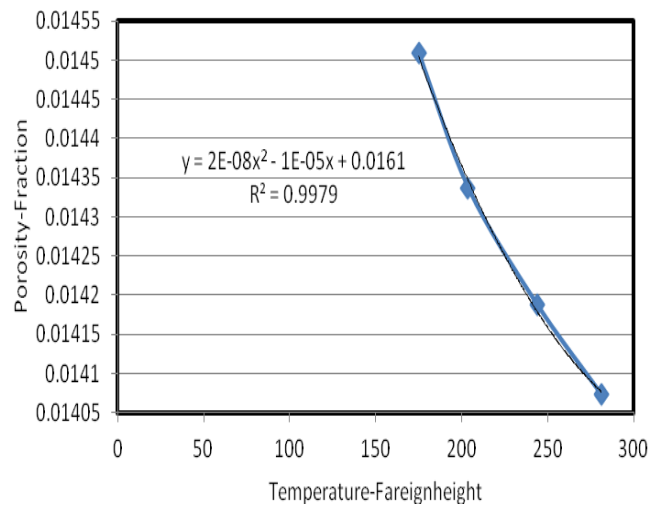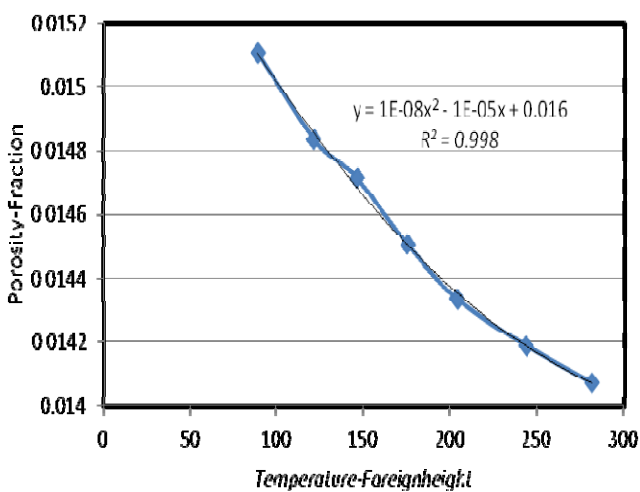FIGURE 3: POLYNOMIAL MODEL FOR TEMPERATURE RANGE FROM 88-281.25ºF

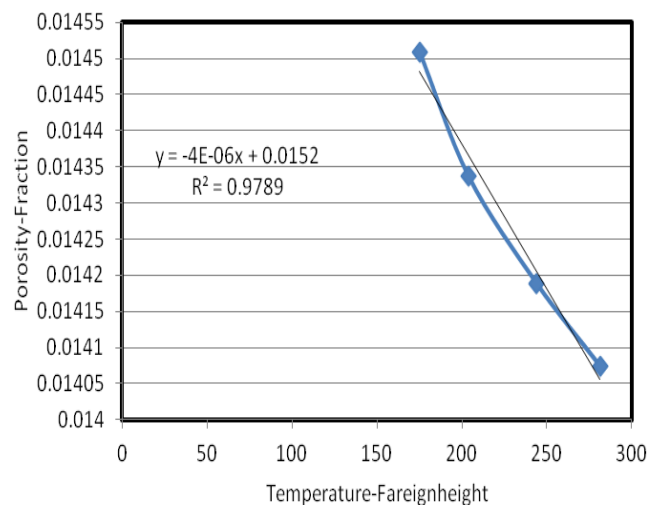FIGURE 4: LINEAR MODEL FOR TEMPERATURE RANGE FROM 88-281.25ºF

FIGURE 5: POLYNOMIAL MODEL FOR TEMPERATURE RANGE FROM 88-281.25ºF

FIGURE 6: LINEAR MODEL FOR TEMPERATURE RANGE FROM 88-281.25 ºF

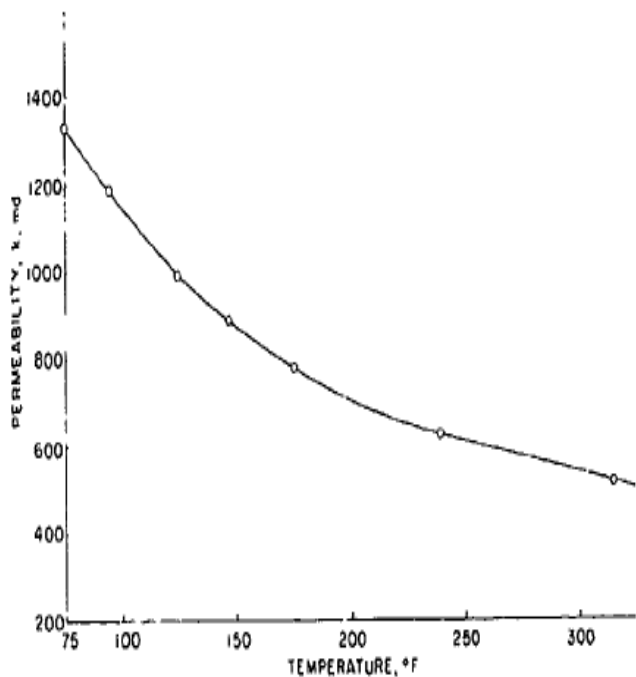*Comparison with Experimental Work*

FIGURE 7: EFFECT OF TEMPERATURE ON THE ABSOLUTE PERMEABILITY OF BOISE SANDSTONE [WEINBRANDT ET. AL]
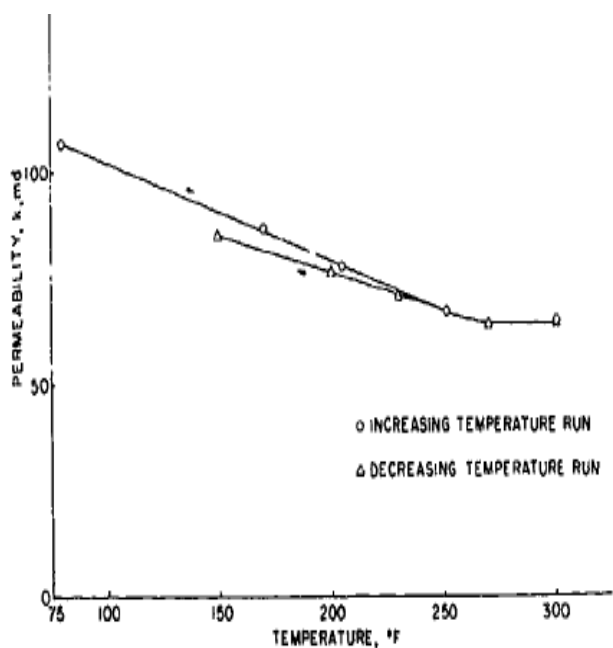

FIGURE 8: EFFECT OF TEMPERATURE ON THE ABSOLUTE PERMEABILITY OF BEREA SANDSTONE [WEINBRANDT ET. AL]

A number of publications have appeared in the petroleum literature that contains experimentally derived trends with regard to permeability and temperature. Figure 7 shows a typical trend for Boise sandstones while Figure 3 shows the trend for Berea sandstone. All these trends agree with the mathematical models established in this paper. Under normal circumstances the positive thermal coefficient of a geologic material will cause expansion due to temperature change as already discussed. This means that for a given porous medium the expansion will create less pores spaces with a net reduction of pore sizes. This will change the normal pore size distribution of the porous medium with a net increase in the number of smaller pores. Since the total pore volume of a porous medium is the sum of individual pores we should expect to see a greater contribution due to smaller pores with increasing temperature, in agreement with the results obtained by Vodak te. al.

Conclusions

The reduction of absolute permeability with temperature is an observation that has been experimentally established in the petroleum literature and that is precisely what this paper has shown mathematically. Unlike relative permeability there is so far no mathematical approach to establishing this trend. Using the most widely cited relationship between porosity, irreducible water saturation and specific surface this paper has derived analytical equations that fit well into experimentally established trends in published works. The regression coefficients observed in the plots from Figures 1 through 6 indicate that the linear model adopted by this paper is within experimental errors. The plots capture absolute permeability trends in the petroleum reservoir under thermal operations conditions. Also, the fitting of the experimentally observed trends in this work shows that viscoelastic effects were non-existent in experimental data. Therefore the analytical derivations obtained agree with experimental trends in published works documenting absolute permeability variation with temperature.

REFERENCES

Evans. J.S.O., "Negative Thermal Expansion Coefficient" J. Chem. Soc., Dalton Trans., 3317-3326, 1999.

Gibbons, D.F., "Thermal Expansion of Some Crystals with Diamond Structure". Physical Review, vol. 112, no. 1, 1958.

Lowell, S., and J. Shields, "Powder Surface area and Porosity" Third Edition. Wiley and Sons, 1979.

Miller, M.A., and H.J. Ramey Jr., "Effect of Temperature on Oil/Water Relative Permeabilities of Unconsolidated and Consolidated Sands" SPE Pacific Symposium, 1985

Nakornthap, K., and R.D. Evans, "Temperature-Dependent Relative Permeability and its Effect on Oil Displacement by Thermal Methods". SPE, Reservoir Engineering, 1986.

Pape, H., Clauser, C., and J. Iffland, **"**Permeability Prediction for Reservoir Sandstones and Basement Rocks Based on Fractal Pore Space Geometry". SEG Expanded Abstracts. García Márquez, Gabriel, Translated by Edith Grossman. London Cape, 1998.

Simons, R.O., and R. W. Balluffi, "Low Temperature Thermal Expansion Copper". Physical Review. Vol.108 , no. 2, 1957.

Timur, A., "An Investigation of Permeability Porosity and Residual WATER Saturation Relationship". PSWLA ninth Annual Logging Symposium, 1968.

Vodak, F., Trtik, K., Kapickova, O., Hoskova, S., and P. Demo, "The Effect of Temperature on Strength-Porosity relationship for Concrete. Construction and Building Materials". Science Direct, 2004.

Weinbrandt, R.M., H. J. Ramey Jr., H.J and F.J. Casse, "The Effect of temperature on Relative and Absolute Permeability of Sandstones". SPE J. paper 4142-PA, 1975.

William Lyons, "Working guide to Reservoir Engineering". Publ. Gulf Professional publishers (GPP), 2010.

Nomenclature

ϕ = Porosity

S_{iw} = Irreducible water saturation, fraction

K = Permeability, md

μ = Temperature coefficient of irreducible water, 1/T

τ = Temperature coefficient of porosity, 1/T

β = Temperature coefficient for rock grain, m/T

T = Temperature, ^{o}C

ϕ^{0} = Reference value of porosity

r_m = Mean radius of rock grain, m

r_m^{0} = Reference value of mean radius of rock grain, m

A_l = Kozeny empirical constant, non dimensional

S = Specific surface, 1/m

K = Absolute permeability, md

S_f = Sphericity-dimensionless

Adango Miadonye is a Professor of ChemicalEngineering and the Chair of Department of Chemistry at Cape Breton University. He joined Cape Breton University in 1998 after many years of university teaching and research experience in Chemistry, Chemical Engineering and Petroleum Engineering in several countries. He is a member of editorial boards of several journals for chemical engineering , and petroleum science and engineering, and served as Chair in several Research Award Selection Committees for Government and Private sectors. Dr. Miadonye is an adjunct Professor at the Department of Process Engineering and Applied Science, Dalhousie University.

Mumuni Amadu is a PhD Student at Dalhousie University Department of Chemical Engineering and a part time Instructor in Petreum Engineering Courses. His Research focus is on Carbon Geosequetsration. He worked as a Program Officer at the Ministry of Mines and

Energy(Ghana). He later worked as a Geological engineer in the same country being assigned various tasks from exploration to mine development stages. He was also a Research Assitant in Carboante Reservoirs under a Professor at the Technical Unicersity of Demmark.

Mr. Amadu was a student member of Soceity of Petroleum Engineering at the Technical University of Denamrk. A number of abstracts from his ongoing research work have been accepted by international Journals in Dedicated this area.

Evaluation of the Efficiency of Additives on the Destabilization of Petroleum Emulsions

Érika A. Jarque, Priscila F. Oliveira and Claudia R. E. Mansur[*]

Federal Universityof Rio de Janeiro – InstituteofMacromolecules – Av. Horácio Macedo, 2030 – Ilha do Fundão, 21941-598, Rio de Janeiro, RJ, Brazil.

[*]celias@ima.ufrj.br

Abstract

The demulsification process is extremely important in the petroleum industry because the natural formation of water-in-oil (w/o) emulsions hinders the performance and increases the cost of the production and processing of crude oil. Commercially produced polymers have been widely used as additives to destabilize these emulsions, among them block copolymers of poly(ethylene oxide) and poly(propylene oxide), or PEO-PPO block copolymers. This article reports the performance of a series of commercial demulsifiers based on silicone polyethers, containing PEO or PEO-PPO block copolymers in their chains. The stability of the w/o emulsions, with and without the additives, was evaluated by determining the water/oil interfacial tension, the compressibility of the films formed at these interfaces and the gravitational separation of oil and water by the bottle test. The results show that the addition of these additives reduced the interfacial tension of the systems, indicating the adsorption of their molecules at this interface. All the additives promoted the breakdown of the w/o emulsions, but those with higher molar masses and chains of PEO-PPO block copolymers were the most efficient.

Keywords

Demusifiers; Silicone Polyether; Petroleum Emulsion

Introduction

During the extraction of crude oil, the mixture of water and oil is subjected to turbulent flow, promoting the dispersion of the water in the form of small droplets and resulting in the formation of emulsions. The fractions of crude oil with polar characteristics, such as asphaltenes and resins, act as natural emulsifiers, which migrate to the oil/water interface and form a film that acts as a barrier, preventing the coalescence of the water droplets and generating stable emulsions [1-3]. To destabilize these emulsions it is necessary to add chemical products called a demulsifiers. These additives are generally employed in gravitational separation tanks that are used to separate the oil, gas and water phases, remove emulsifying reagents present at the phase interfaces,

and permit the coalescence of the water droplets associated with the crude oil being pumped.Poly(ethylene oxide)-poly(propylene oxide) (PEO-PPO) block copolymers have been widely studied and used for this purpose in the petroleum industry. These molecules contain a structure that is partly hydrophilic, which preferentially interacts with water molecules, and another part that is hydrophobic, with greater affinity for the oil phase. These characteristics enable these molecules to be adsorbed at the interface [4-10]. Extensive studies have been conducted to identify the conditions and factors that influence the stability of w/o emulsions [11,12]. The best understanding of the stability of these emulsions is provided by rheology, which investigates the interfacial properties between water and oil.Some studies have shown that an emulsion's stability is related to changes in the properties of the interfacial film during compression. Measurement of surface pressure isotherms of compressed droplets allows determining the interfacial compressibility and the crumpling ratio, defined as the ratio of the surface area of the compressed film in relation to initial surface area [13].The surface pressure (π) is defined by Equation 1, where $\gamma_o$is the interfacial tension without the presence of surfactants and γ is the system's tension with addition of surfactants [14].

$$\Pi = \gamma_o - \gamma \qquad \text{Equation (1)}$$

The film's surface pressure is determined and plotted as a function of the film ratio, $A/(A°)$(ratio of the interfacial area after compression, A, and the initial area, A°, in a given time of droplet aging. At each time, the interfacial compressibility is determined by Equation 2 [13]:

$$Ci = -\frac{1}{A}\frac{dA}{d\pi} = -\frac{d\ln A}{d\pi} \qquad \text{Equation (2)}$$

where Ci is the interfacial compressibility (mmN-1), A is the surface area (m) and π is the surface pressure (mNm-2).

The compressibility can be calculated in interface as a change in the curve of the surface pressure versus the logarithm of the surface area.It is still not clear how to predict the interaction of different surfactants with the emulsion's interface. One of the hypotheses is that an efficient surfactant acts by partially or completely substituting the asphaltenes at the interface, weakening the film irreversibly (by increasing its compressibility and diminishing the crumpling ratio) or completely replacing it with a reversible surfactant film. By this hypothesis, weak films should favor coalescence of the water droplets, making emulsions more unstable.

Therefore, it is important to study new surfactants to learn how they act at the interface of emulsions, to propose treatment methods to minimize the problems caused by the formation of emulsions. This article evaluates the efficiency of new additives based on silicone polyethers in the process of destabilizing water-in-oil (w/o) emulsions. For this purpose, the interfacial properties were investigated of w/o systems in the presence of the additives tested and the stability of the emulsions was evaluated by the bottle test, which measures the gravitational separation of water from oil. The additives tested here have already been evaluated in previous studies of the process of destabilizing foams formed in crude oil [15-17]. Although there are many factors that influence the performance of the gravitational separation tanks, the main problem is the formation of foam. Since antifoam additives are mainly used in these separators, it is very important that these be effective in breaking down w/o emulsions, to reduce operational costs of oil production.

Experimental

Materials

Five silicone polyethers were investigated in this study, all donated by the company Momentive and are identified with the prefix SP. The company's specifications of these products are shown in Table 1.

TABLE 1. CHARACTERIZATION OF SILICONE POLYETHER

Sample	$\overline{M}$w	% Silicone	% EO	% PO
SP1	9000	60	40	--
SP2	10000	65	35	--
SP3	8000	20	50	30
SP4	20000	35	45	20
SP5	20000	30	40	30

(a) Data supplied by the donor company.

The polyether groups are composed of poly(ethylene

oxide) (PEO), containing or not poly(propylene oxide) (PPO), in different proportions. According to the donor company, the polyether groups are added to the polysiloxane chains by hydrosilation. This process results in an alkyl group in which the PEO and PPO are added along the siloxane chain by a series of Si-C bonds that are hydrolytically stable. Figure 1a shows the structure of the samples grafted only with PEO chains, here called SP1 and SP2. Figure 1b depicts the structure of the samples grafted with PEO-PPO block copolymers, called SP3, SP4 and SP5.
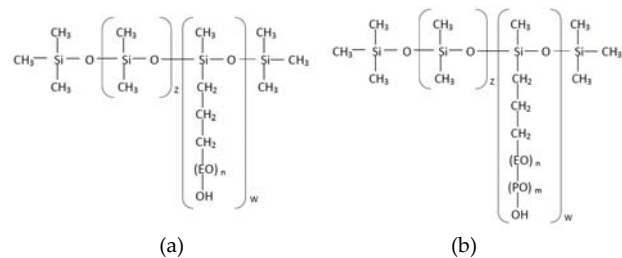

(a)   (b)

FIGURE 1: STRUCTURE OF THE SILICONE CHAIN GRAFTED WITH (A) POLY(ETHYLENE OXIDE); (B) POLY(ETHYLENE OXIDE)-POLY(PROPYLENE OXIDE) BLOCK COPOLUMERS

The crude oil sample came from a Brazilian oil field. The chemical and physico-chemical characteristics of this sample, with respect to the level of saturates, aromatics, resins and asphaltenes (SARA), water content and density (°API) [18] were determined according to the procedures described in a previous paper [19]. The results are shown in Table 2. The concentration of asphaltenes (2.4 %wt) found in this oil indicated it was suitable for our purposes, since the asphaltenes present in an oil sample have a significant influence on the stability of water-in-oil emulsions. Synthetic emulsions prepared from samples of this type of oil must show clear differences in the capacity for demulsification when comparing different demulsifier systems.

TABLE 2. CHEMICAL AND PHYSICO-CHEMICAL CHARACTERISTICS OF PETROLEUM

Properties	Petroleum
Water content (wt%)	0.05
°API	21.2
Saturates (wt%)	40.7
Aromatics (wt%)	34.1
Resins (wt%)	22.9
Asphaltenes (wt%)	2.4

Methods

1) Preparation of Silicone Polyether Solutions

Normally, the polymer additives utilized in the petroleum industry must be dispersed in solvents, due to the high viscosity or are in solid form. For

this reason, the silicone polyether solutions were prepared utilizing toluene as the solvent.The silicone polyether solutions were prepared at a concentration of 40 %wt – the same concentration of the formulations used in oil fields – to evaluate their efficiency in destabilizing the oil emulsions.

2)   Analysis of W/O Interface Tension

The aqueous phase consisted of saltwater, composed of 55 000 ppm of the salts NaCl/CaCl (10:1). The saltwater/oil interface tension measurements were obtained by the pendant drop method using a DataPhysics model OCA-20 automatic contact angle meter (goniometer), to observe the interfacial behavior of the additives as a function of time. All these measurements were carried out at 25 °C. The additives were dispersed in the oil phase (crude oil). All the analyses were performed at a concentration of 50 ppm of the additive.In pendant drop tests, a droplet of oil is formed at the end of a straight needle (d= 0.89 mm) connected to a syringe with electronic control of the droplet, within an optical glass cuvette containing a fixed volume of the additive solution. The droplet issubjected to interfacial tension and gravitational forces and is filmed by a camera. The measurements were taken at one-minute intervals and the interfacial tension (γ) was determined by digitalizing the images and analyzing the droplets' profile by applying the Young-Laplace equation (Equation 3) [20].

$$\Delta P = (\varrho o - \varrho a)\ g\ h = (1/r_1) + (1/\ r_2) \qquad \text{(Equation 3)}$$

Where:

ΔP is the pressure difference across the interface (inside – p1 and outside – p2 the droplet); ϱo and ϱa are the densities of the oil and aqueous phases, respectively; g is gravity; h is the height of the liquid column of the droplet and r1 and r2 are the principal radio of curvature. The errors of these measurements are indicated in the equipment manual as being 10%.

3)   Tests of the Gravitational Separation Efficiency of the Silicone Polyether

The performance of the additive solutions prepared in toluene, at a concentration of 40%wt, was evaluated using the saltwater/crude oil gravitational separation test, or the bottle test, to test the as-prepared emulsion [9]. The additives were evaluated at a concentration of 50 ppm and the tests were run by placing the test tube containing the emulsion and the surface agent in a temperature-controlled bath at 60 °C after vigorous agitation. Water separation was observed at time intervals of 5 to 65 min. To prepare the saltwater-in-oil emulsions, the saltwater solution, composed of 55 000 ppm of the salts NaCl/CaCl (10:1), was prepared using Ultra Turrax T 25 agitator at 6000 rpm for 3 min. The saltwater was added to the crude oil, and the water/oil ratio in the emulsion was 50:50. The synthetic emulsions were characterized by means of the determination of water content by potentiometric titration from use of the titration set by Karl Fisher reagent and all synthetic emulsion samples presented water content about 50% v/v. In addition, it was determined the droplet size of emulsions with optical microscopy and it was observed sizes in the range of 10-12 micrometers. The efficiency of each formulation used in these tests was calculated by applying Equation [4,5,6,9,21]:

$$EF_{WO} = (V_{WS}/V_{WT})\ x\ 100 \qquad \text{(Equation 4)}$$

Where:

EF_{WO} is the efficiency of gravitational separation of water and oil (in % by volume); V_{WS} is the volume of water separated during the test (in mL); and V_{WT} is the volume of total water inside the test tube (in mL). All measurements were taken in triplicate. The values presented in the table are the averages, accompanied by the respective standard deviations.

4)   Extraction of the Asphaltene Molecules

The asphaltenes were separated from the crude oil sample by the difference of solubility, using a Soxhlet extractor. This procedure involves the addition of an excess of a flocculant (n-heptane) to the oil in the proportion of 1:5, promoting reflux for 1 hour, followed by filtration through filter paper at room temperature (25 °C). In this procedure, the asphaltenes, which are insoluble in n-heptane, are separated by precipitation, while the resins, which are soluble in this solvent, remain in solution. The resins can be recovered after evaporation of the n-heptane in a rotary evaporator, at a temperature of 50 °C. The precipitate obtained was added in a thimble formed of filter paper inside the Soxhlet device and submitted to extraction with toluene in a proportion of 1:3, until the solution appeared clear in the apparatus. The asphaltenes, soluble in this solvent, were recovered after evaporation of

the toluene in a rotary evaporator at a temperature of 70 °C. After being dried, the asphaltene samples were placed in closed flasks covered with aluminum foil to prevent their oxidation. Solutions containing 40 %wt of additive in toluene were prepared, and these solutions were applied at a concentration of 50 ppm.

Results and Discussions

Determination of the Water/Oil Interfacial Tensions

As described above, the interfacial tensions were measured by the pendant drop method. This method permits monitoring the variation in the water/oil interfacial tension as a function of time. With this it is possible to obtain these values when the processes of diffusion, adsorption, reorganization at the interface, desorption and transfer of molecules to the other phase occur. All the tests were performed at a temperature of 25 °C.The silicone polyether solutions were dispersed in the oil phase at a concentration of 50 ppm. As shown in Figure 2, all the additives reduced the interfacial tension.

The curves shown in Figure 2 provided other information important to the study of the water/oil interface: the additives rapidly reduced the interfacial tension values of the systems evaluated, behavior that can be related to the formation of the water/oil interfacial film in the emulsion.

By analyzing initially additives containing only ethylene oxide units in their chains (SP1 and SP2) can be observed that which has the lowest concentration of silicone, SP1 (Table 1) reduced the interfacial tension values of the water-in-oil system most
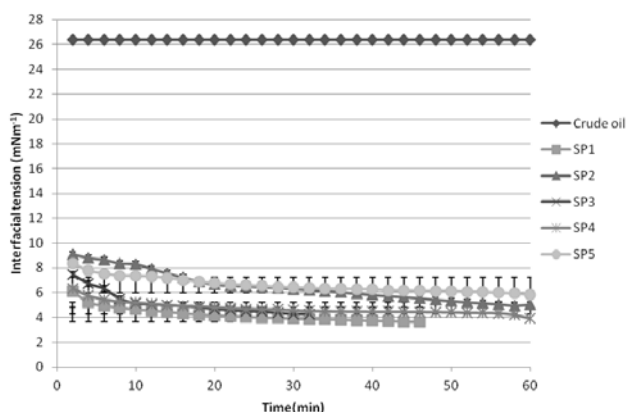

FIGURE 2: EFFECT OF THE ADDITIVE SOLUTIONS ON THE WATER-OIL INTERFACIAL TENSION MEASURES

According to the literature [22], the faster the minimum

interfacial tension values are reached, the faster the additive's molecules diffuse to the interface, leading to the formation of thin films with low elasticity, which are more easily ruptured, allowing the water droplets to coalesce. Therefore, all the additives assessed in this study are suitable for application as demulsifiers of water-in-oil emulsions. Table 3 shows the interfacial tension values obtained after the end of the analysis (approximately one hour).

TABLE 3. INTERFACIAL TENSION VALUES ONE HOUR AFTER THE START OF THE ANALYSIS

Additive	Petroleum-additive interfacial tension (mNm^{-1})
----	26.5 ± 2.6
SP1	3.6 ± 0.4
SP2	5.0 ± 0.5
SP3	4.5 ± 0.5
SP4	4.5 ± 0.5
SP5	5.8 ± 0.6

This behavior agrees with other findings in the literature [23] and , according to which nonionic surfactants derived from EO (ethylene oxide condensates of hexadecanol and dodecanol alcohols) have smaller areas at the water/ ar interface the derivatives of hexadecanol (less hydrophobic), although the difference is small. According to the Gibbs adsorption isotherm [24], the smaller this area is, the greater will be the interfacial tension reduction. For the other additives (SP3, SP4 and SP5), the presence of the propylene oxide units in their chains appears to hinder the packing of these chains at the interface more, acting to increase the interfacial tension values obtained. This behavior can particularly be observed when comparing the results for the additives SP4 and SP5 (with higher molar masses): the concentration of silicone units in the chains of additive SP5 is lower, which could cause a lower water/oil interfacial tension value for this additive. However, this additive showed the highest interfacial tension of all the additives analyzed, which can be attributed to the higher concentration of PO units in its chains.

Effect of the Additives on the Stability of the Emulsions

1) *Tests of Gravitational Separation of Water*

The performance of the silicone polyether samples in destabilizing the w/o emulsions was evaluated by the bottle test. The efficiency of each formulation utilized in these tests was calculated by applying Equation 4. All the measures were taken in triplicate and the values presented are the

averages followed by the respective standard deviations. The synthetic w/o emulsions remained stable for 70 minutes after their preparation, a longer interval than used in the water/oil gravitational separation tests, indicating that the synthetic w/o emulsions would remain stable during the entire period of the tests after inclusion of the additives. Figure 3 shows the gravitational separation efficiency for each additive tested.
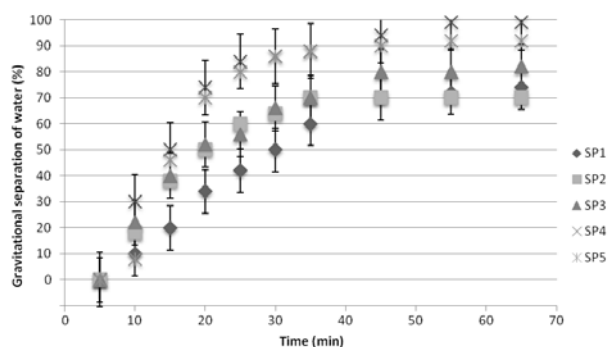

FIGURE 3: GRAVITATIONAL SEPARATIONAL EFFICIENCY OF THE W/O EMULSIONS IN THE PRESENCE OF THE SILICONE POLYETHER SOLUTIONS

The results of these tests indicated that although all the samples reduced the water/oil interfacial tension (Table 3), indicating adsorption of their molecules at the interface, these additives did not cause stabilization of the emulsion. This behavior can be observed by the breakdown of the emulsion promoted by these additives, which caused satisfactory water separation (above 60%). The destabilization of the emulsions occurred due to the rapid adsorption of the silicone polyether molecules at the interface, as observed previously in the interfacial tension measurements shown in Figure 2. This indicates the formation of a thin film more prone to rupture, destabilizing the emulsion by allowing the water droplets to coalesce. The most efficient additives in destabilizing the w/o emulsions were SP4 and SP5 (above 90% water separation). These two additives have the highest molar mass values. It can also be observed that SP4 (which has a greater concentration of silicone in its chains) was slightly more efficient (99%), although the range of values obtained for the two additives overlapped when considering the standard deviation intervals. In contrast, the additives with the lowest molar masses (SP1, SP2 and SP3) were less efficient in the water/oil separation (between 70 and 82%). Between additives SP2 and SP1, neither of which have PO units in their chains, SP2 promoted faster water/oil separation. This can be

due to its higher silicone content, probably promoting better diffusion of this additive's chains in the oil phase, thus allowing its molecules to reach the water/oil interface more quickly. Despite the lower molar mass of additive SP3, it was the most efficient of the three additives with lowest molar mass (SP1, SP2 and SP3). This can be attributed to the presence of PO units in its chains, which appear to improve its performance, likely because of its greater interaction with the emulsion's oil phase.

2) Rheological Analysis

Because the stability of emulsions is directly related to the properties of the water/oil interfacial film [13,14,25,] we conducted rheological analysis of the five additives. The interfacial tension data obtained by the pendant drop method allowed determining other rheological parameters, namely the compressibility, crumpling ratio and stability parameter, shedding more light on the effects caused by the additives and the interface of the emulsions.

3) Surface Pressure Isotherms

The surface pressure isotherm is obtained by plotting the graph of the surface pressure (π) in function of the interfacial area (Equation 1). These graphs demonstrated that the compressibility of the water/oil films fell sharply when the interfacial areadeclined, as shown by Equation 2. The reduction in compressibility prevents coalescence of the droplets and thus prevents the destabilization of the emulsion. Figures 4 to 8 show the surface pressure isotherms for additives SP1, SP2, SP3, SP4 and SP5, respectively. From the graphs it can be seen that the films' compressibility increased with the passage of time, destabilizing the emulsions. This behavior was expected, due to the good gravitational separation efficiency of the additives based on silicone polyethersanalyzed (Figure 2). The analysis of the surface pressure also demonstrated that for all the silicone polyether samples the additive's molecules were adsorbed at the interface, forming a film with higher compressibility, and thus irreversible, able to destabilize the emulsion. The irreversibility of these films could be observed by the absence of readsorption of the asphaltene molecules at this interface. The results obtained also showed that all the additives studied increased the surface pressure. This behavior can be attributed to the fact

the surfactant molecules are adsorbed faster at the water/oil interface than the asphaltene molecules. Figures 7 and 8 do not show any phase transition. This behavior can be related to the speed of the adsorption of the silicone polyether molecules at the water/oil interface. It appears that the adsorption occurs quickly enough so as not to allow transition from a reversible to an irreversible film. This phenomenon was expected in light of the better results in the gravitational separation tests carried out with these samples (Fig. 3).
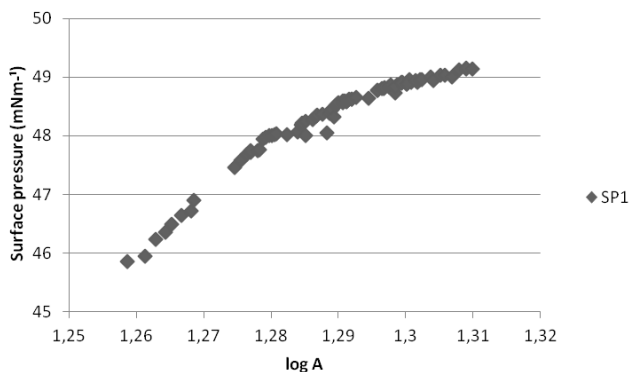
FIGURE 4: SURFACE PRESSURE ISOTHERM FOR ADDITIVE SP1
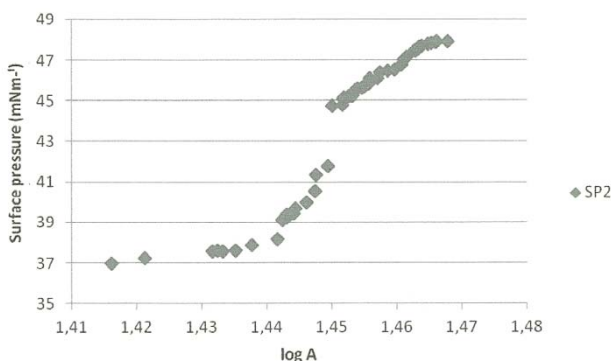
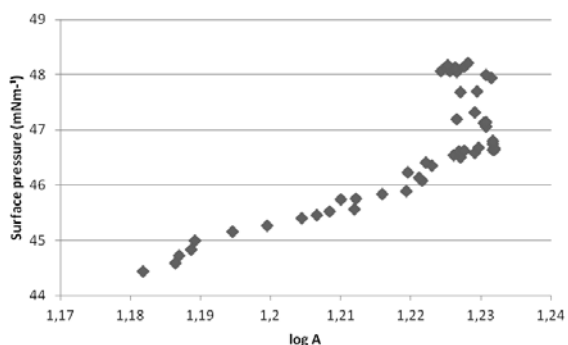FIGURE 5: SURFACE PRESSURE ISOTHERM FOR ADDITIVE SP2

FIGURE 6: SURFACE PRESSURE ISOTHERM FOR ADDITIVE SP3

In contrast, for samples SP1, SP2 and SP3 (Figures 4 to 6, respectively), this transition can be observed, indicating a slightly slower adsorption speed than for the other two samples. These samples have the lowest molar masses, which may explain the slower transition speed observed for them, making the destabilization process slower. Also based on these surface pressure isotherms, it was possible to confirm another rheological parameter, the crumpling ratio. This ratio defines the stability of an emulsion, discussed next.
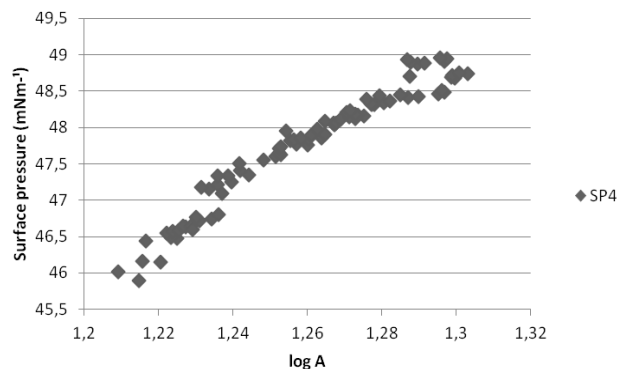

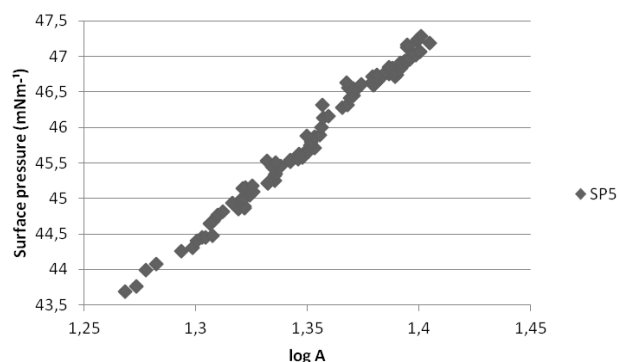FIGURE 7: SURFACE PRESSURE ISOTHERM FOR ADDITIVE SP4

FIGURE 8: SURFACE PRESSURE ISOTHERM FOR ADDITIVE SP5

4) Stability Parameter of the Emulsion

Determination of the crumpling ratio is important to understand the destabilization of an emulsion. Films with high crumpling ratios undergo little compression during coalescence, causing the formation of stable emulsions. Table 4 shows the crumpling ratio for each additive studied and the emulsion stability parameter, calculated by Equation 5. This parameter was developed by Ortiz and colleagues [25] and is related to the system's crumpling ratio and interfacial tension.

$$ SP = CR^{0.5}\left(\frac{\pi}{\gamma^\circ}\right) = CR^{0.5}\left[1 - \left(\frac{\gamma}{\gamma^\circ}\right)\right] \quad \text{Equation (5)} $$

Where SP is the stability parameter, CR is the crumpling ratio after 4 hours, π is the surface pressure, γ is the sample's interfacial tension (in the presence of asphaltenes or solution of surfactants) and γ is the interfacial tension of the

pure solvent.

The data in Table 4 indicate that all the w/o emulsions in the presence of the additives had extremely low stability, with only small differences between them. This parameter takes into consideration all the rheological characteristics of the interface (the crumpling ratio, surface pressure and interfacial tension). For this reason, although the samples differed in their demulsification efficiencies, the parameters calculated did not vary according to this efficiency.

TABLE 4. COMPARISON BETWEEN THE CRUMPLING RATIO AND THE STABILITY PARAMETER OF EACH ADDITIVE

Sample	Crumpling ratio (CR) (a)	Stability parameter (SP)
No additive	1.04	1.105
SP1	0.21	0.037
SP2	0.30	0.073
SP3	0.17	0.024
SP4	0.20	0.034
SP5	0.26	0.053

(a) Error of ± 0.1

5) Effect of Asphaltene Molecules on the Stability of the Emulsions

To assess the interfacial behavior of the additives and the asphaltenes extracted from the crude oil sample, we analyzed the interfacial tension of the saltwater/asphaltenes and/or additives by the pendant drop method, at a constant temperature of 25 °C. This evaluation was only performed with two of the additives, the ones that presented the best and worst efficiency in the water/oil gravitational separation tests (SP4 and SP2, respectively). Evaluation of the toluene/saltwater systems with and without asphaltenes allowed perceiving the action of the asphaltenes at the water/oil interface. As expected, the asphaltenes act as surfactants, able to reduce the interfacial tension of the toluene/saltwater system. The interfacial tension of the system containing only toluene was 21.3 mNm^{-1}, that declined to 12.7 mNm^{-1} with the addition of the asphaltene molecules (concentration of asphaltenes in solution of 2.4 wt%). Analysis of Figure 9 shows that, as expected, both additives SP2 and SP4 have surfactant action, that is, their molecules migrate to the interface and reduce the tension, as already observed previously, with additive SP2 being slightly more efficient in reducing the interfacial tension. It is believed that the demulisifaction process occurs by displacement of the asphaltene molecules at the interface, which are replaced by the addtive's molecules. The

additive forms a more compressible interfacial film than that formed by theasphaltene molecules and thus allows the water droplets to coalesce.It can be observed from analyzing the graphs of the interfacial tension of the solutions of saltwater and asphaltenes with additives that for additive SP4 the interfacial tension varied with time until reaching the tension value of the additive/saltwater system (~4.7mNm^{-1}). This behavior indicates a high rate of displacement of the asphaltene molecules at the water/oil interface, explaining the highest efficiency in separating the water from the system observed in the presence of this additive (Figure 3). The results for additive SP2 indicate that the interface still appears to contain asphaltene molecules, since the saltwater/additive solution's interfacial tension (~4.4mNm^{-1}) was lower than that of the system formed by saltwater/asphaltenes with the additive (~6.0mNm^{-1}). This indicates that the lower gravitational separation efficiency can be attributed to the lower displacement of asphaltenes at this interface.
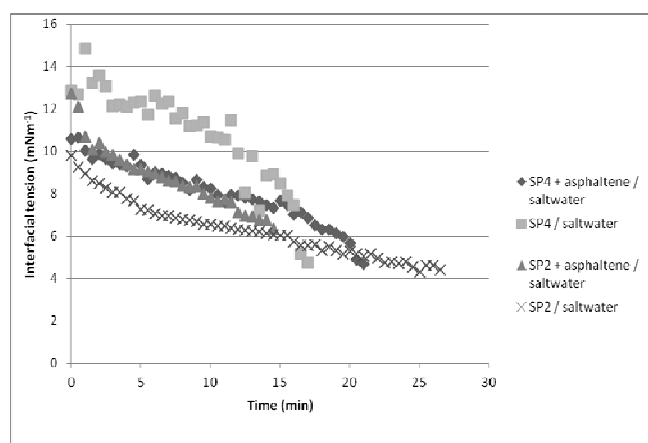

FIGURE 9: INTERFACIAL TENSION MEASURES OF SYSTEM SP2 IN TOLUENO/SALT WATER WITH AND WITHOUTASPHALTENES

Conclusions

All the additives based on silicone polyethers evaluated in this study were efficient in destabilizing water-in-oil emulsions.The additives with higher molar masses were more efficient in breaking down the water-in-oil emulsions, and among them the one with the highest silicone concentration in its chains was the most efficient.By the surface pressure isotherms, it was possible to verify that compressibility of the films formed in the water/additive emulsions increased with time, promoting destabilization of the emulsions. Besides this, all the additives studied were capable of being

adsorbed at the interface, forming an irreversible film, also with higher compressibility, able to promote destabilization of the emulsion.All the w/o emulsions with the presence of the additives had a very low stability parameter, but this parameter did not vary according to the efficiency of each additive. All the additives had surfactant action, meaning their molecules migrated to the interface of the w/o system and reduced the interfacial tension of the system. The additives were able to remove the asphaltene molecules of water/oil interface. However, the lower water/oil gravitational separation efficiency was attributed to the lower removal of asphaltenes from this interface.

ACKNOWLEDGEMENTS

REFERENCES

Alexandridis P., Athanassiou V., Fukuda S., Hatton T. A. "Surface-activity of poly(ethylene oxide)-block-poly(propylene oxide)-block-poly(ethylene oxide) copolymers." Langmuir 10 (1994): 2604.

Arnold K. E.,Smith H. V. "Petroleum Engineering Handbook", 3rd Ed., Chapter 19, Richardson- Texas-USA: Society of Petroleum Engineers, 1992.

Fan Y., Simon S.,Sjoeblom, J. "Interfacial shear rheology of asphaltenes at oil–water interface and its relation to emulsion stability: Influence of concentration, solvent aromaticity and nonionic surfactant." Langmuir 26 (2010): 10497.

Fraga A. K., Rezende D. A., Santos R. F., Mansur C. R. E. "Method to evaluate foaming in petroleum." Brazilian Journal of Petroleum and Gas 5 (2011): 21.

Fraga A. K., Santos R. F., Mansur C. R. E. "Evaluation of the efficiency of silicone polyether additives as antifoams in crude oil." Journal of Applied Polymer Science 124 (2012): 4149.

Gao S., Moran K., Xu Z.,Masliyah, J. "Role of Bitumen Components in Stabilizing Water-in-Diluted Oil Emulsions." Energy & Fuels 23(2009): 2606.

Hannisdal A., Ese M., Hemmingsen P., SjöblomJ. "Particle-stabilized emulsions: Effect of heavy crude oil components pre-adsorbed onto stabilizing solids." Colloids and Surfaces A: Physicochemical and Engineering Aspects276(2006): 45.

Hunter R. J., Foundations of Colloid Science. Clarendon Press, Oxford: 1986.

Kang W. L., Jing G. L., Zhang H. Y., Li M. Y., Wu Z. L. "Influence of demulsifier on interfacial film between oil and water." Colloids and Surfaces a-Physicochemical and Engineering Aspects 272 (2006): 27.

Lucas E. F., Mansur C. R. E., Spinelli L. S.,Queirós, Y. G. C. "Polymer science applied to petroleum production." Pure and Applied Chemistry 81 (2009): 473.

Mansur C. R. E., Barboza S. P., Gaspar G., Lucas E. F. "PLURONIC X TETRONIC polyols: study of the properties and performance in the stabilization of emulsions formed in the petroleum industry." Journal of Colloid and Interface Science 271 (2004): 232.

Mansur C. R. E., Lechuga F. C., Mauro A. C., González G., Lucas E. F. "Behavior of mixtures of nonionicpolyoxide-based surfactants and their application in the destabilization of oil emulsions." Journal of Applied Polymer Science 106 (2007): 2947.

Moore W.J. Physical Chemistry. Prentice-Hall, Inc., New Jersey: 1972.

Moradi M., Alvarado V., Huzurbazar S. "Effect of Salinity on Water-in-Crude Oil Emulsion: Evaluation through Drop-Size Distribution Proxy." Energy & Fuels 25(2011): 260.

Ortiz D. P., Baydak E. N., Yarranton H. W. "Effect of surfactants on interfacial films and stability of water-in-oil emulsions stabilized by asphaltenes." Journal of Colloid and Interface Science 351 (2010): 542.

Pacheco V. F., Spinelli L. S., Lucas E. F., Mansur C. R. E. "Destabilization of petroleum emulsions: evaluation of the influence of the solvent on additives." Energy Fuels 25 (2011): 1659.

Ramalho J. B. V. S., Lechuga F. C., Lucas E. F. "Effect of the structure of commercial poly(ethylene oxide-b-propylene oxide) demulsifier bases on the demulsification of water-in-crude oil emulsions: elucidation of the demulsification mechanism."Quim. Nova 33 (2010): 1664.

Rezende D. A., Bittencourt R. R., Mansur C. R. E. "Evaluation of the efficiency of polyether-based antifoams for crude oil." Journal of Petroleum Science and Engineering 76 (2011): 172.

Silva P. R. S., Mauro A. C., Mansur C. R. E. "Linear and branched polyoxide-based copolymers: methods to determine the CMC." Journal of Applied Polymer Science 113 (2009): 392.

Souza V. B., Neto J. S. G., SPinelli L. S., Mansur C. R. E. "Application of oil/water nanoemulsions as a new alternative to demulsify crude oil."Separation Science and Technology, in press (2013).

XuY. M., Wu J. Y., Dabros T., Hamza H., Venter J. "Optimizing the polyethylene oxide and polypropylene oxide contents in diethylenetriamine-based surfactants for destabilization of a water-in-oil emulsion." Energy & Fuels19 (2005): 916.

Yan N., Gray M. R., Masliyah J.H. "On water-in-oil emulsions stabilized by fine solids." Colloids and Surfaces A 193 (2001): 97.

Yang X. L., Hamza H., Czarnecki J. "Investigation of subfractions of athabasca asphaltenes and their role in emulsion stability." Energy & Fuels 18 (2004): 770.

Yarranton H. W., Sztukowski D. M.,Urrutia, P. "Effect of interfacial rheology on model emulsion coalescence: I. Interfacial rheology." Journal of Colloid and Interface Science 310 (2007): 246.

Zhang Z., Xu G.Y., Wang F., Dong S.L., Li Y.M. "Characterization and demulsification of poly(ethylene oxide)-block-poly(propylene oxide)-block-poly (ethylene oxide) copolymers." Journal of Colloid and Interface Science 277 (2004): 464.